Polarimetric Studies of the Solar Atmosphere

A THESIS

submitted for the award of Ph.D. degree of

MOHANLAL SUKHADIA UNIVERSITY

in the

Faculty of Science

by

Sanjay Gosain

Under the Supervision of

Dr. K. Venugopalan

(Professor)

DEPARTMENT OF PHYSICS

FACULTY OF SCIENCE

MOHANLAL SUKHADIA UNIVERSITY

UDAIPUR

2007

DECLARATION

I hereby declare that the work incorporated in the present thesis entitled **"Polarimetric Studies of the Solar Atmosphere"** is my own work and is original. This work (in part or in full) has not been submitted to any University for the award of a Degree or Diploma.

Date: (Sanjay Gosain)

CERTIFICATE

I feel great pleasure in certifying that the thesis entitled **"Polarimetric Studies of the Solar Atmosphere"** embodies a record of the results of investigations carried out by Mr. Sanjay Gosain under my guidance. I am satisfied with the analysis of data, interpretation of results and conclusions drawn.

He has completed the residential requirement as per the rules.

I recommend the submission of thesis.

Prof. Dr. K. Venugopalan
(Supervisor)

Prof. Dr. P. Venkatakrishnan
(Co-supervisor)

Date:

Acknowledgements

It is a great pleasure to thank my supervisors Prof. K. Venugopalan and Prof. P. Venkatakrishnan for their valuable guidance and encouragement in carrying out this work. The discussions with them regarding various problems during this work proved to be very fruitful. Their aspiration to carry out outstanding research work has always been a source of inspiration for me. It was a great experience to work with them and I hope to continue working with them in future also. I thank Prof. J. N. Goswami, Director, Physical Research Laboratory for providing me all the necessary facilities to carry out my thesis work. I also thank Prof. G. S. Agarwal, former Director of Physical Research Laboratory who allowed me a special permission to pursue my Ph. D. I also wish to thank Prof. K. Krishnaswami for granting permission and travel funds to attend solar physics schools abroad during the course of my Ph.D. I would like to express my gratitude to Dr. K. Sankarasubramanian and Dr. R. Sridharan for sharing their experience and knowledge by answering to my queries promptly whenever I had one. I also thank them for kindly providing their IDL programs related to image processing. In particular, I would like to thank Dr. Sankarasubramanian, for introducing to me the techniques for data reduction and inversion of Advance Stokes Polarimeter (ASP) observations.

I sincerely thank the SOHO/MDI team for making such a wonderful instrument, and providing high quality data available on-line and even sending in tapes and DVDs for free.

I am thankful to my colleagues and friends Mr. Brajesh Kumar and Mr. Raja Bayanna for their help in various matters. I thank the students Sanjeev Tiwari, Jayant Joshi and Ram Ajor Maurya for having exciting scientific discussions. Also, I thank all of them for their company during the observations.

I would like to thank my colleagues Prof. Ashok Ambastha, Dr. Debi Prasad

Choudhary, Dr. Nandita Srivastava, and Dr. Shibu K. Mathew for their help and support at various stages of my thesis. Special thanks to Dr. Debi Prasad Choudhary and Dr. Shibu K. Mathew, from whom I learned many instrumentation skills.

I would like to thank Dean, M. B. College of Science, Mohanlal Sukhadia University for extending the facilities for the research work. Also, I would like to thank the faculty members and staff of M. B. College of Science for their help during the thesis work. The help from project students of M. Sc. (I.T.) of MLSU in developing software components is also acknowledged.

I thank the administrative staff of USO, Mr. Raju Koshy, Mr. Rakesh Jaroli, Mr. C. P. Suthar, Mr. Ramachandra Carpenter, Mr. Dalchand Purohit, Mr. Shankarlal Paliwal and Mr. Jagadish Singh Chouhan for their help at various stages and providing me the friendly environment at USO. I thank Mr. Laxmilal Suthar for helping in carrying out co-ordinated H-alpha observations with me.

I am greatly thankful to the expert technical help from Mr. Sudhir Kumar Gupta and Mr. Naresh Jain in setting up the electrical and electronics subsystems. Special thanks to Mr. F. M. Pathan, who troubleshooted the CS100 controller, used to maintain parallelism of Fabry-Perot etalon. Also, I thank (late) Mr. B. L. Paneri who helped in designing and fabricating several opto-mechanical sub-systems with fine precision. His absence during phase-II of the instrument was very much felt. I also thank the people in PRL in mechanical workshop, Mr. G. P. Ubale, Mr. G. A. Panchal among others who were very prompt and helpful in fabricating the instrument subsystems.

I am greatly thankful to Dr. G. Madhavan Nair, Chairman of Indian Space Research Organization (ISRO) for accepting our invitation to inaugurate the instrument. His appreciation has greatly boosted my confidence and inspired me to work even harder in future.

I would like to thank the Ph.D. section of Mohanlal Sukhadia University for their kind co-operation throughout my thesis.

Also, I thank my neighbour, Mr. Chander Singh Samar, who allowed me to use his internet connection during the writing part of my thesis.

Finally, I appreciate the patience shown by my daughter, Vanshita, and my wife, Ruchi, while I was working on weekends. I thank my parents for constant encouragement to pursue the thesis work. I thank all of them for enduring with me. Without their support it would have been a difficult task. I hope they will continue their support in the same way in future also.

Sanjay Gosain

Contents

Acknowledgements **iii**

List of Figures **x**

List of Tables **xiii**

Abstract **xiv**

1 Introduction **1**

1.1 Introduction to solar magnetic fields 1

1.1.1 Global Structure of the Magnetic field 3

1.1.2 Active Region Magnetic Fields 4

1.1.3 Evolution of Active Region Magnetic Fields 8

1.2 Measurements of Solar Vector Magnetic Field 10

1.2.1 Zeeman Effect 10

1.2.2 Hanle effect 12

1.2.3 Polarized Light and Stokes Parameters 14

1.2.4 Solar Polarimeters 16

1.3 Motivation and Outline of the thesis 17

2 Solar Vector Magnetograph Instrumentation **20**

2.1 An Introduction to Solar Magnetographs 20

2.2 Earlier Magnetograph at USO 24

2.3 Solar Vector Magnetograph 24
2.4 Optical layout of SVM 27
2.5 Polarimeter Module 28
2.5.1 Quarter Waveplates 29
2.5.2 Nanorotator Rotary Stages 31
2.5.3 Dual Beam Calcite Analyser 32
2.5.4 Polarimeter Calibration 35
2.5.4.1 Measurement of polarimeter response matrix . . 36
2.6 Narrow-band imaging filter system 39
2.6.1 Brief overview of Fabry-Perot Interferometers 40
2.6.2 Comparison of a solid and air-gap etalon 41
2.6.3 Fabry-Perot system of SVM 42
2.7 Digital CCD Camera 45
2.8 Solar Vector Magnetograph: Phase I 47
2.9 Solar Vector Magnetograph : Phase II 49

3 Software for Instrument Control 52

3.1 Summary 52
3.2 Control Software: Design Approach 53
3.3 Hardware aspects of various components 53
3.3.1 Computer Hardware and Peripherals 53
3.3.2 Fabry-Perot Controller 54
3.3.3 Polarimeter Controller 54
3.3.4 CCD Controller 55
3.4 Software Design 56
3.4.1 CCD Control module 56
3.4.2 Polarimeter module 57
3.4.3 Fabry-Perot etalon CS100 control module 58
3.4.4 Analysis and Visualization System 60

3.4.5 Control software enhancements during phase-II 62

3.5 Discussion and Conclusion 64

4 Data Reduction and Stokes Inversion 65

4.1 Summary 65

4.2 SVM Observational Data-set 67

4.2.1 Visualizing a Wavelength Data-cube 68

4.2.2 SVM FITS File Format and Extended Header Description 70

4.2.3 CCD camera parameters incorporated in the FITS header 71

4.2.4 Fabry-Perot etalon controller (CS100) parameters 71

4.3 Data Reduction 72

4.3.1 Dark, Bias removal 72

4.3.2 Flat fielding 72

4.3.3 Image Registration 73

4.3.4 Co-aligning the dual beams 74

4.3.5 Removal of Fringes 75

4.3.6 Polarization calibration 76

4.4 Stokes Inversion of the observed profiles 76

4.4.1 Polarized Radiative Transfer Formulation 78

4.4.2 Stokes Inversion 80

4.4.3 Stokes inversion of SVM data 81

4.4.4 A toolkit for Milne-Eddington inversions 82

4.5 Visualization package for SVM vector data 83

5 Acoustic wave interaction with inclined magnetic fields 87

5.1 Introduction 87

5.2 Observational Data 88

5.3 Variation of acoustic power with vector field parameters 93

5.4 Inferences on excitation of 5 minute oscillations in magnetic regions 93
5.5 Acoustic power distribution 95
5.6 Results and Discussion 96
5.7 Summary 98

6 Summary, Conclusion and Future Improvements 99

6.1 Summary and Conclusions 99
6.2 Future Improvements 103
6.2.1 A fast CCD camera and Modulator 104
6.2.2 Parallelization of Stokes Inversion 106
6.2.3 Simultaneous Stokes observations in chromospheric lines 108
6.2.4 Higher spatial resolution 109

Appendix 109

Bibliography 114

List of Publications 130

List of Figures

1.1 Magnetic butterfly diagram: The time-latitude diagram of longitudinally averaged line-of-sight flux 4

1.2 Sample full disk line-of-sight magnetogram obtained from SoHO/MDI instrument during solar maxima 5

1.3 Structure of photosphere due to pores and sunspot as seen by SVM instrument 6

1.4 Structure of magnetic fields as seen in the corona 7

2.1 Schematic layout of the optical and control system of the Solar Vector Magnetograph 28

2.2 The Nanorotator stages used in polarimeter 33

2.3 Schematic of Calcite beam displacing prism 35

2.4 The left panel shows the calculated Stokes input vector from the known properties of the input polarizer and retarder and the right panel shows corresponding observed Stokes parameters as a function of retarder orientation. The Stokes parameters I,Q,U and V are represented as dash-dot-dot-dashed, dotted, dashed, and dash-doted respectively. 37

2.5 Observed Stokes parameters corrected for polarimeter response matrix are shown together with theoretical input Stokes vector. 38

2.6 Tilt response of FP etalon 44

2.7 Channel spectrum of the two FP etalons 45

2.8 Instrumental profile of the air-gap FP etalon 46
2.9 Solar Vector Magnetograph Phase-I, roof-top setup at the USO main campus 48
2.10 First light polarized images obtained from phase-I of SVM . . . 49
2.11 Solar Vector Magnetograph Phase-II, island-site setup at the USO main campus 51

3.1 A closeup of the CCD camera control section in the control GUI. 57
3.2 A closeup of the polarimeter control section in control GUI . . . 58
3.3 A closeup of the Fabry-Perot control section in control GUI . . . 59
3.4 A schematic of FP calibration procedure. 60
3.5 A closeup of the slider used for visualizing the datacube frames in the control GUI 61
3.6 A snapshot of the GUI after integrating all sections 62

4.1 A visualization of the wavelength data-cube. 69
4.2 An example of the typical flat-field applied to the data 73
4.3 An illustration of the image registration procedure of the SVM dataset 74
4.4 An example of fringe removal from the data 75
4.5 A snapshot of the GUI for the data reduction of SVM observations 77
4.6 A snapshot of the GUI for the performing inversion of Stokes profiles 84
4.7 A snapshot of the interface developed for visualization of SVM vector magnetograms 86

5.1 USO vector magnetograms and SOHO/MDI dopplergrams for NOAA AR No. 10756 91
5.2 SOHO/MDI Intensity and longitudinal flux maps corresponding to the sunspot NOAA No. 10756 92

5.3 The plots of mean power spectrum in regions lying in different inclination and field strength bins 94
5.4 The maps of binned high and low frequency power for the sunpot NOAA No. 10756 are shown 96

6.1 Chirality of vector magnetogram on 9 January, 2007 102
6.2 Chirality of vector magnetogram on 6 February, 2007 103
6.3 A schematic of the design for implementing parallel inversion of Stokes profiles 106
6.4 A snapshot of the webcam based solar autoguider control software112

List of Tables

2.1 Vector magnetographs around the world 23
2.2 Orientations of Quarter Wave-plates used in polarimeter 30
2.3 Specifications of Quarter Wave-plates 32
2.4 Specifications: Calcites 34
2.5 Fabry-Perot Etalon Properties 43

Abstract

Solar magnetic fields play an important role in the variety of activity phenomena observed on the Sun. They are present right from Sun's deep radiative interior up-to the heliopause. Their evolution, mainly due to photospheric dynamics and flux emergence, leads to activity phenomena like flares, filament eruptions, Coronal Mass Ejections (CMEs). These phenomena directly affect near-Earth space weather by the accompanying high-energy radiation and charged particles. In order to predict these events a detailed understanding of solar magnetic structures is required. Thus, task of measuring solar magnetic fields is of utmost importance in solar physics. However, the measurement of solar magnetic fields is very challenging task. The challenge comes mainly from the fact that the measurements need to be done remotely by sensing the polarization (due to Zeeman effect) of solar spectral lines. Also, the distortions in imaging due to atmospheric "seeing" leads to poor spatial resolution and effects polarization measurements. The focus of this thesis is on the measurement aspects of solar magnetic fields. A new instrument is developed for measuring the vector magnetic fields in the photosphere. The instrument is called Solar Vector Magnetograph (SVM). The key features of the instrument are (i) symmetric imaging optics with no oblique reflections, to minimize instrumental polarization, (ii) a tunable narrow-band imaging filter for scanning the spectral line, which is based on Fabry-Perot etalon, (iii) dual-beam polarization analyzer (Savart Plate), to minimize seeing induced spurious polarization signals, and (iv) a self-developed instrument control software for automated observations. Further, a data-reduction and analysis package with graphical user interface (GUI) is developed for interactive data reduction. The interpretation of observed polarization, i.e., Stokes profiles, in terms of magnetic field vector is done by fitting them with theoretical profiles under Milne-Eddington model atmosphere assumptions. The packages are developed for this purpose as well as for the analysis and visualization of vector magnetograms. Finally, a study of the effect of vector magnetic field parameters on the solar acoustic p-modes is carried out.

Chapter 1

Introduction

1.1 Introduction to solar magnetic fields

The Sun, our nearest star, directly interacts with us with its radiative output and keeps our ecosystem in balance. A tiny variation in Sun's irradiance can lead to global changes in the climate of the Earth. Researchers have found evidence that the Sun's magnetic field has increased during last century (Lockwood et al. 1999). How much is the solar activity responsible for the global warming is a hot topic of research (Solanki et al. 2004). The activity phenomena on the Sun like coronal mass ejections (CMEs), filament eruptions and highly energetic flares lead to enhanced X-ray, gamma ray and charged particle flux into space and affect the near Earth space weather. The source of all these activities is the solar magnetic field. This is the reason why magnetic field is the most studied parameter of the Sun. Though our understanding of various aspects of solar magnetic fields has improved yet the subjects of eleven year sunspot cycle, coronal heating, sunspot structure and dynamics, stability (prominences) or instability (flares, CMEs) of magnetic structures remain enigmatic. In order to attain a thorough understanding of these subjects the magnetic field observations are required with large spatial and temporal coverage.

The fundamental role played by magnetic fields in solar activity phenomena has motivated solar physicists to develop innovative instruments. While George Ellery Hale (1908) made the pioneering efforts to measure magnetic fields in sunspots, new improved instruments have continually been developed over the years. The complete measurement of magnetic vector needs measurement of transverse component of magnetic field in addition to longitudinal fields. These complete vector field measurements are necessary because of variety of reasons. As E. N. Parker (1984) pointed out that stresses introduced in the magnetic field due to convective motions deform the field. Longitudinal fields do not give measurement of stress and one needs vector fields to study them. These stresses can be studied in relation to the flux emergence, flares, eruptive phenomena, onset of coronal mass ejections and so on. Due to very low plasma β (ratio of gas pressure to magnetic pressure) in upper chromosphere and corona the magnetic field is nearly force-free. In the absence of the chromospheric and coronal field measurements the photospheric vector fields are extrapolated in the volume above photosphere using force-free condition and appropriate boundary conditions.

The quantitative measurement of the magnetic fields is done by remotely sensing the spectral line polarization, induced due to the Zeeman effect. The Zeeman effect causes the splitting of atomic energy levels due to precession of atom around the magnetic field. The resulting split components of the spectral line are polarized, which depend on the strength and direction of magnetic field. By measuring the circular as well as linear polarization, the magnetic field direction and strength can be inferred. This is known as Zeeman effect diagnostics. Other diagnostics that are used to determine fields are called Hanle effect diagnostics. Certain lines in solar spectrum become polarized when they are partly formed by coherent scattering. In the presence of magnetic field, the precession of atoms modifies the nature of scattering polarization, called Hanle effect. Zeeman and Hanle effects are in a sense complimentary to each other as Hanle effect is sensitive to weak fields and fields of mixed polarity as compared to Zeeman effect.

In the present chapter we shall discuss the basic properties of solar magnetic fields and their role in activity phenomena. The topics are discussed according to magnetic structures and later according to phenomena. The measurement of solar magnetic fields using Zeeman and Hanle diagnostics is discussed briefly. Finally, the subject of polarization of light and spectro-polarimetric methods used in solar polarimetry are discussed. Towards the end of this chapter the motivation and outline of the thesis are given.

1.1.1 Global Structure of the Magnetic field

The distribution of magnetic flux at the solar surface spans all scales, from global dipolar structure seen during solar eclipse down to the limit of achievable angular resolution of present day ground and space based solar telescopes. The global magnetic field of the Sun undergoes an interesting 22 year cyclic behaviour, as seen in magnetic butterfly diagram (figure 1.1). This diagram is made by stacking side-by-side, the line-of-sight magnetic flux averaged over all longitudes. The noticeable features are the (i) opposite polarities in opposite hemispheres, (ii) gradual migration of active region belts towards equator, (iii) poleward migration of following polarity flux, (iv) polar magnetic fields, (v) reversal of polarities in active region belts and polar fields after 11 years. The inter-relationship between the general magnetic field of the Sun and the localized sunspot magnetic field became clear with the development of the magnetograph by H. Babcock (1953). The instrument was made more sensitive during 1950s. Hale-Nicholson sunspot polarity rule (1925) was also found to be applicable to more widespread facular regions. The advancements in the instrument further led to the discovery that the polar field of the Sun also reverses during the 22 year cycle. These findings led Babcock (1961) to propose a model, which is still the most accepted model, for cyclic behaviour of solar magnetic field.

The circular polarization map of the Sun (fig 1.2) shows an overview of large-scale flux pattern on the Sun at the time of activity maxima. The pattern appears quite complex but we can identify some features : new and old bipolar magnetic regions, the magnetic network, latitude zones of activity and the background field. The dominating bipolar regions are found in two belts, one in each hemisphere.

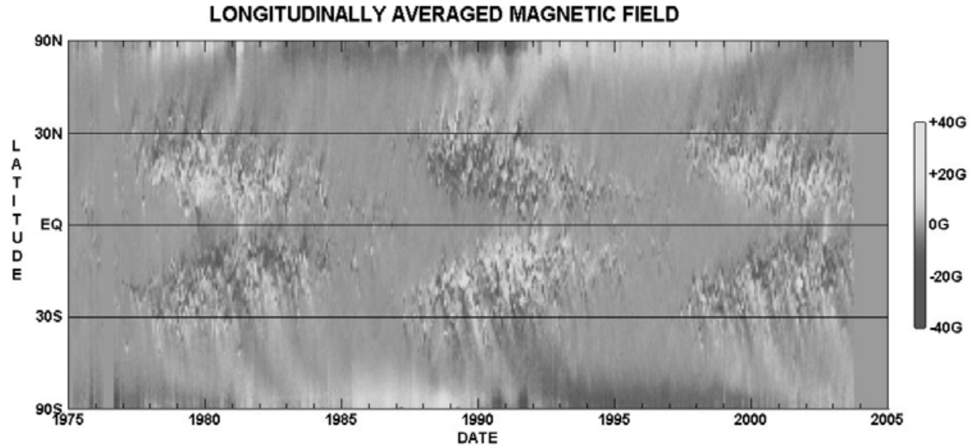

Figure 1.1: Time-latitude diagram of the longitudinally averaged line-of-sight magnetic flux, obtained from Kitt Peak synoptic Carrington maps, in the solar photosphere for the last three activity cycles. The emergence of magnetic flux in active regions migrates to lower latitudes with solar cycle. The combined effects of convection and meridional circulation lead to the magnetic flux transport to high latitudes and thus cause reversals of the polar magnetic fields in phase with the activity cycle.

The orientation of the new bipolar groups is slightly tilted with respect to east-west direction when it emerges, and slowly as the field disperses over timescales of days to months the large areas are covered with magnetic flux. The flux is highly intermittent and is carried about by granular and supergranular motions. The flux is swept away to the narrow boundaries of supergranular cells, where they make a network pattern with typical cell size of 30 Mm. The individual flux elements, however, are small and their size is expected to be of the order of 100 km only.

1.1.2 Active Region Magnetic Fields

The magnetic field emerging from solar interior in active regions is responsible for much of the structures seen on the Sun in different wavelengths. In the photoshere the structures are mostly in the form of sunspots and its associated sub-structures

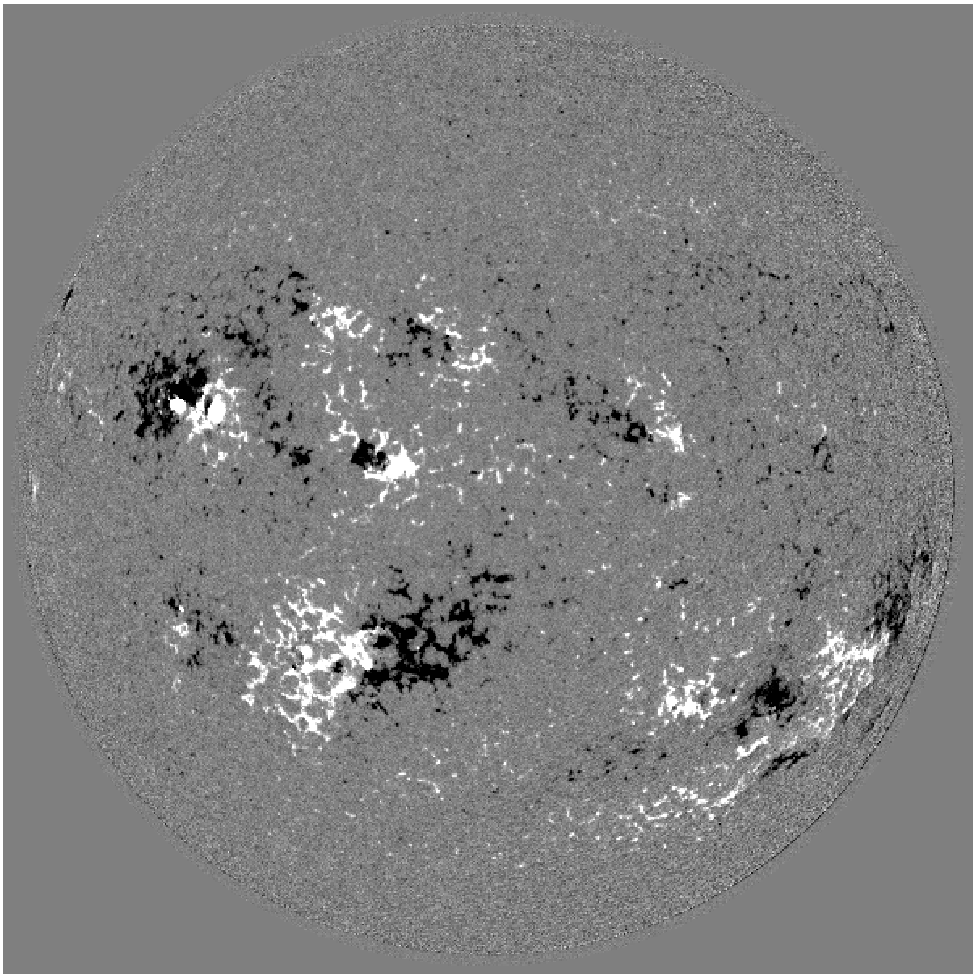

Figure 1.2: Full-disk line-of-sight magnetogram from SoHO/MDI instrument, obtained on 14 October 2001 (period of solar maxima). North is at top, east is to the left. Bright (dark) areas represent magnetic field directed towards (away) from us.

(umbral dots, penumbral filaments, light bridges), pores, white light granulation and the dynamical events are mainly white light flares, granular flows, Evershed flow and surface oscillations due to solar acoustic waves. The structures that were resolved by Solar Vector Magnetograph with its 1 arc-sec per pixel sampling are shown in figure 1.3. The structures seen in H-α filtergrams namely loops, prominences, spicules, plages, filaments and associated dynamic events like flares and prominence eruptions, jets, surges, etc are all governed by magnetic field. The coronal observations (fig

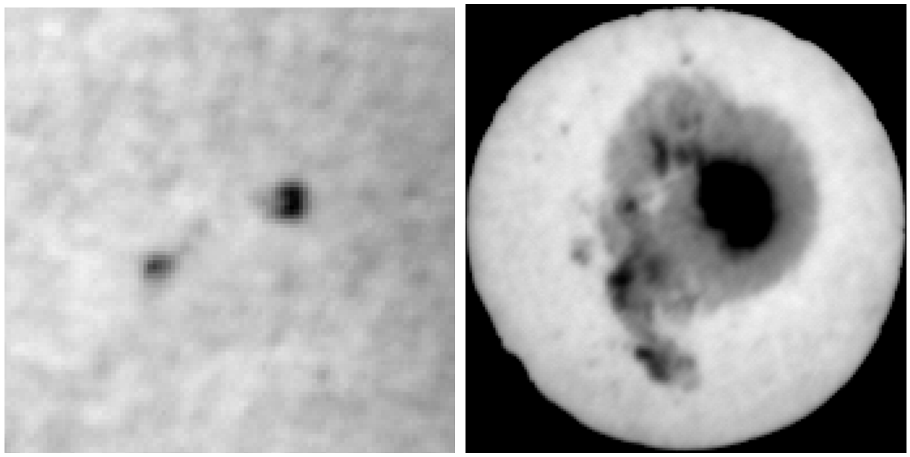

Figure 1.3: The structures resolved by SVM with its 1 arc-sec per pixel scale seen in photospheric continuum are shown. Two pores, corresponding to a small bipole, can be seen on the left panel. A simple sunspot within a circular field-of-view of SVM is shown in the right panel.

1.4) of the Sun in extreme ultraviolet wavelength and X-rays shows bright magnetic loops, X-ray bright points, sigmoid structures and coronal holes in “unipolar” field regions. Their dynamics is seen in events like flares, formation of post flare loops, filament eruptions, coronal dimming, Moreton waves etc. Further, in decimetric and longer radio wavelengths suprathermal electrons accelerated in active regions provide a bright emission through collective processes (“noise storms”) that exceed the emission of hot thermal plasma by few orders of magnitude. At distances of 2-3 $R_\odot$ plasma structures in white light show most prominent coronal streamers. Their structure suggests closed field structure at low heights and open field structure at the top due to streaming slow solar wind.

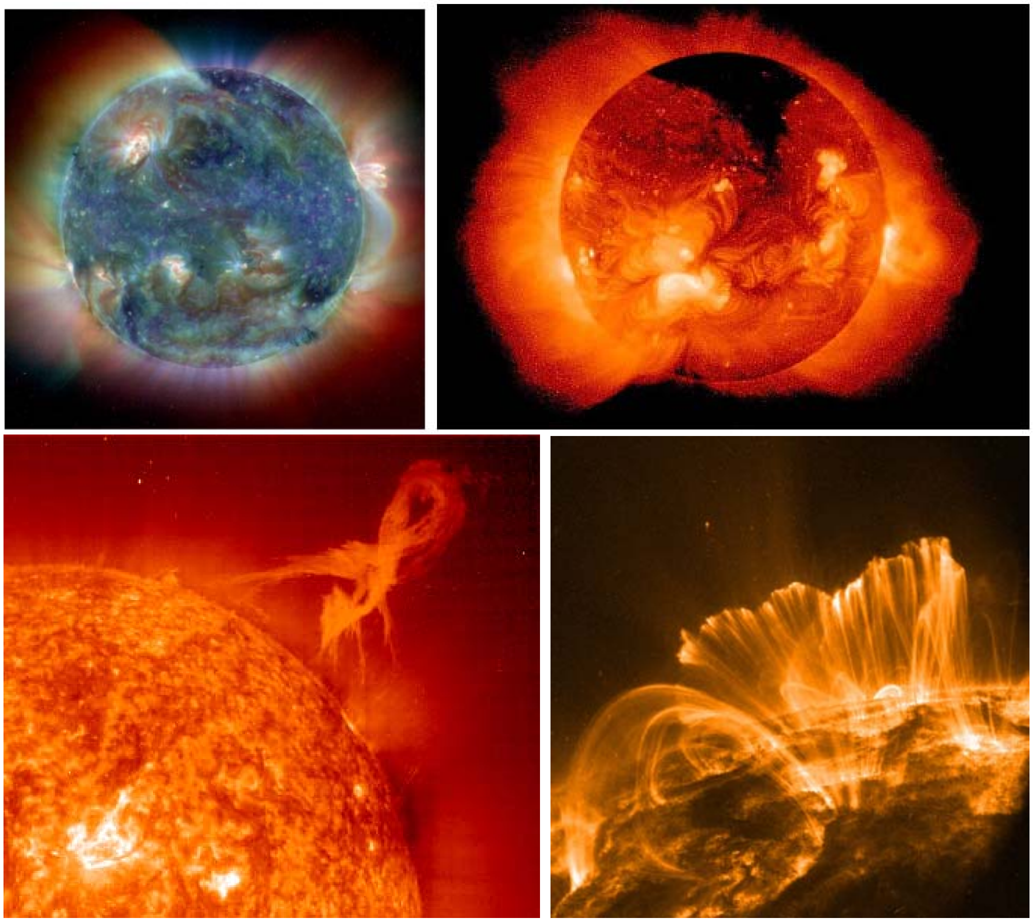

Figure 1.4: The left figure (top panel) shows structure of corona in a composite image in Extreme Ultra Violet (EUV) wavelengths from EIT instrument on-board SOHO satellite. The right figure on the top panel shows the image of the Sun in soft X-ray by YOHKOH satellite. The bright structures over active regions, relatively darker coronal holes and compact bright points are among prominent features in these images. The left image (lower panel) shows material carried high up in the corona with a twisted field configuration during an eruption event, as observed by EIT instrument on-board SOHO. The right image (lower panel) shows post flare loops in an arcade formation, as observed by TRACE satellite.

1.1.3 Evolution of Active Region Magnetic Fields

Flux emergence: The estimated per day flux emergence from the Sun is 10^{20} Mx in the form of active regions (AR), 10^{22} Mx in the form of ephemeral regions (ER) and 10^{24} Mx as intranetwork fields (IN) (Zirin, 1987). The emergence rates are order of magnitude different,1:100:10000 for AR:ER:IN. Therefore, a tiny non-random component of the IN flux emergence can make IN fields the dominating source of large-scale pattern (Stenflo, 1992). The relationship between small and large scale processes of flux emergence, and between global and local dynamos are the subject of intense debate (Harvey 1992; Durney 1993).

Flux cancellation: Magnetic flux cancellation was first described using high resolution Big Bear magnetograms (Wang Zirin and Shi, 1985; Martin et al 1995). By definition, flux cancellation is the mutual flux disappearance of closely spaced magnetic fields of opposite polarities. It has been identified to be the most important mode of flux disappearance on the Sun. Flux disappearance rate due to cancellation is measured to be rate 10^{15} to 10^{16} Mx per second approaching with a velocity of 0.3 to 0.6 km per second.

Moving magnetic features (MMFs): Granules and small magnetic elements, called moving magnetic features (MMFs) around the organized fields of sunspots in active regions are carried radially outwards at speeds up-to 1 km/sec. (Sheeley 1969; Harvey & Harvey 1973; Brickhouse & LaBonte 1988; Wang & Zirin 1992; Yurchyshyn et al. 2001). MMFs appear to carry net flux away from the sunspot at an estimated rate of $3 \times 10^{19} - 10^{20}$ Mx/hour, close to decay rate of 10^{19} Mx/hour.

Field evolution during solar flares: The flares emit radiation in a wide spectrum from radio to gamma rays. The variety of magnetic configurations seen in observations are difficult to explain with simple models. The models should explain where the energy is stored and how this is related to observed post flare loops and chromospheric ribbons. The post flare loops are seen to form between the flare ribbons during the development of majority of flares (Schmieder 1992; Malherbe 1997). These models suggest reconnection process to be responsible for this observed property (Forbes & Acton 1996; van Driel et al 1997). The energy released in flares can not be instantaneous energy transported from photosphere, rather the energy must be slowly built up and stored in the magnetic field and released suddenly due to reconnection.

Evolution in corona: The X-ray Sun is often characterized by S-shaped coronal loops over active regions. These structures are interpreted as twisted flux ropes due to loss of equilibrium (Pevtsov et al 1996; Rust & Kumar 1996). The reason for loss of equilibrium is either due to new flux emergence (Chen 1996) or slow photospheric motions storing energy in magnetic field structures. The helical-like pattern is seen often in eruption of prominences (Raadu et al 1988; Rompolt 1990; Vrsnak et al 1991). The quiescent phase of filaments does not show their magnetic structure, however, the models based on photospheric magnetogram can recover the shape of prominence with a twisted flux tube (Aulanier et al 1990). Observations of CMEs often show associated filament eruptions (Hundhausen 1988). The coronagraph pictures of CMEs often show prominence embedded within CME structure and often displays twisted structure, suggesting the flux rope structure of expanding magnetic field. In the interplanetary medium the twisted configurations are often identified as magnetic clouds (or interplanetary CMEs or ICMEs) with insitu measurements from satellites.

Thus, the observations and theoretical models suggest that the stressed magnetic fields manifest as twisted magnetic structures. These structures are probably formed at the bottom of convection zone, thereby bringing both magnetic energy and helicity into corona. In highly conducting corona magnetic energy can be dissipated at a fast rate while the helicity is a preserved quantity (Biskamp 1993) and cannot be removed easily. Also, the helicity is independent of solar cycle and only depends on hemispheres (negative/positive in north/south hemispheres) and cannot be removed by cancellation. There is a possibility that the trans-equatorial field connectivity (Choudhary et al 2002) between regions of opposite helicity can lead to cancellation of helicity to some extent. However, the main mechanism to remove accumulated magnetic helicity is to eject it in the interplanetary medium (Low 1996; Zhang & Low 2005).

1.2 Measurements of Solar Vector Magnetic Field

The electromagnetic radiation coming from distant objects like Sun and stars carries important information about the physical parameters of the object. This information is represented mainly in its properties like its intensity as a function of wavelength (spectra) and its polarization. The measured spectrum of light and its polarization can be interpreted in terms of theoretical models of the remote source. In solar physics, the measurement of magnetic field is an important topic of research. In order to remotely measure magnetic field on the Sun we measure Zeeman effect induced polarization of light in the magnetically sensitive spectral lines. These spectro-polarimetric observation are then interpreted using polarized radiative transfer in a model solar atmosphere permeated by magnetic fields.

1.2.1 Zeeman Effect

The Zeeman splitting of the spectral lines can be resolved only in sufficiently strong fields. For weaker fields, polarization of Zeeman components are used for measurement of magnetic field. Here we discuss the Zeeman effect and how it is used to measure fields by measuring polarized spectrum at a given point on Sun. The L-S (Russel-Saunders) coupling is appropriate for weak fields. L, S, J and M_J are the quantum numbers characterizing the quantum state of the atom. L characterizes total orbital angular momentum of the outer electrons, S is the analog for spin, and J determines the total angular momentum and M_J is magnetic quantum number which characterizes the component of J in a given direction, and takes the values $-J, -J+1, ...J$, while J itself can take values from $|L-S|, |L-S|+1, ...L+S$. For field strength, B, equal to zero all M_J states have same energy, that is, they are degenerate states. The degeneracy is removed if B is not zero and M_J is the component of J in the direction of field vector $\vec{B}$. The corresponding energy shift and resulting Zeeman splitting of spectral line depend upon the Land$\acute{e}$ factor of each state, defined as,

$$g = 1 + \frac{J(J+1) + S(S+1) - L(L+1)}{2J(J+1)}$$

Let $g, g^{'}$ and $M, M^{'}$ be Land$\acute{e}$ factors and magnetic quantum numbers of lower and upper states of the transition considered, respectively. The displacement of the spectral line from its undisplaced position corresponding to B=0 is given by,

$$\lambda - \lambda_0 = \frac{e}{4\pi c m_e} g^* \lambda^2 B,$$

where

$$g^* = gM - g^{'}M^{'},$$

g^* is the g-factor for transition. When λ is in units of cm and B is Gauss, then we can write $\Delta\lambda_B = \lambda - \lambda_0 = 4.67 \times 10^{-5} g^* \lambda^2 B$.

States with $S = 0$ have g=1. If both states of a transition have S=0 then the selection rule for M_J, is $\Delta M_J = -1, 0, +1$, which corresponds to $g^* = -1, 0, +1$. The result is "normal" Zeeman splitting, or Lorentz triplet. In some exceptions a triplet may occur even in transitions between states where $S \neq 0$. In these cases, however, the splitting may differ from normal case.

In general the Zeeman multiplet , or "anomalous" splitting is present. Since solar lines are broad the splitting is generally not resolved except for very strong fields. For weak fields it is possible to treat the multiplet as if it were a triplet. An "effective" $g-$factor is calculated from the g^* values of contributing components; each component is given a weight according to its intensity. Beckers (1969) has compiled a table of Zeeman multiplets and effective $g-$factors.

The Zeeman triplet is seen as two shifted σ components and one unshifted π component. Longitudinal Zeeman effect is seen when magnetic field is oriented in the line-of-sight. In this case the σ components alone are seen, which are circularly polarized in opposite sense. The sense is also opposite in absorption lines as compared to emission line. Transverse Zeeman effect is seen when field direction is perpendicular to the line-of-sight of the observer. In this case the observer will see all three components, however, the polarization seen is different. The unshifted π

component, is linearly polarized parallel to the field direction, and the σ components are linearly polarized perpendicular to field direction. Again, for the absorption lines the sense of polarization is different to emission line. The polarizations are changed by 90° for σ as well as π components. In general the field is oriented at an arbitrary angle and one observes combination of polarizations. It should be noted that, while the longitudinal Zeeman effect is sensitive to field direction (towards or away from observer), the transverse Zeeman effect is insensitive to the field direction reversed by 180°, which leads to an uncertainty of 180° in the inferred transverse field direction.

In the solar case, the splitting due to Zeeman effect can be recognized only for field strengths of the order of 1500 Gauss. In general, solar lines are Doppler and collision broadened; thus for weaker fields and strong unresolved fields the Zeeman splitting is seen only in the form of Zeeman broadening of spectral line. Although Hale first discovered magnetic field in sunspots by observing the Zeeman splitting in 1908, it was Babcock (1953) and Kiepenheuer (1953), who in 1950s investigated possibility of resolving Zeeman components by means of polarimetric methods.

1.2.2 Hanle effect

Consider an atomic transition between a lower state and two upper states which are degenerate. Then, a photon absorbed by an atom in the lower state will excite both the upper states coherently. When another photon is absorbed by the excited atom, then the resulting downward transition will have quantum interference between the two upper levels and the result is a coherence between incident photon and the scattered photon. This coherence produces polarization in the scattered photon. The polarization is a function of the scattering angle. When the incident radiation field is isotropic, the net polarization observed in any scattered direction is zero. However, when there is an anisotropic radiation field, then there is a net polarization in a given direction. Limb observations can therefore show polarization. The quantum interference is possible even when the energy difference between the two upper states is non-zero, but less than the energy equal to caused by "natural broadening". In the presence of a magnetic field, the degeneracy is lifted and the energy levels get separated. When the separation increases beyond the natural width, then the coherence due to the quantum interference is destroyed and there is a drop in polarization. Also, the plane of polarization rotates. This modification of scattering polarization by magnetic field is called the Hanle effect. Since the effect works in a frame of reference moving with the atom, the Hanle effect is not affected by thermal broadening and is therefore a very sensitive diagnostic of magnetic field. However, the maximum effects are observed when the Larmor frequency matches the natural width of the line. The Hanle effect is therefore very sensitive to weak fields.

Two effects seen in solar observations are (i) decrease of scattering polarization in a spectral line (depolarization), and (ii) rotation of plane of polarization when net magnetic flux is in the line-of-sight (Bianda 2003). Bruckner (1963) first measured linear polarization in wings of Ca I 4227 $\mathring{A}$. Later measurements were done by Stenflo (1974), Wiehr (1975;1978), Stenflo (1980;1983), Ivanov(1991) and Keller (2000) among many others. Ivanov coined the term "Second Solar Spectrum" for the linearly polarized spectrum produced due to coherent scattering. Faurobert-Scholl(1992;1993;1995) has worked on development of the radiative transfer tools to interpret the observations.

Zeeman effect and Hanle effect are complimentary to each other as the Hanle effect is sensitive to very weak magnetic fields while Zeeman effect is more sensitive to stronger fields. Also, the Hanle effect is insensitive to vertical fields whereas Zeeman effect is more sensitive to longitudinal fields. Stenflo et al (1998) found that the appearance of second solar spectrum changes greatly both spatially and with solar cycle and emphasize that more detailed mapping of Hanle effect is required.

1.2.3 Polarized Light and Stokes Parameters

The observations of polarized light is best represented in terms of Stokes vector. Since Stokes parameters express polarization in terms of measured intensities, it is the most natural definition to use in polarimetry. These parameters are represented as a Stokes vector

$$\vec{S} = [I, Q, U, V]^T,$$

where superscript T represents transposition. These parameters were introduced by G. G. Stokes in 1852 as a convenient alternative to the more common description of incoherent or partially polarized radiation in terms of its total intensity (I), (fractional) degree of polarization (p), and the shape parameters of the polarization ellipse.

Consider a plane monochromatic electromagnetic wave train, propagating along z direction so that the electric vector lies in the x, y plane. Then

$$E_x = \xi_x cos\phi, \qquad E_y = \xi_y cos(\phi + \epsilon),$$

where $\phi = \omega t - kz$; ϵ is phase difference between E_x and E_y; ξ_x and ξ_y are amplitudes. In general the polarization of light is elliptical with linear and circular polarizations as special case. The definition of Stokes parameters in terms of ξ_x, ξ_y and ϵ were given by G. G. Stokes as

$$I = \left\langle \xi_x^2 \right\rangle + \left\langle \xi_y^2 \right\rangle, \qquad Q = \left\langle \xi_x^2 \right\rangle - \left\langle \xi_y^2 \right\rangle,$$

$$U = 2\ Re \left\langle \xi_x \xi_y^* \right\rangle, \qquad V = 2\ Im \left\langle \xi_x \xi_y^* \right\rangle,$$

Where $\langle\rangle$ denotes an ensemble average over the large number of photons that are detected together in any light detector. For complete polarization we have the relation $I^2 = Q^2 + U^2 + V^2$, which is true for a single wave-train as it is always completely polarized. However, the natural light is never perfectly monochromatic, and has a certain bandwidth. If we consider a nearly monochromatic beam with bandwidth small in comparison with solar spectral lines. Even this beam should be considered as a wave-packet composed by superposition of large number of monochromatic wave-trains with small difference in their frequencies. These wave-trains have their own amplitudes and phases. The Stokes parameters in this case are represented as

$$I = \left\langle \xi_x^2 \right\rangle + \left\langle \xi_y^2 \right\rangle, \qquad Q = \left\langle \xi_x^2 \right\rangle - \left\langle \xi_y^2 \right\rangle,$$

$$U = 2\ Re \left\langle \xi_x \xi_y^* \right\rangle, \qquad V = 2\ Im \left\langle \xi_x \xi_y^* \right\rangle,$$

By resorting to the ergodic theorem, the ensemble average can also be treated as time average over the period of observation, sufficiently long so that result is independent of time.

For the partially polarized light we have the relation $I^2 \geq Q^2 + U^2 + V^2$, where the degree of partial polarization given as

$$P = \left(\frac{Q^2 + U^2 + V^2}{I^2} \right)^{1/2}.$$

The Stokes vector can describe unpolarized, partially polarized, and fully polarized light. For comparison, the Jones vector only spans the space of fully polarized light, but is more useful for problems involving coherent light. The four Stokes parameters do not form a preferred basis of the space, but rather were chosen because they can be easily measured or calculated. The effect of an optical system on the polarization of light can be determined by constructing the Stokes vector for the input light and applying Mueller calculus, to obtain the Stokes vector of the light leaving the system. For example, the Mueller matrix of an optical system like a train of telescope, spectrograph, liquid crystal retarder, polarizer etc is obtained by simple matrix multiplication of the Mueller matrices of the individual optical components in reverse order. Thus the Mueller matrix of the entire system,

$$\vec{M} = \vec{M}_n \vec{M}_{n-1} ... \vec{M}_2 \vec{M}_1,$$

where $\vec{M}_1$ is the first optical element in the optical train through which light enters. Also, the rotation of the optical elements leads to change in Mueller matrix, described by the operation

$$\vec{M}' = R(-\theta) \vec{M} R(\theta),$$

where θ is the rotation angle, and the rotation matrix is given by

$$R(\theta) = \begin{pmatrix} 1 & 0 & 0 & 0 \\ 0 & cos2\theta & sin2\theta & 0 \\ 0 & -sin2\theta & cos2\theta & 0 \\ 0 & 0 & 0 & 1 \end{pmatrix}$$

This is often useful in determining the Mueller matrices of rotating elements in the polarimeter like the wave-plates or polarizers. The treatment of Stokes vectors and Mueller matrix algebra for various optical components is given in monographs by Schurcliff (1962), Azzam & Bashara (1987) and more recently in Collett (1993) and Tinbergen (1996).

1.2.4 Solar Polarimeters

The existing spectro-polarimeters in solar astronomy basically differ in the way polarimetry and spectroscopy are implemented. Spectroscopy can be performed with modest spectral resolution (R=50,000 to 200,000) with narrow-band tunable filters like Fabry-Perot interferometers, birefringent filters or filters based on magneto-optical effects over the entire two-dimensional field-of-view. Alternatively, it can be done by a slit spectrograph, where one needs to scan the slit to record entire field-of-view. Solar spectro-polarimeters which use the filters have the advantage of obtaining the polarization map over the field-of-view instantaneously, however, they require to scan in wavelength domain in discrete steps. The examples of the spectro-polarimeters based on tunable filters are (i) Imaging Vector Magnetograph (IVM) (Mickey et al. 1996), (ii) Imaging Bi-dimensional Imaging Spectrometer (IBIS) (Cavallini et al 2006), (iii) Vector Imaging Polarimeter at VTT, Tenerife (Tritschler et al 2004), and (iv) the present one, the Solar Vector Magnetograph (SVM) (Gosain et al 2005; 2006). The examples of spectrograph based magnetographs are (i) Advance Stokes Polarimeter (ASP) (Elmore et al 1992), (ii) Polarimetric Littrow Spectrograph (POLIS) (Schmidt et al, 2003) (iii) Diffraction Limited Spectropolarimeter (DLSP) (Sankarasubramanian et al 2003, 2006), among many others. On the other hand the polarimeters which use spectrographs have typically high spectral resolutions and obtain instantaneous spectra, but only in one direction (along the slit). For two dimensional mapping one needs to scan in spatial domain (slit scanning). Both the schemes have their own advantages and disadvantages. The scanning is required in either spatial or spectral domain to achieve the complete observations. Historically there has been debates on these issues (Lites et al. 1994; Zirin 1995; Lites 1996). However, with the advancement of solar adaptive-optics technology, ultra-narrow pass-band filters like triple etalon filters working in tandem (TESOS, Tritschler et al 2002) and with improved inversion codes which can accurately recover magnetic field parameters with only few wavelength samples across the spectral line (Orozco Suarez et al 2006; Borrero et al 2007) the filter based instruments are becoming favourable. Specially, the compactness of filter based instruments, larger field-of-view and high spatial and temporal resolution has led to proposed Visible Imaging Magnetogrpah (VIM) on board Solar Orbiter satellite and proposed Helioseismic and Magnetic Imager (HMI) on-board Solar Dynamics Observatory (SDO) satellite.

1.3 Motivation and Outline of the thesis

The solar flares and other activity phenomena are caused by the toroidal magnetic field emerging in the form of solar active regions. The energy released in these explosive and energetic events in the form of radiation in all bands including X-rays, gamma rays and high energy particles, is initially stored in the "stressed" magnetic field configurations (Parker, E. N. 1984). In order to measure these stresses one needs to measure transverse components of the magnetic fields along with the longitudinal magnetic field. While the longitudinal magnetic fields are relatively easy to measure, the observation of transverse magnetic fields is difficult. For a detailed study of interrelationship between the evolution of magnetic field parameters and solar flares, a dedicated instrument providing continuous observations, to monitor the evolution of active regions over several days, is required. The fields derived from polarimetric observations should be reliable and free from problems of Zeeman saturation and magneto-optical rotation in the strong field regions (these problems are typical in magnetographs which sample only one or two positions on the spectral line). Most of the existing magnetographs listed in Table 2.1 are affected by these problems except spectrograph based instruments and IVM of Hawaii, USA. To avoid these problems a magnetograph based on line profile scanning, like the one described in this thesis, is required. These observed profiles when fitted with theoretical profiles generated assuming appropriate solar models give reliable estimation of magnetic field parameters free from the problems mentioned above. However, obtaining such datasets is not very easy and requires lot of hardware and software resources and development time. With the developments in fields of camera detectors, electronics, computer processors, memory and disk-space, software development kits, optical, opto-mechanical systems etc. it is now possible to build such instruments with off-the-shelf components available commercially, which also saves time.

These developments in technology, the availability of large number of clear cloud-free observing days at Udaipur Solar Observatory, co-ordinated observations of flaring active regions with H-α observing facility of our observatory, and the fact that there is no operating imaging vector magnetograph in the country at present, motivated the development of the SVM instrument.

The outline of this thesis is as follows:

The second chapter highlights the design aspects of the solar vector magnetograph, developed at Udaipur Solar Observatory. The design of individual modules and laboratory evaluation of optical components is described. Most of the components that are used in the instrument are procured off-the-shelf. The design parameters of the individual modules and the estimation of final integrated performance is discussed. There were two phases of the project these are discussed one by one.

The third chapter describes the control software, developed for the SVM. The ingenious ideas used for integrating various software components (for each module) and a well established data analysis package are described. The integration of a data acquisition software with data analysis software allows on-line data visualizaton and processing. This feature provides great simplification in implementing customized data acquisition software.

The fourth chapter discusses the format of the observed data and the data-reduction techniques. The set of routines written to carry out post processing of SVM observations to arrive at the Stokes profiles of the observed region are discussed. A user friendly graphical interface specifically developed for performing data reduction and visualization is described. This interface makes data reduction process very easy to learn and saves time. Also, the interpretation of the observed Stokes profiles in terms of magnetic fields is discussed. A brief outline of the polarized radiative transfer theory is given and the methodology involved in deriving physical parameters in the line forming region using inversion of the profiles is discussed. Also, a software package for (i) performing transformation of vectors from observed frame to heliographic frame, (ii) calculation and display of potential (current free) field, (iii) resolution of 180° ambiguity by acute angle method, is developed.

The fifth chapter discusses an application of vector magnetic field observations in studying relationship between p-mode acoustic power and magnetic field topology of a large sunspot. The influence of magnetic field inclination on the acoustic power is studied separately in frequency band below and above the acoustic cutoff frequency. It is found that the acoustic power for strong fields $|B| > 1500$ G increases with increasing field inclination.

The final chapter gives a summary of the study done in this thesis. The preliminary results from the study of the sunspot helicity and its relation with chromospheric super-penumbral fibrils are discussed. Also, it discusses the limitations of the present version of solar vector magnetograph and proposes a new setup with improvements over present version. A webcam based autoguider developed for improved tracking of the telescope mount is described in the Appendix-A.

Chapter 2

Solar Vector Magnetograph Instrumentation

2.1 An Introduction to Solar Magnetographs

A solar magnetograph is basically an instrument which makes two-dimensional spatial maps of solar active regions in polarized light. The polarized radiation arises mostly due to Zeeman effect in solar spectral lines caused by solar magnetic fields. Since these polarization measurements are converted into magnetic field maps, these instruments are popularly known as magnetographs. The first modern magnetograph was developed by Harold Babcock (1953) and Kiepenheuer (1953) which made advancements in the study of solar magnetic fields. Since then routine measurement of line-of-sight magnetic field is being done in many observatories. The circular polarization, which gives information on the line-of-sight magnetic field, is relatively easier to measure. On the other hand, the linear polarization, which gives information on magnetic fields transverse to the line-of-sight is difficult to measure. There are two reasons for that: (i) major fraction of the solar magnetic flux emerging through photosphere is normal to the solar surface (for most of the observed solar disk except regions close to the solar limb) which leads to stronger circular polarization, and (2) Stokes-V (circular polarization) signal increases linearly with longitudinal magnetic field strength while Stokes-Q and U (linear polarization) signals are proportional to the square root of transverse magnetic field strength. Another, reason why linear polarization is difficult to measure is that the solar telescopes normally employ large mirrors (coelostats and heliostats) to deflect the light to a stationary platform. Thus, the instrumental polarization produced by the mirrors itself makes measurement of weak polarization signals difficult. However, by careful measurement of refractive indices of the mirror coatings and knowing the telescope angles during the day, a model of the telescope polarization is constructed and used to remove instrumental polarization offline from the observed data (Balasubramaniam, Venkatakrishnan and Bhattachayra 1985; Sankarasubramanian and Venkatakrishnan 2000). The measurement of polarization of light is done by encoding polarization states into intensity modulations and detecting the modulated signals using photoelectric devices. The early photoelectric V-polarimeter of Babcock consisted of an electro-optic light modulator (a KDP crystal). In this design the orientation of the crystal and the applied AC voltage are chosen in such a way that the circularly polarized part of the light becomes linearly polarized. Thus, an intensity signal which alternately originates from the right and left circular polarization passes the polarizer and enters the spectrograph. An electronic device measures the difference between the two signals passing through two exit slits in the spectral plane and this yields the V signal. These measured signals are then directly converted to magnetic field values by means of weak field approximation or by a fit to line profile to some specified form. Magnetograms have been obtained regularly since 1974 with the V-polarimeter installed at Kitt Peak vacuum Tower Telescope (Livingston et al 1976a,b; Jones et al 1992). Another alternative of modulating the the polarization is the rotating $\lambda/4$ plate first used by Kiepenheuer in 1953. The modulation must be either sufficiently fast so that the two intensities that are subtracted from each other are measured almost under the same atmospheric seeing conditions, or the measurement must be strictly simultaneous by means of a beam splitting device. Each scheme has its own advantages and disadvantages. If full Stokes vector is desired, the diverse states of polarization, namely Q,U and V, must all be encoded separately by appropriate phase retarders within each modulation cycle. Polarimeters based on different modulation schemes have been implemented in various observatories. Table 2.1 gives the characteristics of various magnetographs/spectropolarimeters that exist today. A review of Beckers (1971) lists 22 magnetographs, half of which are vector magnetographs. More recent instruments are the Advanced Stokes Polarimeter (ASP; Elmore et al. 1992; Skumanich et al. 1996) at Sacramento Peak Observatory, as well as the La Palma Stokes Polarimeter (LPSP) and the Tenerife Infrared Polarimeter (TIP), both described by Martinez Pillet et al (1999). The Zurich Imaging Polarimeter ZIMPOL I and ZIMPOL II (Gandorfer and Povel 1997; Stenflo et al 1998; Povel et al 1998; Stenflo 2006) uses a CCD chip itself as a demodulator: within each modulation period one out of each four rows is exposed successively to the four signals; the other three rows are masked and serve as buffers before readout. The Imaging Vector Magnetograph (IVM) at Hawaii (Mickey et al. 1996) uses tunable Fabry-Perot and builds two-dimensional polarized spectra by scanning in wavelength. The Diffraction Limited Spectro-Polarimeter(DLSP) at Dunn Solar Telescope (DST) NSO, Sac Peak is similar to ASP but is flexible to observe at different resolution scales down to diffraction limit, since it is equipped with high-order adaptive-optics (Sankarasubramanian et al., 2006).

Depending on the goal of study, there are two options used for spectrum analysis of the polarized light. These are (i) a narrow band filter like a Fabry-Perot etalon, Lyot filter, Universal bi-refringent filter or a combination of them, and (ii) a slit spectrograph. In the former method instantaneous two-dimensional mapping of narrow-band polarization is done and profiles in wavelength are made by tuning the filter. In case of slit spectrograph the spatial information along only one direction, i.e., along the slit direction is obtained instantaneously and the two-dimensional map is made by scanning the slit over the active region. However, the spectral profile of the region sampled by the slit is obtained instantaneously. Also, the spectral resolu-

Table 2.1: A list of operational vector magnetographs around the world shown along-with their mode of operation and spectral lines.

Instrument	Polarization Modulator	Spectral Isolator	Spectral Line
Mitaka, Japan.	Quartz	Bi-refringent Filter	Fe I 525.0 nm
IVM, Hawaii, USA.	LCVR	Fabry-Perot Etalon	Fe I 630.2 pair
HSOS, China.	KD*P, Quartz	Bi-refringent filter	Fe 525.0 nm
Huntsville, USA.	KD*P, Quartz	Bi-refringent filter	Fe 525.0nm
Big Bear, USA.	LCVR	FP etalon	Fe 630.2nm
ASP, Sac Peak, USA	Quartz	Spectrograph	Fe 630.2 nm
			Mg b1, b2
ZIMPOL, Switzerland	PEM	Spectrograph	multi-line
THEMIS, Spain	Quartz	Spectrograph	Multi-line
TIP, Tenerife	LCVR	Spectrograph	Infra-red
SOLIS	LCVR	Spectrograph	Fe 630.2nm
POLIS	LCVR	Spectrograph	Fe I 630.2nm
			Ca H and K

tion of spectrograph based instruments is generally higher than filter based instruments. As a consequence, the filter based instruments are better suited for making observations with good time resolution but modest spectral resolution, whereas spectrograph based instruments are better suited for detailed high spectral resolution observations of limited field of view. For studies related to dynamics and evolution of target region and magnetic field changes in relation to solar flares and other activity phenomena, the filter type magnetographs are preferred. While, for studying detailed physical parameters of small-scale solar structures, slit-spectrograph based instruments are more suitable.

2.2 Earlier Magnetograph at USO

Magnetic field measurement started at Udaipur Solar Observatory in 1996, with a solid state Fabry-Perot etalon made up of electro-optic LiNbO3 (Lithium Niobate crystal), used for measuring narrow-band circular polarization. The polarimeter was a KD*P based electro-optic modulator and the detection was done in real time using a dedicated frame grabber, a video camera and an on-board image processing system. This was the first magnetograph at Udaipur Solar Observatory, and was called USO Video Magnetograph (VMG) (Mathew et al. 1998a,b). Further progress in the magnetic field measurement at USO came with the development of an instrument capable of two-dimensional imaging spectroscopy and complete Stokes vector determination. This instrument is called Solar Vector Magnetograph (SVM) and has been successfully tested at Udaipur Solar Observatory during 2005. The SVM employs symmetric optics for minimal instrumental polarization and a dual beam analyzer for avoiding seeing induced spurious signals. The spectroscopy is done by a Fabry-Perot etalon together with a narrow-band interference filter. The Fabry-Perot etalon is a tunable air-gap piezo-driven servo-controlled system from M/s IC Optical systems (formerly M/s Queensgate). The development of the SVM forms a significant part of this thesis work. In this chapter I present design of this filter based magnetograph which is capable of making observations relevant for studying evolution of magnetic field vector and velocity field of solar active regions. In the following sections I shall describe details of the instrument and its various subsystems.

2.3 Solar Vector Magnetograph

The design of SVM like any other magnetograph includes following considerations, (i) spatial resolution and field-of-view, (ii) spectral resolution, (iii) time resolution, (iv) instrumental polarization, seeing errors, and sensitivity. The design parameters of any instrument are driven by the goal of scientific study one wants to do with the instrument. The observing conditions at Udaipur Solar Observatory are favourable for studying solar flares due to large number of cloud-free clear observing days and existing H-α flare patrol telescope. Thus, the vector field measurements along with high-cadence H-α provide very useful observations for flare research.

However, there are always some trade-offs that are made in instrument design in order to match the overall system performance. For example, the camera readout rate may be fast but the tunability of the filter may not be that fast or vice-versa, therefore, making few trade-offs is generally inevitable. In the following paragraph we discuss these design parameters in relation to SVM.

- **(i) Spatial resolution and Field-of-view** : For studying the active region (AR) magnetic field structure it is desirable to cover an entire active region, as the field evolution may take place anywhere in either of the polarities. The typical size of an AR is about 4 x 4 arc-min^2. However, in the design of SVM the parameters that constrain the FOV are (a) filter pass-band shift as well as broadening with angle-of-incidence, (b) physical beam separation due to calcite analyzer (Savart plate), and (c) the CCD chip size. Under these constraints, the field-of-view (FOV) of SVM is a circle of 3 arc-minute diameter, with a modest pixel size of one arc-sec, that is compatible with the "seeing" at USO (Brajesh et al. 2007).

- **(ii) Spectral Resolution**: The spectral resolution of the narrow band filter system of the SVM is 52,500 measured at 6300 Å, which corresponds to a FWHM of 125 mÅ. For making studies in different wavelengths and performing a wavelength scan it is desired that the filter should have (a) rapid tunability, and (b) good spectral coverage. In SVM these parameters correspond to response time of 0.2 milliseconds and spectral coverage from 5500 to 7000 Å.

- **(iii) Time Cadence**: It is desirable to make complete Stokes measurement with reasonable sensitivity as fast as possible for studying the dynamics of vector fields. However, the time resolution is limited by (a) the solar 5-minute oscillations, i.e., one should finish scanning the wavelength before the spectral line shifts considerably due to 5-minute oscillations, (b) time taken by polarization modulator/camera system to complete one cycle of observation. In SVM a complete observation cycle means making three spectral scans at three fixed orientations of $\lambda/4$ plates, corresponding to Stokes Q, U and V parameters. The duration of each wavelength scan depends on exposure time of the camera and the number of wavelength samples across the spectral line. In SVM, a wavelength scan of 21 points across the spectral line with exposure time of 100 milliseconds takes 15 seconds. Let us call this time T_{scan}. Thus, a SVM observation cycle with this type of wavelength scan takes three times T_{scan}. This together with time taken for positioning the wave-plates between each measurement comes to be 1 minute on an average. This value is typical of SVM observations done for single line Fe I 6302.5 Å with 21 point wavelength scan and exposure time of 100 milliseconds.

- **(iv) Instrumental Polarization, Seeing errors, and Sensitivity**: The sensitivity of a polarimeter depends on (a) number of integrations: The number of integrations in a wavelength scanning magnetograph is limited by the 5-minute oscillation. The time required to do a wavelength scan in all Q, U, or V, must be accomplished in a small fraction of 5-minute oscillation period. This time, in turn, depends on the number of wavelength samples taken for each scan. As mentioned in the previous section, a complete cycle of Stokes measurement takes one minute on an average, including the time taken to rotate the wave-plates. This is a small fraction of 5 minute p-mode oscillation period. So, in order to build up the signal-to-noise ratio of the measured polarization one can integrate limited number of frames due to 5-minute oscillation constraints. However, one can repeat several one minute cycles and add the profiles later to reduce the noise. The number of such integrations is limited by the evolution time of the active region.

  The telescope optics consists of an eight inch Schmidt-Cassegrain telescope from M/s Celestron (a C-8 model). The entire optical system is mounted on a German Equatorial mount pointing directly toward the Sun. The straight and symmetric optical design telescopes have intrinsically very low instrumental polarization. The on-axis polarization of the symmetric William Herschel Telescope, as determined by observing bright stars with polarimetric accuracy of few parts in 10^{-7}, is only $\approx 15 \times 10^{-6}$ (Hough et al. 2006). Since this instrument aims to measure strong magnetic fields of the solar active regions, where polarization signals are relatively higher, we neglect the telescope polarization as it is expected to be relatively very small. Another major source of polarimetric error is seeing induced spurious signals. In SVM we address this problem by using a dual beam calcite analyzer (Savart plate) to minimize seeing induced errors. Even here differential crystal aberrations lead to measurement errors. These can be reduced by exchanging the two beams by flipping the polarization states and then averaging the two signals.

2.4 Optical layout of SVM

The schematic layout of SVM optics and control modules is shown in figure 2.1. Basic modules are (a) Schmidt-Cassegrain telescope tube, (b) rotating wave-plate polarimeter, (c) tunable narrow-band Fabry-Perot filter, (d) Calcite analyzer (Savart Plate) and (e) a cooled CCD camera. The primary imaging is done using a Celestron C-8 (TM) Schmidt-Cassegrain telescope of 8 inch aperture. The telescope focal length is 2032 mm and the resulting output beam is a f/10 beam. In order to avoid the excessive heating of secondary mirror due to large solar flux, the entrance aperture of the telescope is covered with an 8 inch broad-band interference filter of 150 Å bandpass centered at 6300 Å wavelength. The maximum transmission at the central wavelength is 60%. The telescope makes full-disk image of the sun at the prime focus. The field-of-view is selected at the circular aperture-stop located at the prime focus. The beam from the selected field-of-view then diverges through the polarimeter optics. This beam is collimated by an achromatic lens of focal length

180 mm. The Fabry-Perot etalon and order-sorting narrow-band filter are kept in the collimated beam. The order sorting filter is a two-cavity interference filter from M/s Andover corporation of pass-band 4 Å centered at 6302 Å. After passing the filter assembly the beam is re-imaged onto the CCD chip using an achromat of focal length 500 mm. The dual-beam calcite analyzer is kept just before the CCD camera for polarization analysis. The modules of the SVM optics are described in the following sections.

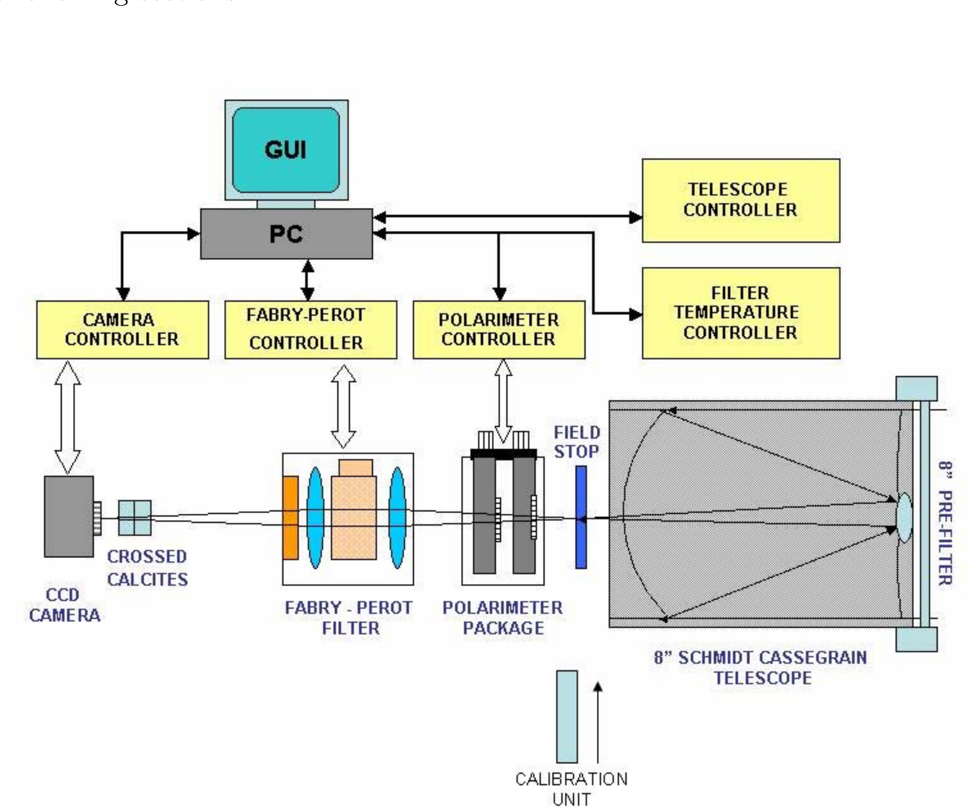

Figure 2.1: A schematic layout of the optical and control system of the Solar Vector Magnetograph.

2.5 Polarimeter Module

The polarimeter of SVM is based on the design of the polarimeter used in French-Italian THEMIS telescope (French acronym stands for Telescope Heliographhique pour l'Etude du Magnetisme et des Instabilites Solaires) (Bommier and Rayrole, 2002). It consists of two quarter wave-plates mounted on a motorized rotary stage of high resolution and accuracy. The Stokes Q, U and V signals are measured by orienting the optic axis of the waveplates according to the values given in Table 2.2. The modulated signal is analyzed by a dual-beam calcite analyzer placed in front of CCD camera. This makes two displaced images of the selected field-of-view on the same camera chip representing orthogonal polarization states.

2.5.1 Quarter Waveplates

The two quarter wave-plates used in the SVM polarimeter are fixed retardance crystal wave-plates. These are compound zero-order retarders assembled from pairs of optically contacted crystalline quartz plates (c-axis cut) and were procured from M/s Melles Griot. The quartz plates have orthogonal optic axis directions, therefore, the roles of ordinary and extraordinary rays are interchanged in passing from one plate to another. Net retardation is essentially temperature invariant since both plates are nearly equal in thickness. This is an important consideration for us, since the ambient temperature of Udaipur varies over a large range, especially during summer. The temperature coefficient for these waveplates is less than 0.01 nm per °C. Also, the wave-plates are designed for 632.8 nm HeNe laser line. However, their use at Fe I 630.2nm will cause a perfect 90 degree phase retarder to give a retardance of 89.63 degrees only, due to wavelength difference of 2.6 nm. The other parameters of importance for these wave-plates, as specified by the manufacturer, are given in Table No 2.3.

In present design the retarders are not kept in collimated beam to avoid the ghost images due to the reflections from the back surface of waveplates. Further, the polarimetery is done in diverging beam. This has two effects, first, the retardance varies across the field-of-view (FOV). For the three arc-min FOV of SVM and 2mm thick wave-plate this corresponds to retardance variation of only 0.2° at 632.8 nm. Secondly, the value of retardance has a spread around a mean value. The amount of spread depends on half of cone-angle of the diverging beam. In our case for *f/10* beam the half cone-angle is 2.8°, which corresponds to a variation of 1° in retardance. These variations in retardance are of the order of retardance tolerance specified by the manufacturer, that is about ±1°.

Table 2.2: Waveplate orientations for the polarimeter

Stokes parameter	Waveplate 1	Waveplate 2
I±U	135^o	135^o
I∓U	90^o	90^o
I±Q	135^o	90^o
I∓Q	135^o	180^o
I±V	45^o	270^o
I∓V	135^o	0^o

We have evaluated two important parameters of the waveplates in the laboratory before using them in the polarimeter, these are the retardance and the orientation of optic axis. The measurement of the phase retardance of a waveplate (WP) can be done in a variety of ways. The simplest technique is to place the WP at 45 degrees between two crossed polarizers and rotate the analyzer and measure the intensity in orthogonal directions then the difference divided by sum of these intensities is equal to the cosine of the retardance of the plate in radians. However, photometric inaccuracies, like the fluctuations in the light source used for the testing and the linearity and noise in the photo-detectors limit the accuracy of measurements in this technique. With the advent of modern two dimensional CCD detectors coupled with interferometric techniques like using a Babinet compensator method, retardance measurements can be done with good accuracies. The method that we used for the determination of these two parameters is based on a technique that uses Babinet compensator and CCD camera (Sankarasubramanian and Venkatakrishnan, 1998). It is possible to determine the retardance values of waveplates using this technique with accuracy of better than 0.5 °. The essence of the technique is that the fringe pattern produced by the Babinet compensator when placed between two crossed polaroids is imaged onto a CCD detector. Now, when a retarder is introduced in between the two polaroids the fringe pattern shifts by an amount proportional to the retardance of the retarder. This retarder is now rotated in small increments and the resulting shifts in the fringe pattern is measured as a function of rotated angle. Note, that in this technique the fluctuations in the intensity do not affect the position of the fringe pattern and hence do not directly affect retardance measurement. Another advantage of this technique is that it is based on the fringe shift detection, which can be accomplished to sub-pixel accuracies by phase matching algorithm (Wang et al., 1996). We have used this technique for checking the retardance values and the orientation of the optic axis of these waveplates. The values are found to be correct and are as per the manufacturer's specifications i.e., $\delta = 90° \pm 1°$. Our retardance measurement accuracy was not better than 1 degree because the optical setup and CCD pixel size did not allow better sampling of the fringes.

2.5.2 Nanorotator Rotary Stages

The optic axis of the quarter waveplates used in the polarimeter are oriented with the help of high precision rotary stages. These rotary stages are off-the-shelf NanoRotator^{TM} rotary stages of M/s Melles Griot Inc, shown in figure 2.2. These stages provides 360 degrees of rotation and can be used in either a vertical or horizontal orientation. Powered by a high-resolution stepper motor, it is constructed with a thin-walled bearing design that provides highly accurate rotation with minimum wobble and eccentricity. A mechanical switch generates a reference signal for each complete rotation. It has a central 50-mm-diameter access hole, which allows quarter waveplates to be mounted for modulation. The load carrying capacity of these stages is upto 50 Kg. Whereas their own weight is about 1.4 Kg. The positioning resolution claimed by the manufacturer after feeding the calibration table in the controller microprocessor is about 1 arc-sec. The stepper motor driving NanoRotator^{TM} stages is controlled by the NANOSTEP^{TM} Control Unit, which consists of a dedicated microprocessor. The controller drives stepper motor which actuates an axis that is fitted with a feedback transducer. The controller uses calibration information to correct for any backlash in the positioning devices. The advantage of using these stages is their good repeatability and accuracy which are very important in minimizing misalignment of polarization optics thus reducing crosstalk errors.

Table 2.3: Specifications of Quarter Wave-plates

Parameter	Value
Wavelength	632.8 nm
Material	Crystal quartz, c-axis cut
Retardation Tolerance	$\lambda/500$
Wavefront Distortion	$\lambda/10$ peak to valley at 632.8 nm
Diameter	30mm +0/-0.15mm
Parallelism	0.5 arc-seconds
Surface Quality	20-10 scratch and dig

2.5.3 Dual Beam Calcite Analyser

A calcite beam-displacing prism give out two parallel, but laterally displaced, orthogonally polarized output beams from one unpolarized input beam. If the input beam is linearly polarized, the output can be made to vary continuously and sinusoidally from one parallel beam to the other by rotating the input polarization angle. The ordinary beam is undeviated. In SVM polarimeter the detection of the modulated polarized light intensity is done by a Savart plate. A Savart plate consists of two calcite beam displacing crystals crossed to each other so that the roles of ordinary and extraordinary rays are exchanges in the second calcite. This scheme has been discussed extensively and used by Semel et al. (1987,1993) and Donati et al (1990, 1999). The advantage of using such an analyzer is the simultaneous

Figure 2.2: The picture shows the nanorotator stages used to drive the quarter waveplates to the respective orientations.

detection of orthogonal Stokes parameters. Thus, the errors in measured polarization due to temporal variation of atmospheric seeing are removed and there is no need for fast modulation and demodulation. This in turn allows for large integration times and leads to an improved signal-to-noise ratio. However, this scheme is not absolutely free of errors, the main sources of error are (i) the error in co-alignment of two images formed on the detector, (ii) detector imbalance, i.e., the error in gain correction of two beams, (iii) differential optical aberrations in the two beams due to different optical path traversed in the calcites. However, the scheme is very effective in measuring polarization signals upto $10^{-3} \times I_c$ levels using "beam exchange" method even with slow modulation systems (Donati et al, 1990; Bianda et al, 1998; Donati et al, 1999). The so called "beam exchange" method combines two sets of observations in which the two orthogonal beams in the polarimeter are flipped using a half-wave plate and the combination of four measured intensities removes the effect of transmission changes and differential gain variations of different detector areas

Table 2.4: Specifications: Calcites

Parameter	Value
Wavelength Range	350-2300 nm
Optical Material	Optical Grade Calcite
Total Output/Total Input	
350nm	35-40%
400nm	65-70%
500nm	>80-88%
Clear Aperture	10×10 mm
Extinction Ratio	1×10^{-4}
Outer Diameter (ϕ)	25 mm
Length (L)	34.9mm
Beam Displacement at 500 nm	3.3 mm
Surface Quality	40-20 scratch and dig
Centration	3 arc-minutes
Dimensional Tolerance	Length $\pm$ 0.2mm

(Keller, C. 2002; Venkatakrishnan, P. 2003).

The calcites used in SVM polarimeter are from M/s Melles Griot Inc. and their characteristics are given in Table 2.4. The extraordinary beam is deviated by 6 degrees within the prism. Upon exit, the extraordinary beam is again parallel with the input beam and the exiting ordinary beam. Single-layer MgF_2 anti-reflection coatings are applied to both faces of the calcites. The schematic of these calcites is shown in figure 2.2.

The deployment of the two calcites crossed to one another requires great care. Since, the two orthogonally polarized beams coming out of the crossed calcites (assuming the optic axis of the two calcites are horizontal and vertical respectively) are not displaced vertically or horizontally, but rather are separated so as to make an angle of 45 degrees to the CCD chip. Therefore one has to read twice as large CCD area now as compared to the case where the two images were one above the other or side-by-side. To solve this problem either one has to rotate the camera by 45 degrees, or rotate both of the calcites together by 45 degrees in the same direction. Rotating the camera adds a problem of rotated image and hence needs offline de-rotation. However, rotating the calcite assembly is simpler and is followed in our design. This changes the reference axis of the polarimeter system and the orientations of QWPs are measured relative to this reference axis.

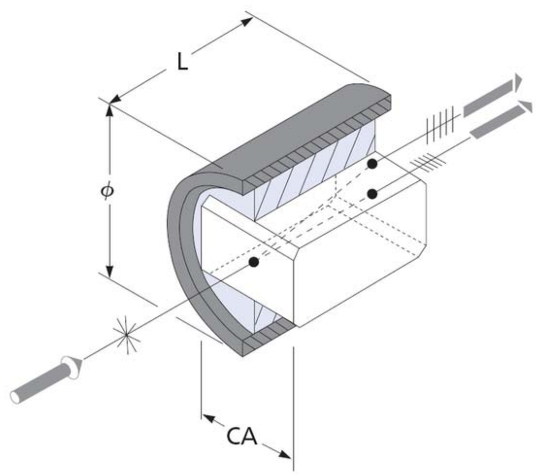

Figure 2.3: This figure shows the schematic of calcites used in dual beam analyser

2.5.4 Polarimeter Calibration

The polarimetric data as measured by the polarimeter needs to be calibrated for cross-talks resulting in the polarimeter itself and instrumental polarization. The relation between the incoming Stokes vector and measured Stokes vector can be written as

$$S_{out} = X \cdot T \cdot S_{in} \tag{2.1}$$

Where, S_{in} and S_{out} are input and measured Stokes vectors respectively. The 4×4 matrices T and X are telescope Mueller matrix and polarimeter response matrix respectively. Since the SVM employs a symmetric telescope with no oblique reflections the telescope polarization T is expected to be minimal. Further, by looking at the disk center quiet regions in continuum, we have not detected any instrumental linear or circular polarization up-to 0.05 % of continuum intensity level. This sets an upper limit to the instrumental polarization. Since the goal of the instrument is to measure the magnetic fields of the active regions and sunspots, where the polarizations are much higher and the typical noise in the continuum for a single exposure sequence is dominated by photon noise and seeing errors, the telescope polarization T for SVM has not been taken into account during data reduction. Hence the equation above reduces to

$$S_{out} = X \cdot S_{in} \tag{2.2}$$

Thus, in order to calibrate the polarimetric data the response matrix of polarimeter, X, needs to be determined. In the following section the measurement procedure of response matrix X of the polarimeter is described. The final accuracy of the observations depend on the quality of calibrations.

2.5.4.1 Measurement of polarimeter response matrix

For calibrating the SVM polarimeter a calibration assembly (CA) is deployed just after the prime focus of the telescope and before the polarimeter module. The CA consists of a polarizer and a quarterwave retarder mounted on a precise computer controlled rotary stage. The orientation of the calibrating optics can be controlled to an accuracy of better than 0.01 degrees with a repeatability of 0.1 degrees. The orientation of the axis of the polarizer is determined by first removing the polarimeter from the beam and then introducing the CA polarizer and rotating it through 180 degrees in steps of 5 degrees. The calcite analyzer in front of CCD camera then modulates the beam and the axis of polaroid relative to calcite axes is immediately determined. This also determines the degree of polarization of the polarizer. Similarly for determining the axis of retarder, the CA polarizer is first crossed to the analyzer axis and retarder in inserted into the optical path and rotated through 180 degrees in steps of 5 degrees. The modulation of the beam once again gives the axis of retarder readily. This also gives the measurement of the retardance of the CA retarder by fitting a simple model. Here, the polarizer is assumed to be an ideal polarizer and it is assumed that the optics between CA optics and calcite analyzer i.e., the filters, relay lenses, pre-filter and Fabry-Perot etalon does not change the polarization state of the light. These simple assumptions and the imperfectness of CA optics or errors in their knowledge limit the accuracy of the calibrations. With the axes of CA optics known the input Stokes vector can be calculated for a given orientation of the CA optics. The continuum solar light from defocused quiet sun disk-center through a narrow band pre-filter centered at Fe I 6302.5 $\mathring{A}$ is used for calibrations. The relation between the incoming Stokes vector from the Sun and the measured Stokes vector is given as

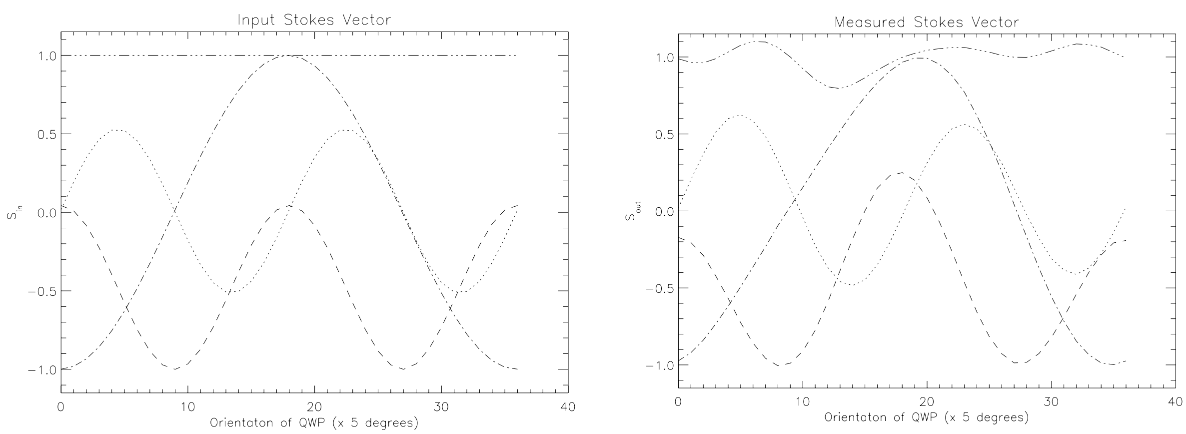

Figure 2.4: The left panel shows the calculated Stokes input vector from the known properties of the input polarizer and retarder and the right panel shows corresponding observed Stokes parameters as a function of retarder orientation. The Stokes parameters I,Q,U and V are represented as dash-dot-dot-dashed, dotted, dashed, and dash-doted respectively.

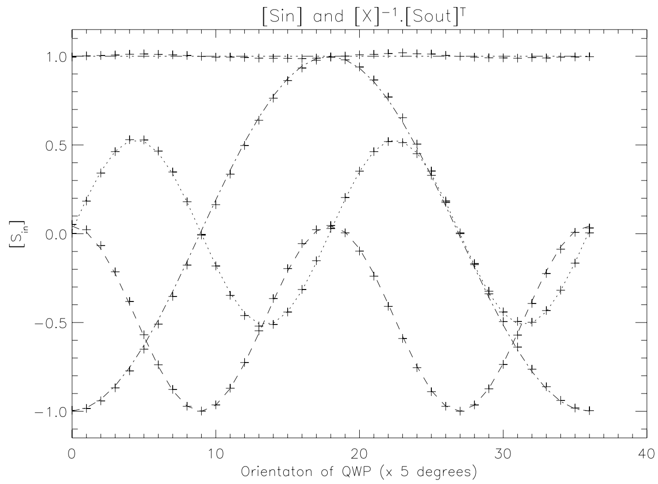

Figure 2.5: Observed Stokes parameters corrected for polarimeter response matrix are shown together with theoretical input Stokes vector.

$$S_{out} = X \cdot M_\delta(\theta_\delta) \cdot M_p(\theta_p) \cdot [1, 0, 0, 0]^T \tag{2.3}$$

where θ_δ and θ_p are the orientations of the retarder and polarizer of the CA relative to the reference axis which is taken to be the terrestrial North-South direction. Here the input Stokes vector is taken as unpolarized light, this however, is not very important as the CA polarizer orientation is kept fixed during calibration and retarder orientation is changed in steps of 5 degrees through 180 degrees. The theoretical and measured Stokes vector at each CA retarder orientation is shown in fig 2.4.

The polarimeter response matrix is calculated by writing the input (calculated) and output (measured) Stokes vectors at each retarder position θ_δ, in form of two 37×4 matrices. Let us call these input and output matrices as A and Y respectively. Thus

$$Y = X \cdot A \tag{2.4}$$

$$A^T \cdot Y = A^T \cdot A \cdot X^T = D \cdot X^T \tag{2.5}$$

$$X^T = D^{-1} \cdot A^T \cdot Y \tag{2.6}$$

where X is the desired polarimeter response matrix. This method has been adopted from the calibration scheme of Polarimetric Littrow Spectrograph (POLIS) instrument at Vacuum Tower Telescope (VTT) , Tenerife (Beck et. al., 2005). A typical response matrix, determined from the input and output Stokes vectors as shown in fig. 2.4, is given below

$$X = \begin{bmatrix} 1.000 & 0.1118 & -0.0107 & -0.0433 \\ -0.0142 & 0.9927 & -0.1651 & -0.0386 \\ -0.0084 & -0.03623 & 0.9892 & 0.2177 \\ -0.0065 & 0.2308 & -0.0436 & 0.9807 \end{bmatrix}$$

Thus the incoming Stokes vector can be approximated from the observed Stokes vector and measured response matrix as follows

$$\tilde{S_{in}} = X^{-1} \cdot S_{out} \tag{2.7}$$

The resulting $\tilde{S_{in}}$ determined from $X^{-1} \cdot S_{out}$ is shown in figure 2.5. The uncertainty in measurement of X arises due to uncertainties in knowledge of calibration optics parameters. The error in the calibration is obtained by evaluating the total deviation of the fit and is given as

$$\bar{\sigma}^2 = \frac{1}{N} \sum (Y - X \cdot A)^2 \tag{2.8}$$

This variance is of the order of 1.3 $\times$ 10^{-4} in our case.

2.6 Narrow-band imaging filter system

The filter based magnetographs have the advantage of good time resolution over spectrograph based instruments. They are capable of providing vector magnetograms of a full active region in a few minutes, as compared to several minutes by a spectrograph based instrument. However, the chief limitation of filter-based imaging magnetographs is their lower spectral resolution and limited wavelength sampling, sometimes done only in one of the wings of the line. As a result they suffer from Zeeman saturation problem for strong field regions and the magnetograph calibration becomes non-linear for strong fields. This problem is not present with instruments capable of measuring polarization across the complete spectral line. This means the filter should have tunability range long enough to make a wavelength scan of the entire spectral line. Also, this should be done quickly to avoid spectral line smearing due to 5-minute p-mode oscillations on the sun. There are many options available for a narrow band filter like, Lyot bi-refringent filters, magneto-optical filter, Michelson interferometer, Fabry-Perot interferometer etc. We considered only two choices, since these were readily available to us, i.e., (i) a solid electro-optic tunable LiNbO3 etalon, and (ii) an air-gap servo-stabilized tunable etalon.

2.6.1 Brief overview of Fabry-Perot Interferometers

During the last decade a number of instruments have been developed using the Fabry-Perot (FP) etalons as the tunable narrow band filters for obtaining the monochromatic images of the sun in selected wavelength bands (Bendlin et al 1992; Kentischer, 1998; Debi Prasad et al., 1997). The stratospheric balloon and space borne instruments have also used the FP etalons for obtaining the magnetograms and dopplergrams of the active regions (Rust, 1985; Socker et al., 1996). The advantage of FP based narrow band filters over traditionally used birefringent filters is greater transmission and simplicity in manufacturing. Also, FP based filters are of lower cost. Mainly, two types of etalons are used in solar applications. One of them is made out of electro-optic crystals such as LiNbO3 and are polished and coated on both the sides that act as the optical cavity. These etalons are tuned by applying electric voltages across the surface perpendicular to the transmission axis, which changes the refractive index between the reflecting surfaces. However, there is a limit to the applied voltages, which is generally 3000 Volts for LiNbO3. Therefore, it is possible to tune only a part of the Free Spectral Range (FSR) limited by the highest voltage that the crystal can tolerate. In many cases, the application of excess voltage has damaged the etalon wafers. In a typical crystal the tunability being 0.5 Å per thousand Volts (Mathew et al., 1998a;1998b), with full tuning range of only about 3 Å. The other type of filters used are servo-controlled tunable etalons. These etalons consist of two plates with an air gap and are supported by three piezo-electric stacks. The optical spacing is monitored by capacitance micrometers. With a servo loop the parallelism between the two plates is maintained to a high degree of accuracy resulting in high finesse and stability. The scanning is achieved by applying the voltages to the piezo-electric crystals (Kentischer, 1998; Balasubramaniam, 2002).

2.6.2 Comparison of a solid and air-gap etalon

In this section we compare two Fabry-Perot etalons belonging to the two categories described above having similar finesse of about 30. An identical laboratory setup was used to evaluate the instrumental parameters of the two etalons. We find that although the LiNbO3 etalon has limited tunability it has wider acceptance angle. However, greater care must be taken to use them because they are mechanically fragile.

Figure 2.6 shows that the shift and the broadening of the transmission profile of the two etalons as a function of tilt angle. As may be noticed the wavelength shifts slowly with respect to the tilt angle in case of solid etalon as compared to the piezo-electric servo controlled air gap etalon. The relation between the wavelength shift $\delta\lambda_r$ with the tilt angle θ for a given wavelength λ can be expressed as

$$\frac{\theta^2}{8} = \mu^2 \, \frac{\delta\lambda_r}{\lambda} \tag{2.9}$$

where μ is the refractive index of the cavity. This shows that the θ dependence of the wavelength shift is independent of optical gap and depends only on the refractive index. The μ for LiNbO3 is 2.297 (ordinary) and 2.208 (extraordinary). Therefore, for a given wavelength the shift $\delta\lambda_r$ is inversely proportional to μ^2. Taking the ordinary refractive index for the z-cut LiNbO3, we find that for a given angle the acceptance angle for solid etalons is about 4.5 times more compared to air gap etalon. This is consistent with our observations. Therefore, for wide field applications it may be advantageous to use LiNbO3, when it is required to image at a few selected wavelengths. Also, wider acceptance angle is advantageous regarding the problem of pupil apodizations (Lühe and Kentischer, 2000). Although the wide-field capability is not realizable their rapid tunability all through the FSR makes the piezo-electric etalons suitable for making universal filters. The comparison of tunability of two FPs was done in laboratory and the channel spectra are shown in figure 2.7. However, as the FSR is a function of plate separation, the tunability of LiNbO3 etalon may be increased by using thinner wafers, however, there are practical difficulties in manufacturing thin wafers. Another advantage of piezo-electric system is that due to the closed loop servo control mechanism the cavity parallelism can be adjusted to a high order of accuracy. On the other hand, in case of LiNbO3 etalons the initial parallelism achieved at the time of manufacture remains practically unchanged over several years, about ten years in the present case. While comparing these two types of etalons we may mention that there exists other benefits of air spaced piezo tunable etalons apart from the ones mentioned above. It is possible to make piezo-electric etalons with very narrow gaps, of the order of 10 μm or less which allows a double or triple etalon system to be made with very high spectral resolution (Kentischer et al, 1998; Tritschler et al. 2002). Also, it is possible to make apertures that are considerably bigger (150 to 200mm) at the resolution that are useful.

2.6.3 Fabry-Perot system of SVM

The narrow-band imaging filter of SVM consists of a Fabry-Perot interferometer and an order sorting pre-filter. The manufacturer of the Fabry-Perot etalon is M/s ICOptical systems Inc, U.K., formerly known as M/s Queensgate Inc, U.K. This type of etalon was first introduced by Hicks et al (1976). In this etalon the active

Table 2.5: Etalon Properties

$LiNbO_3$ Etalon Properties	
Substrate Material	Z-cut $LiNbO_3$
Substrate diameter	73.6 mm
Usable Aperture	30 mm
Etalon Thickness	175 μm
Coating	Multilayer broad band,
	hard ion assisted deposition
	of SiO_2, Ta_2O_5, ITO
Reflectivity	0.95 at λ=6120 Å
Voltage sensitivity	0.45 Åper 1000 Volts
Piezo-Electric Etalon Properties	
Substrate Material	Fused Silica
Type	ET50 IC Optics inc.
Usable Aperture	50 mm
Etalon spacing	488 $\pm$ 3 μm
Plate Flatness	λ/200
Coating	Multilayer dielectric coating
Reflectivity	0.96 at λ=5500-7000 Å

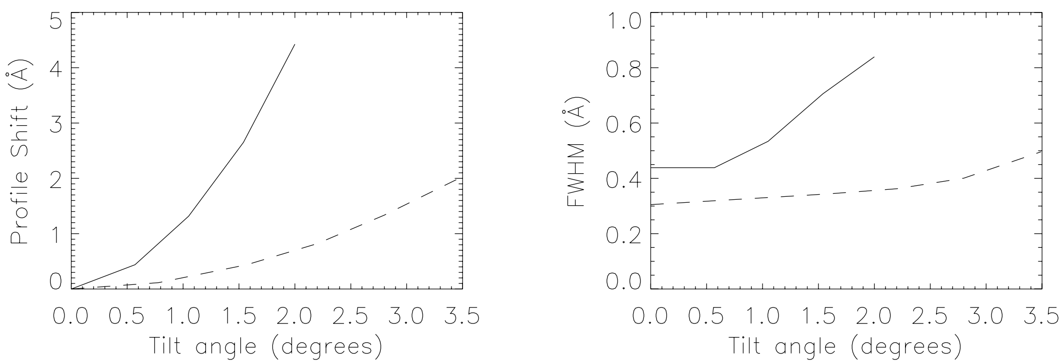

Figure 2.6: The plot (left) shows the shift in the peak transmission profile with tilt angle and the plot (right) shows the change in FWHM of the transmission profile with tilt angle.

control element determining the etalon gap separation does not depend on the optical properties of the etalon gap. Instead, a gap sensing capacitance micrometer is used for sensing the cavity spacing (Hernandez and Mills 1973). The change in capacitance with physical spacing is measured, and the servo loop then is used to control this capacitance.

The etalon has 50 mm clear aperture. The The FP is kept in a collimated beam, as a result of which there is an amplification of angles by a factor of 11. The FWHM of the transmission band of FP is determined to be about 125 mÅ using laser in laboratory and also using telluric lines formed in Earth's atmosphere (figure 2.8). The collimated design suffers from problem of spectral shift across the field-of-view but offers better spectral resolution than telecentric design and is more compact in size. The spectral shift over the FOV is not a problem as full line profiles are made by scanning the wavelength. The adjacent transmission peaks of the FP are blocked using a narrow-band interference filter. This filter is a two cavity filter with a pass-band of 0.35nm. The filter is kept in a temperature controlled oven with temperature stability of $\pm 0.5°$C.

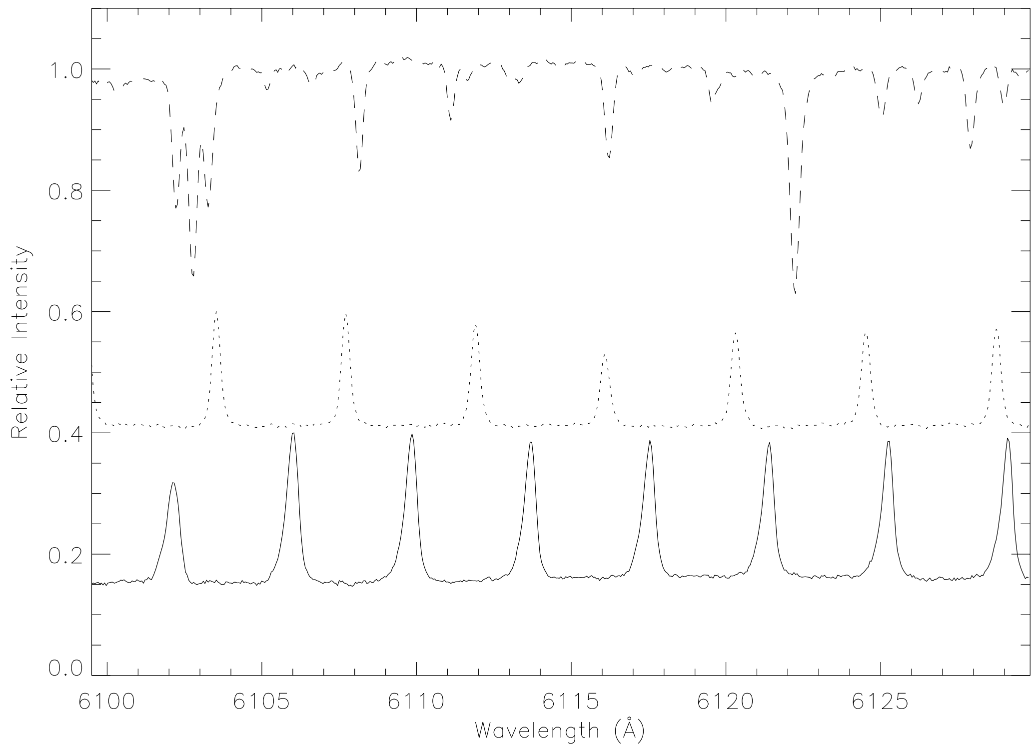

Figure 2.7: The typical channel spectrum of the etalons along with the solar spectrum. The solid line corresponds to the piezo-electrically controlled servo controlled etalon while the dotted line represents the channel spectrum for LiNbO3 etalon. The solar spectrum is given at the top in dashed line.

2.7 Digital CCD Camera

The CCD camera is a cooled scientific grade camera procured from M/s Apogee Inc. (Model AP6E camera). The camera uses a Kodak KAF 1001E image sensor consisting of 1024x1024 pixel array with square pixel of size 24 μm. The pixels are digitized up-to 14 bits at a speed of 1MHz. Typical readout time for full frame, without binning, is about 1.3 seconds. The camera is interfaced to the computer by a PCI card which also gives power supply to the camera. The camera has a thermo-electric and forced-air cooling system capable of cooling the chip to -20 °C.

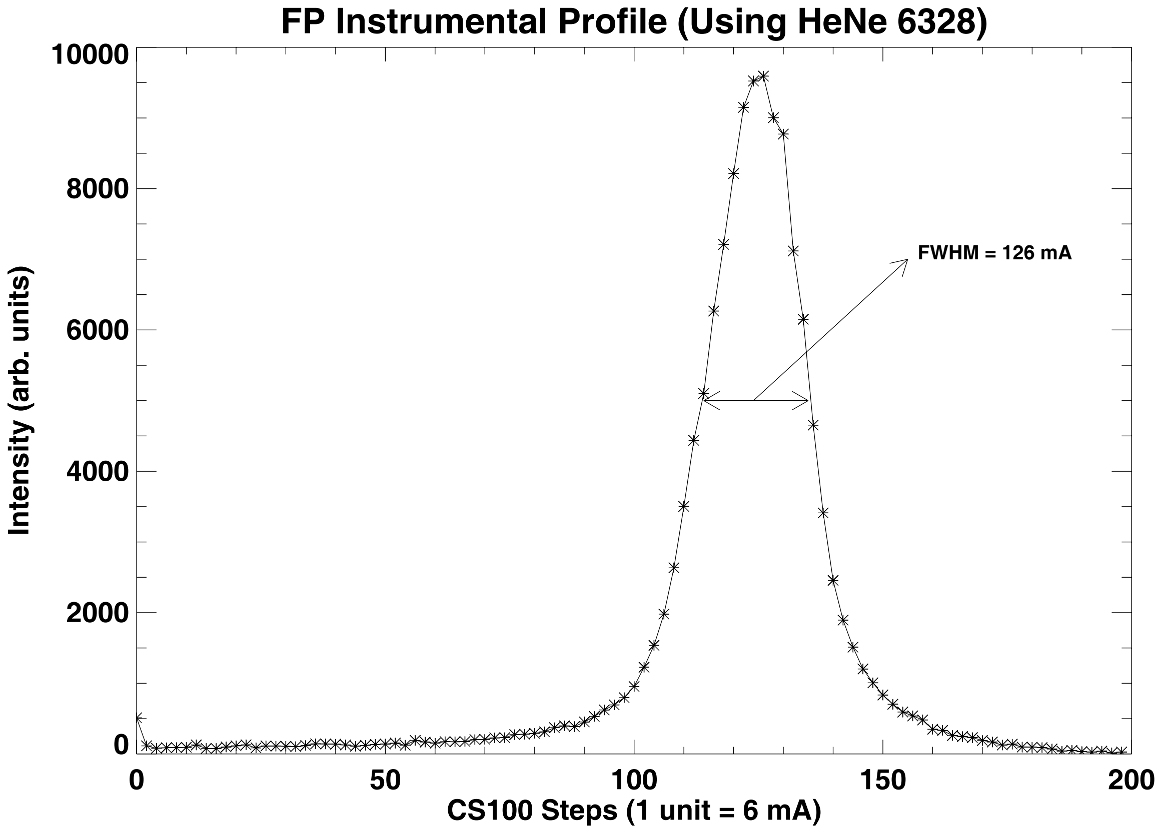

Figure 2.8: The instrumental profile of the air-gap etalon determined by the HeNe laser in the laboratory. The FWHM of the transmission profile corresponds to 125mÅ.

The camera is capable of reading full frames or sub-frames. There is also 1x1 to 8x63 on-chip binning. The detector has quantum efficiency (QE) of 40% at 400nm and a peak QE of 72% at 550nm. The camera has a Melles Griot 42 mm iris shutter, which allows to take exposures from 30 milliseconds to 10,400 milliseconds (in 10 milliseconds increment). The gain is set at 8 e^{-} per ADU (analog to digital conversion unit) and the nominal dark current value is 1 to 2 e^{-} pixel^{-1}second^{-1}. The camera comes with ActiveX control driver software. These drivers can be called from any windows based programming language to access the camera functions and data array. The camera driver is very useful for developing custom observing software. In fact, the camera driver has allowed us to develop a dedicated control software for SVM data acquisition. This software is built on a Microsoft^{TM} Visual Basic platform, which allows event driven programming. A Graphical User Interface(GUI) has been developed which allows user to run SVM operations with the click of a mouse. Further, a very new concept has been used in software design which allows the images to be directly displayed and analyzed on the GUI itself by embedding Interactive Data Language (IDL) ActiveX object in the interface. The software has been described in detail in chapter 3 of this thesis.

2.8 Solar Vector Magnetograph: Phase I

The Solar Vector Magnetograph was developed in two phases. In phase I the instrument was installed on the terrace of the USO office building. This setup was basically used: (i) to evaluate the performance of the mechanical components on a tracking system, (ii) to evaluate the performance of polarimeter and Fabry-Perot, and (iii) to test the control software in various observing modes and modify accordingly. The length of the SVM optical setup was about 1.6 metres. The individual modules were fixed onto movable base plates, which were then fixed on optical rail at the desired locations. The entire rail was mounted on a German Equatorial mount. The polar alignment of the mount was done using the drift method and was found to be accurate enough to track a sunspot within few arc-seconds (maximum drift of 5 arc-seconds for a period of 5 minutes). This duration is long compared to the time required to make one complete Stokes measurement. The entire system was housed on the rooftop of USO office building, a platform with sliding dome was developed indigenously to house the telescope (see figure 2.9). During the operation the dome was retracted back and the telescope was kept in the open. The first light images were obtained in March 2005. The first light polarization images of the sunspot taken in the blue wing of Fe I 6302.5 Åline is shown in figure 2.10. It was realized from the phase-I of SVM that some of the optical mounts had flexure, which changes slowly during the day as the telescope tracks the sun. Also, the software was modified to record various observing parameters in the FITS (Flexible Image Transfer System) header of data file. An on-line wavelength calibration system was incorporated in the software. The instrument was operational during March-May 2005 and the observations were taken with this setup. The data reduction and analysis was carried out using a software developed in-house. This software and the data analysis procedure is described in detail in Chapter 4. The vector magnetic field observations of active regions, obtained during phase-I of SVM, has been used along with SoHO Michelson Doppler Imager (MDI) (Scherrer et al 1996) dopplergrams to study the effect of magnetic field inclination on the acoustic power. The results from this study are presented and their implications discussed in chapter 5.

Figure 2.9: A view of the Solar Vector Magnetograph Phase-I setup on the terrace of USO main office building. The sliding dome is pushed backwards here and the SVM optics mounted on the old German Equatorial mount. The computer and control electronics is kept in the mobile platform to move in and out.

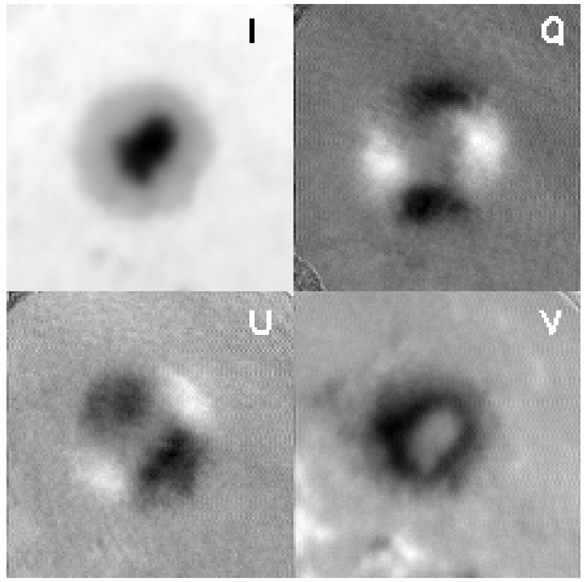

Figure 2.10: The first light observations obtained from the phase-I of SVM, represented here as Stokes I, Q, U and V images of a sunspot on the disk center. These images are obtained at 80 m$\AA$ away from the line center in the blue wing of Fe I 6302.5 line.

2.9 Solar Vector Magnetograph : Phase II

After the experience gained during the phase-I of SVM, the phase-II of SVM was initiated. During phase-II, the following new additions were made: (i) the mechanical mounts of the optical systems were re-designed and improved to reduce flexure and alignment problems, (ii) a new fully automated German-Equatorial mount was procured, (iii) an on-line calibration scheme for polarimeter was developed and implemented, and (iv) the magnetograph was adapted to the new German-Equatorial mount and the entire setup was shifted and installed at the island observing site of USO. The system was housed in a building which is cylindrical in shape and has a hemispherical dome which can be rotated manually. The dome has a slit which can be opened manually during the observations. The software for the observations was also modified to include many new features, which are described in chapter 3. The setting up of the instrument at island site and alignment of the new mount took lot of effort and time. The instrument setup in phase-II is shown in figure 2.11. The quality of data has improved in phase-II mainly due to the following reasons: (i) The open-loop (i.e., without guiding) tracking performance of the new mount was found to be very good. Typically, the drift is only 2 to 3 arc-seconds (i.e., 2-3 pixels) in 5 minutes, (ii) the present seeing conditions at the island site (when the lake is filled with water, which is presently the case) is proven to be better than when the lake is empty (Brajesh et al 2007), and (iii) the operation of the telescope inside the building protected by a dome prevents the telescope shake due to flow of winds present at the island site. The instrument in phase-II started operating in early 2007 (during February). The formal inauguration of the instrument was done on 20th February, 2007 by Dr. G. Madhavan Nair, Chairman, Indian Space Research Organization (ISRO).

During the current year which coincides with the solar minimum, there were very few active regions, most of which were non-flaring. The vector magnetic field observations of these regions were studied together with USO, high resolution H-α observations. The direction of the super-penumbral H-α filaments, which delineates the direction of transverse magnetic field in the chromosphere was compared with penumbral transverse magnetic field directions in photosphere, as observed with SVM. The preliminary results of this study are presented in chapter 6.

Figure 2.11: A view of the Solar Vector Magnetograph Phase-II setup at the island site of USO. The hemispherical dome on the cylindrical building can be manually rotated and opened. SVM optics is mounted on the newly procured German Equatorial mount.

Chapter 3

Software for Instrument Control

3.1 Summary

Any instrument that consists of many modules interfaced to a computer needs customized software for its operation. This is required because most of the times the individual components are bought from different vendors with their own controllers that follow their own standards and protocols. A detailed design and implementation of the software developed to run SVM observing sequence is described in this chapter. The philosophy behind this particular software design is the usage of Component Object Model (COM) technology of Microsoft Windows^{TM}. This gives an advantage of rapid software development, flexibility and portability. The control software is written in Visual Basic^{TM} software development environment. The user can interact with the instrument modules through a Graphical User Interface (GUI) and can program the sequence of magnetograph operations. The integration of Interactive Data Language (IDL) ActiveX components in the interface provides a powerful tool for online visualization, analysis and processing of images.

3.2 Control Software: Design Approach

The approach for fast development of magnetograph was to use off-the-shelf components. Thus, most of the components were bought directly from different vendors rather than developing them in-house. Although each vendor supplies some software drivers etc. with their hardware, the most common problem is to integrate all the sub-systems under one common platform using one programming language. Our choice of platform for control software was Microsoft Windows due to easy availability of device drivers for this Operating System (OS) and also because it does not limit the performance of the instrument in any way. Development of control software on free OS like Linux is attractive but non-availability of device drivers is the main drawback (Do-Young et al., 2002).

The sequence of magnetograph operations involve (i) setting the CCD exposure times, (ii) calibrating the Fabry-Perot (FP) filter before observations, (iii) setting the FP cavity tuning parameters like start wavelength, end wavelength and step-size, (iv) orienting the wave plate for each Stokes measurement, (v) record CCD images at various wavelengths as defined in (iii) above at each orientation of wave plate, and finally (vi) write the data-cube thus obtained onto the hard-disk in FITS format.

3.3 Hardware aspects of various components

3.3.1 Computer Hardware and Peripherals

The computer used is a Pentium III PC with 800MHz frequency processor. One of the desired features of SVM operation is to keep large-sized data-cubes (typical size ranges from 40 to 100 MB) in system RAM during wavelength scan and write them to system hard disk drive (HDD) while the wave plate orientation is being changed. This avoids the disk writing during data acquisition and uses idle PC time for writing while wave plates are moving. Thus more than the computing power of the PC we require a PC with large RAM size and fast HDD. For this purpose we use 512MB RAM and a fast SCSI HDD with 10,000 RPM. For backup of the data we use the optical media.

3.3.2 Fabry-Perot Controller

Piezo-scanned Fabry-Perot etalons using a closed-loop feedback system have been demonstrated using the technique of capacitance micrometry (Hicks et al, 1976). This technique removes the problem of the nonlinear response and hysteresis associated with piezoelectric transducers and allows precise control of both etalon gap and parallelism. The CS100 servo controller is interfaced to the PC using RS232 serial port. The company specified protocol is used for passing appropriate commands over serial cable for setting cavity spacing, response time, front-panel enable/disable and reading cavity spacing. The cavity spacing for SVM etalon is 433 μm and the cavity scan range is $\pm$ 3μm. The entire scan range is divided into 4096 digital units (i.e., 12 bits). The minimum wavelength scan achieved per digital unit is 6.5 m$\mathring{A}$. The cavity spacing is controlled by sending appropriate value of the Z (where Z ranges from 0 to 4096) in hexadecimal format to the input port of CS100 communications port.

3.3.3 Polarimeter Controller

The polarimeter consists of two multi-order quartz quarter-wave plates designed for 632.8nm. These wave plates are mounted on Nanorotator$^{(TM)}$ stages from Melles Griot. These stages provide fast and accurate positioning with positioning resolution of 1 arc-sec. The stages are equipped with stepper motors driven by proprietary Nanostep$^{(TM)}$ controllers with inbuilt microprocessor, which sends micro-stepping signals to motors. The controllers are provided with General Purpose Interface Bus (GPIB) interface. These controllers can be configured to drive linear as well as rotary stages. There are two controllers, one is called the master and other slave. Each controller can control upto two axes of motion. Each axis can be configured for rotary or linear motion by software. For faster response and pre-programmed moves one can write programs and embed them in the flash memory of these controllers. After feeding the company provided calibration data the backlash error is compensated and thereby improves the repeatability. The motion can follow a given profile for given acceleration, speed and deceleration. A PCI-GPIB card is used for controlling the Nanostep$^{(TM)}$ controllers. The positioning can be done using appropriate GPIB command sets provided by the vendor. The highly programmable and flexible command sets allows one to define the minimum speed, acceleration, maximum speed, resolution and velocity profiling of these rotating stages. Also, these are continuous 360-degree stages with a limit switch, which is used as reference position of the stages. The PCI-GPIB card is from Ms. National Instruments and uses NI488.2 device driver, which can be programmed using variety of programming languages.

3.3.4 CCD Controller

The CCD camera is from Ms Apogee Inc. (model AP6E). The ActiveX COM drivers that come with this camera are very useful. These drivers are easily callable under any windows programming language supporting Component Object Model (COM) interface and thus allows easy integration of the camera control in any application. Further, the data array is immediately returned via a pointer to the array memory. Using this pointer another program can quickly access the images from the memory. Using IDL programming language, which is capable of array processing, and "IDL-DrawXWidget" ActiveX object of IDL, it is possible to immediately process and store the data. We use this feature of IDL to access and store the images in form of FITS data-cubes using IDL astronomy library routines (available from NASA http://heasarc.nasa.gov/docs/fits.html). The Camera consists of a 1024x1024 pixel array with pixel size of 24 micron. The camera is interfaced to PC with a PCI card. The controller card does not have its own memory and directly passes incoming data using Direct Memory Access (DMA) to system RAM. The digitization is done with

14 bits. The camera is thermoelectric cooled with forced air. The cooler can go down to -20 °C. A TTL input to PC controller allows exposure start within 100ns of trigger for applications requiring precise synchronization of exposures to external events. The camera supports sub-frame readout.

3.4 Software Design

The design of software is mainly dictated by the following requirements.

(i) Initialization of each module,

(ii) Setting parameters of each module interactively,

(iii) online display of images from camera,

(iv) calibration programs for each module,

(v) programmable sequence of operation,

(vi) data visualization and pre-processing,

(v) storing the data in FITS format, and

(vi) storing instrument parameters in FITS header.

The development tool of choice was Visual Basic $^{(TM)}$ since it provided a rapid application development environment and suited well to our software/hardware interfaces. The development approach was modular and each module was separately tested before integration under single graphical user interface (GUI). These modules are described below.

3.4.1 CCD Control module

The module for controlling the CCD camera is designed as shown in figure 3.1. The CCD camera allows to read a portion of the chip. The region of interest is defined as follows. The starting coordinates on the CCD chip are specified in the text-boxes labelled as STARTX and STARTY in the GUI. The number of pixels to read in X and Y directions are then specified in the text-boxes labelled NUMX and NUMY.

Further, the exposure time of the CCD camera is selected by specifying the

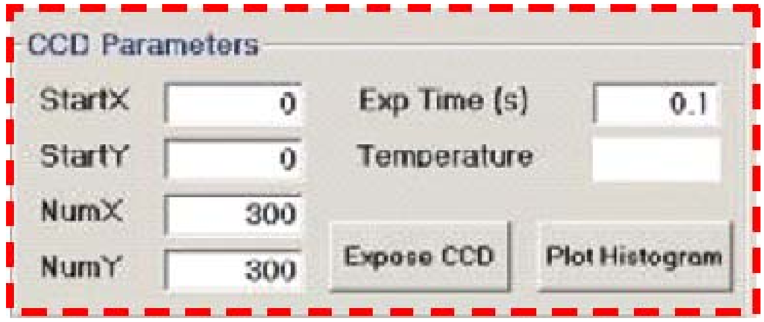

Figure 3.1: A closeup of the module meant for controlling CCD camera coordinates, exposure-time, intensity histogram and CCD chip temperature indicator are shown.

exposure time in text-box labelled EXP-TIME. A test exposure with the settings done above can be made by pressing the button labelled EXPOSE CCD. An image is then acquired and displayed on the GUI. In order to check the counts of exposed image one can plot a histogram of the image intensity on the GUI. To monitor the temperature of the CCD camera continuously and are displayed on the GUI in the CCD control section.

3.4.2 Polarimeter module

The polarimeter can be controlled by passing commands over GPIB bus to the Nanostep (TM) rotating stage controller. For passing commands one needs to access the device handle, which is then used for communicating with the device. This was easily done using proprietary NI488.2 (TM) Application Programming Interface (API) provided with the GPIB card. The polarimeter control was integrated in Visual Basic by incorporating definition modules for GPIB card available from National Instruments website (http://www.natinst.com/gpib/). The module showing the polarimeter interface is shown in figure 3.2.

The desired parameters can be read from the GUI and appropriate commands

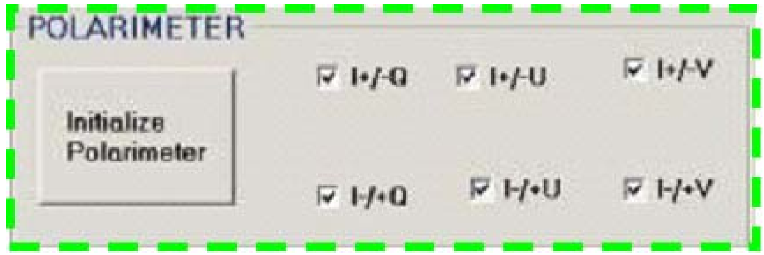

Figure 3.2: A closeup of the module in the GUI used for controlling the polarimeter. The initialization of rotary stages to home position is done by pressing INITIALIZE button. The orientation of the QWPs is set to reference angles automatically.

communicated to device via GPIB. The initialization of polarimeter rotary stages to zero set-point is done by pressing INITIALIZE button. We have hardwired the sequence of orientations of the waveplates for each Stokes parameter into the control program of the polarimeter, since these sequences are pre-defined. The user can select the kind of Stokes measurement that needs to be performed via a check-box. This involves initializing the rotary stage to a reference position and then going for subsequent orientations as per user selection. Finally, the stages return to initial position.

3.4.3 Fabry-Perot etalon CS100 control module

The software interface for communication with CS100 is shown in figure 3.3. The hardware interface provided with CS100 control is RS232 standard Serial port. The software support for this device is not very user friendly with no sample programs provided, and one has to write specific codes for port settings and for decimal to hexadecimal conversions. Also, the communication protocol is not very user friendly and can not be easily interpreted by reading the commands. Thus we developed the entire CS100 control by our GUI from very low-level communication protocols via RS232 serial communications interface. There are several ways in which one can perform serial communications, we chose to use MSCOMM component readily available under Visual Basic. By accessing its "methods()" and "properties()" one can perform all desired communication with the device.

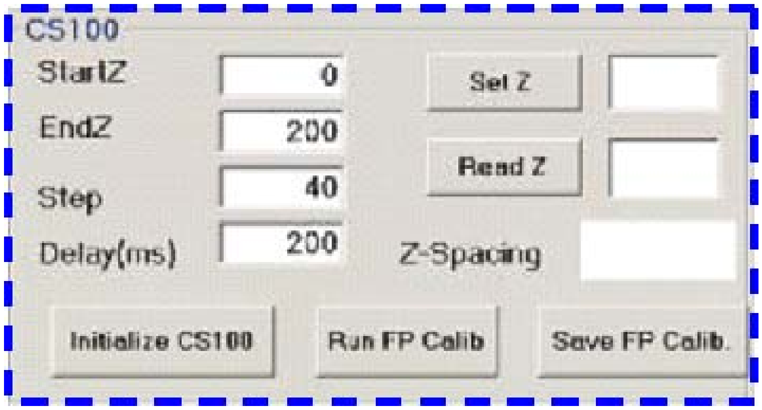

Figure 3.3: A closeup of the module meant for controlling CS100 controller for Fabry-Perot etalon is shown. The values of the cavity scan range are given in terms of 12 bit number. The start and end number are provided in the STARTZ and ENDZ boxes. The step size (STEPZ) for the scan is in multiples of 6.5 $m\AA$.

The cavity tuning range is adjusted in CS100 controller such that the entire cavity tuning range, which is $\pm 3\mu m$ corresponds to 4096 levels. The FP cavity is then tuned by sending appropriate hexadecimal values in 12bit range. Thus we have provided in GUI the start-step, end-step and step-size so number of scans is automatically calculated and a corresponding memory space is allocated for the data cube. Also, important are parameters like response time, reading cavity spacing and out-of-range indicator, which can be done using GUI. Due to possibility of drifts in the cavity spacing one needs to calibrate frequently the FP etalon and know the line center wavelength beforehand. This means one needs to have an online facility for taking images at user specified start-step, end-step and step-size and show the profile

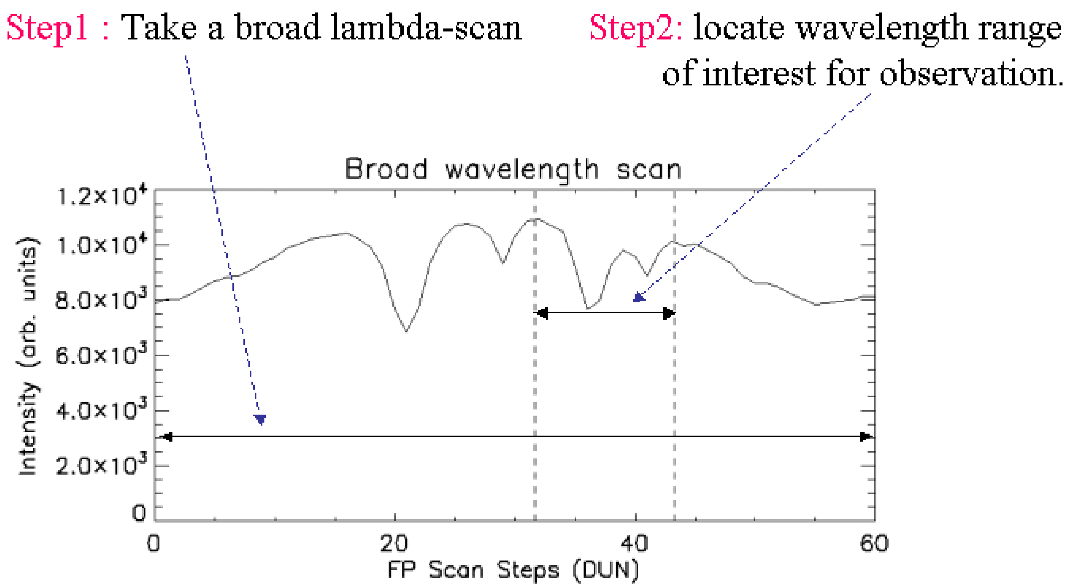

Figure 3.4: A schematic of Fabry-Perot calibration procedure. A broad FP scan is taken as a first step. The spectral line to be observed is then selected for further observation as a next step.

immediately. This is provided in the GUI as a separate module, which performs the scan on the selected solar region and shows the intensity profile, which is used to calibrate the line enter position. This is explained in figure3.4 . One can save this calibration data-cube in FITS format for later reference.

3.4.4 Analysis and Visualization System

A popular astronomy image processing software called IDL^{TM} (Interactive Data Language) is integrated in the application for online visualization and analysis of the images. This is implemented with the help of IDL ActiveX component called "IDLDrawX". This component consists of graphics display window, which is embedded, in the main form of the GUI. This component has very useful "properties()" and "methods()" with which one can exchange image data between IDL and Visual Basic via pointers and intrinsic IDL functions can be applied on the image array.

This makes on-line image processing very easy as one need not write the image processing code from the scratch. The graphics display window on the GUI is used for the image display and plotting via IDL. Also, one can write the image data to FITS (Flexible Image Transport System) format using NASA/IDL library function "write fits()". The data-cube can be created in IDL and images can be stacked one by one to the data-cube as they are read from the camera. Later this data-cube is written to hard disk in FITS format with all the observing settings written to FITS header. This avoids disk-writing time during wavelength scan thereby making scanning process faster and also memory allocation and management is done by IDL at high level.

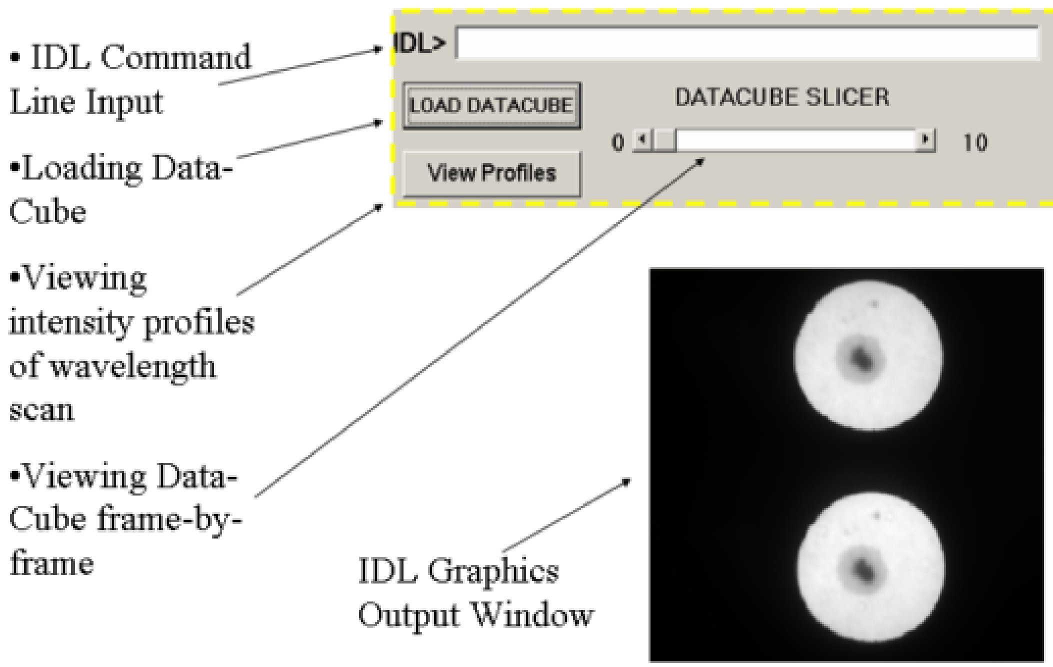

Figure 3.5: A closeup of the module meant for loading the datacube and visualizing the frames one by one by sliding the slider is shown.

The visualization of the data-cube like extracting wavelength profile at any spatial coordinate can be done from the same interface quickly through IDL plotting routines. This is needed for choosing the scanning parameters like start-step, end-step and step-size before performing spectral scan. This section of the software interface is shown in figure 3.5.

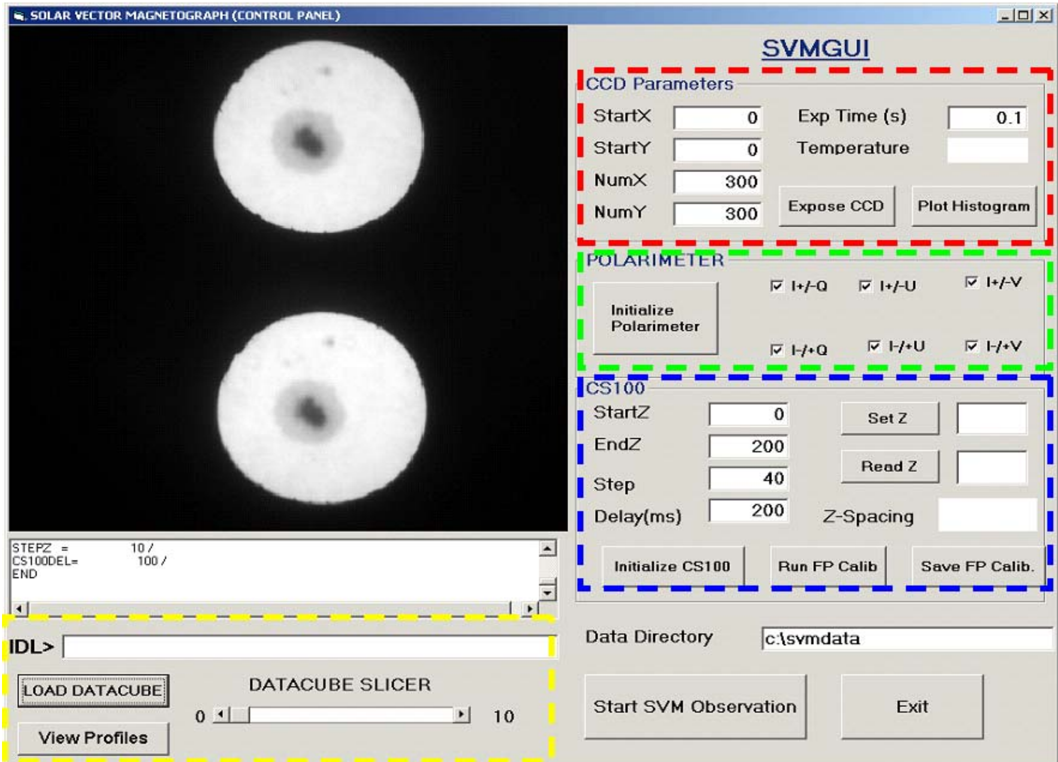

Figure 3.6: Snapshot of the integrated instrument control GUI showing different instrument control sections and IDL graphics display window (black panel) for image display

3.4.5 Control software enhancements during phase-II

During phase-II of SVM at island site, it was realised that the size of data that was required to be copied to optical media like Compact Disc was enormous and time consuming. The reason for the data-size to be large was that the area on the CCD camera chip that was readout included two beams (as shown in figure 3.5). The useful portion from the frame containing the active region, however, was smaller than the actual area readout. Earlier, this area was extracted from the larger frame (as shown in figure 3.5) during data reduction. In phase-II the control software was modified such that the observer can specify the area-of-interest (AOI) in both the beams in the recorded frame. This way the actual AOI is extracted from the data array, as soon as it is read-out from the camera into the memory, and stored onto the disk. This substantially reduced the amount of data generated and saved lot of backup time as well as the time for offline AOI extraction during data reduction. Further, the mean dark and bias frames that are taken during the observations can be applied on-the-fly to the incoming data-array from the camera. This saves lot of time that will otherwise be wasted during offline data reduction. Further, the calibration assembly for the polarimeter, which consists of a retarder plate mounted on a rotary stage can be inserted into the beam and rotated through the control software. The telescope mount is fully capable of computer control and has its own software which has lot of useful features. Since, the telescope control needs to be done only during the starting and end of the observing run, it is not integrated into the SVM control software. However, features like setting appropriate tracking rate for the Sun can be done from the SVM control software. The telescope also allows user to receive correction signals from the guider in form of TTL pulses. A webcam based guider has been implemented in SVM phase-II. The full-disk image of the sun is captured from the webcam, which is co-aligned with the main telescope. The webcam is read at a frame rate of 5 frames-per-second. The centroid is calculated for each image and compared with desired co-ordinates to estimate the drift of the telescope. The errors are then fed to the telescope control system (MKS4000) via parallel port. The four pins of parallel port are used for RA+, RA-, DEC+ and DEC- controls. By giving appropriate signals to the telescope control system the target can be kept in the field-of-view continuously for long duration (see Appendix-A). The preliminary version of the guider is developed, and in future a more refined version will be developed which will use cross-correlation of solar images to determine minute shifts and correct them to provide stable tracking.

3.5 Discussion and Conclusion

A snapshot of the entire control interface (GUI) is shown in figure 3.6. In this software design we have shown how the COM technology available in MS Windows platform can be used under Visual Basic for easy and fast system integration. An encouraging aspect of this philosophy of developing software by integrating COM components is the availability of COM components for different instrument modules from the manufacturers or third-party vendors. Also, for astronomers there is already an ASCOM (Astronomy Software Component Object Model) standard available, which is a set of technologies and drivers that form the basis for interoperability between ASCOM-based tools. The most current list of supported instruments can be found at http://ascomstandards.org/drivers.html. So, if one chooses ASCOMcompatible hard- wares for their instrument the control software or system integration becomes very fast and easy. Also, by adding COMcomponents of analysis packages like IDL to the instrument control software one can make their application very powerful.

Chapter 4

Data Reduction and Stokes Inversion

4.1 Summary

The reduction and analysis of the data from any instrument is carried out by performing a series of operations on the raw data. Essentially these operations are done to remove or compensate the imperfections in the instrument. For SVM these operations require procedures to do the following tasks: (i) restore the spatial correspondence of the spectral images in the data-cube, that is registration of images, (ii) restore the correct intensity of the recorded images, that is correct for dark, bias, gain non-uniformity of the detector and remove systematic patterns like fringes or ghost images, (iii) determine correct wavelength, that is, to calibrate the reference wavelength, and (iv) to restore the correct polarization intensities, that is, calibration of the measured Stokes parameters. Further, it is important to note that all of the aforementioned procedures have finite accuracy and the final data will always have certain amount of uncertainty, which one tries to minimize as much as possible by incorporating improved techniques in instrumentation, calibration and data reduction techniques. Another important requirement of data reduction is to have an access to the observing log, i.e, information on all relevant observing and calibration parameters. With the advent of Flexible Image Transport System (FITS) file format it is possible to keep entire observing log as a part of data file itself in the form of an extended header. Further, the spectro-polarimetric datasets are typically huge (in terms of memory) due to coverage in spatial, wavelength and temporal dimensions, i.e., I(x,y,λ,t). These datasets require lot of computational resources to process the data. It is, therefore, desirable to have a data reduction program which is user-friendly and takes less time in processing the data.

This reduced data contains measurement of Stokes parameters across the absorption line and needs to be interpreted in terms of the magnetic field vector. This interpretation requires knowledge of line formation in magnetized solar atmosphere. The solution to the polarized radiative transfer equation were formulated by Unno(1956), Stepanov(1960), and Rachkovsky(1972). Further, the choice of model atmosphere used for radiative transfer is also important. The inversion of the observed Stokes profiles under Milne-Eddington atmosphere with simplifying assumptions is the most popular method used for inferring the magnetic and thermodynamic parameters. The Milne Eddington model neglects depth dependence of physical parameters and assumes linear variation of source function with depth. For the spectro-polarimetric observations with filter based instruments of modest spectral resolution and limited wavelength sampling, the Milne-Eddington inversions give good results for magnetic field parameters while other physical parameters are poorly determined (Lites and Skumanich, 1984, Graham et al, 2002). These inversions depend on the number of spectral samples and the noise in the profiles (Lites and Skumanich, 1984).

With the development of solar adaptive optics system (Scharmer et al. 2000; Luhe von der et al. 2002; Rimelle et al. 2006) and tandem etalon filter system TESOS (Kentischer et al. 1998), filter based instruments are now comparable with the spectrograph based instruments in terms of high spectral and spatial resolution like Tenerife Infrared Polarimeter (TIP), La Palma, Spain. However, adaptive optics can correct for atmospheric distortions only in small fields-of-view called "isoplanatic patches". This problem shall be overcome by instruments operating in space, like the proposed Helioseismic and Magnetic Imager (HMI) instrument on-board Solar Dynamics Observatory (SDO) proposed for 2008, however due to telemetry problems they can perform very limited line sampling. The ground based instruments like SVM are free from telemetry issues and can study the evolution of magnetic field vector with full line sampling and faster cadence. The combined study of magnetic regions with space based observations will be of great value.

This chapter describes (i) the data format used to store the SVM observations and (ii) the data reduction and analysis procedures for reducing SVM data and a package for performing these operations , (iii) the inversion of observed Stokes profiles using Milne-Eddington model atmosphere with a software utility, which allows changing the guess model parameters and inferring magnetic field vector from SVM observations interactively, and (iv) a visualization package to display vector data, resolve 180° ambiguity using potential field, and perform geometric transformations.

4.2 SVM Observational Data-set

A typical observational run of SVM consists of the following sequences.

- (i) Spectral Calibration: In order to sample the spectral line properly the wavelength scanning parameters are determined by calibrating the Fabry-Perot. This is done by looking at the disk center of the sun and performing a wavelength scan over one complete free spectral range (FSR). This data-cube is then saved as a FITS file for later reference. The name of this file is generally given by the observer through an "inputbox" in the GUI as FP-CALXXXX.FITS, where XXXX is the time in HHMM format. These calibrations are repeated frequently and are useful to check any error due to the Fabry-Perot drifts.

- (ii) Dark and Bias: A mean dark and bias images are taken by averaging 20 frames each.

- (iii) Flat field observations: A burst of ten slightly de-focused images of the quiet sun are taken in continuum and are averaged to make a flat field. These images are taken as close to disk center as possible in order to avoid limb darkening. The telescope is shaken randomly to blur out any intensity patterns of solar origin. Flat-fields are obtained for each of the three orientations of the wave-plate to take care of beam wobble.

- (iv) Polarimetric Observations: The polarimetric images of the target region are observed by measuring the Stokes Q,U, and V parameters at each image position and as a function of wavelength. Due to the slow movement of polarimeter retarders we record each Stokes parameter sequentially. That is, first we fix the polarimeter position for a particular Stokes parameter and perform the wavelength scan and then move to next polarimeter position and repeat the scan.

- (v) Clear Observations: These observations are identical to polarimetric observations mentioned above but these are taken in quiet sun as close to disk center as possible and are slightly out of focus. These observations are useful for removing fringe patterns from the actual dataset, where fringe patter changes with each wavelength position.

4.2.1 Visualizing a Wavelength Data-cube

Before explaining more details about array processing and array data-cubes, here I briefly explain how a data-cube (or three dimensional data array) can be visualized. The data-cube obtained by performing a wavelength scan can be visualized as in the figure 4.1. The horizontal top-surface of the cube shows the image of the field-of-view (here a sunspot is selected for observation) at a particular wavelength. Actually, two images of the same FOV are obtained in same frame due to calcite in front of CCD camera. These two images are orthogonally polarized. Their sun gives the intensity and their difference gives the appropriate Stokes parameter. Similarly, other images of the same field-of-view are taken at adjacent wavelengths and are stacked one over the other. One wavelength data-cube is generated for each Stokes parameter, therefore one requires three wavelength data-cubes, for one complete set of Stokes vector observation. The wavelength dimension is along the vertical direction in the figure (the vertical surface of the cube looks like the image of a solar spectrum as taken by spectrographs with the spatial direction of the slit along X and Y axes respectively. The spectral line visible in this figure is Fe I 6302.5 along with the telluric line.

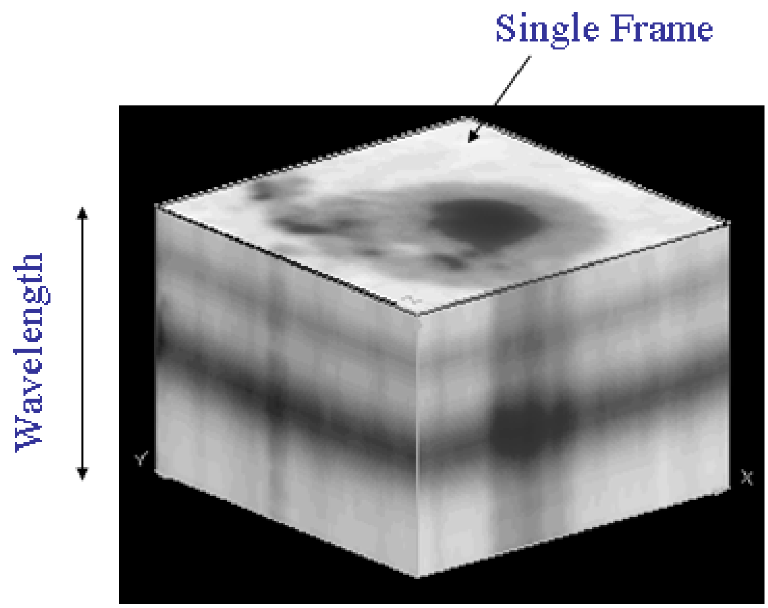

Figure 4.1: The data-cube obtained by performing a wavelength scan is shown in the adjoining figure. The horizontal top-surface of the cube shows the image of the field-of-view at a particular wavelength. Similarly, other images taken at adjacent wavelengths are stacked one over the other. The wavelength dimension looks like the image of a solar spectral absorption line as taken by spectrographs.

4.2.2 SVM FITS File Format and Extended Header Description

The section below describes the kind of data acquired by the instrument, its format, header specifications and the steps involved in step-by-step reduction procedures. The data format for the SVM is chosen to be Flexible Image Transport System (FITS) standard. This is a standard developed by NASA USA. More details on the FITS standard and utilities can be found from the website

"http://heasarc.nasa.gov/docs/heasarc/fits.html".

The format allows one to write extended headers in addition to standard headers, to allow maintaining a log of all observing parameters. This self informative headers explain every detail about the data to the user and enables sharing of data within the community. The observing parameters in case of SVM are briefly described as follows:

The minimal header generated in FITS file format for any file is given below.

- SIMPLE : This contains the date, time and application used for creating FITS file
- BITPIX : This tells about the Analogue to Digital (A/D) digitization per pixel (In our case this is 14 bits).
- NAXIS : Number of dimensions of the data set (In our case this is 3).
- NAXIS1 : Number of pixels in X-dimension.
- NAXIS2 : Number of pixels in Y-dimension.
- NAXIS3 : Number of points in wavelength scan (Z-scan).
- DATE : Date of file creation in (CCYY-MM-DD) format.

4.2.3 CCD camera parameters incorporated in the FITS header

The region of interest is that area of the CCD chip which, we are interested to read. The CCD chip size is 1024×1024 pixels. Following are the entries in FITS header relevant for knowing region-of-interest.

- STARTX : X-Pixel from which to start reading
- STARTY : Y-Pixel from which to start reading
- NUMX : Number of pixel to read in X-direction
- NUMY : Number of pixel to read in Y-direction
- CCDTEMP: Present temperature of the CCD chip
- CCDTEMPS: Desired temperature of the CCD Chip
- CCDCOOLER MODE: Mode of cooling AUTO/MANUAL
- EXPOSURE: Exposure time of the CCD camera shutter in seconds.

4.2.4 Fabry-Perot etalon controller (CS100) parameters

The Fabry Perot etalon as described in previous chapter, is mounted on three piezo crystal stacks and the cavity spacing is changed by applying voltages to the piezo. The voltage to be given to piezos can be given in the range 0 to 4096, i.e., 12 bit number. This is indicated as Z-number. Following are the entries in FITS header relevant for knowing CS100 wavelength scanning details.

- STARTZ : Start Z value of cavity spacing
- ENDZ : End Z value of cavity spacing
- STEPZ : Incremental z-value while performing wavelength scan

- CS100DEL : The delay in milliseconds before applying next z-value in a scan.

4.3 Data Reduction

This section describes the data reduction procedures performed on SVM observations in order to derive the Stokes spectra. Most of these operations can be performed via a graphical user interface as described in the following section.

4.3.1 Dark, Bias removal

The images of dark current and electronic bias are taken frequently ,i.e., every half and hour or so during the observations.These images are made by taking about twenty individual dark and bias frames and averaging them. The exposure time of the dark is same as the the data image. If exposure time of data image is changed due to sky conditions the dark observation is repeated with changed exposure time. There is a provision in the SVM control software to apply on-line dark and bias corrections to the incoming images from the camera. The mean dark and bias images are saved as FITS files for later reference, if required. The mean dark and bias are also used in correcting the flat-field and the spectral calibration images during data reduction.

4.3.2 Flat fielding

The flat-field image is taken by pointing the telescope to the disk center of the sun and averaging several frames (about 10), taken in continuum, while the telescope is shaken randomly with the joystick. This flat-field is repeated at each polarimeter orientation to take care of beam wobble. The flat-field sequences are taken from the control software of SVM, while the number of frames to be averaged and the continuum window can be changed from the user interface. Once the flat-field sequence is taken, the control software can be programmed to apply flat-field corrections on-line to the incoming data from the camera. The flat fielding of the frames of the data-cube removes the dust-marks (see figure 4.2), corrects for gain inhomogeneities of the detector and the overall system transmission i.e., vignetting. The flat-field information is also used to balance the intensities of the two beams, which results due to different optical paths.

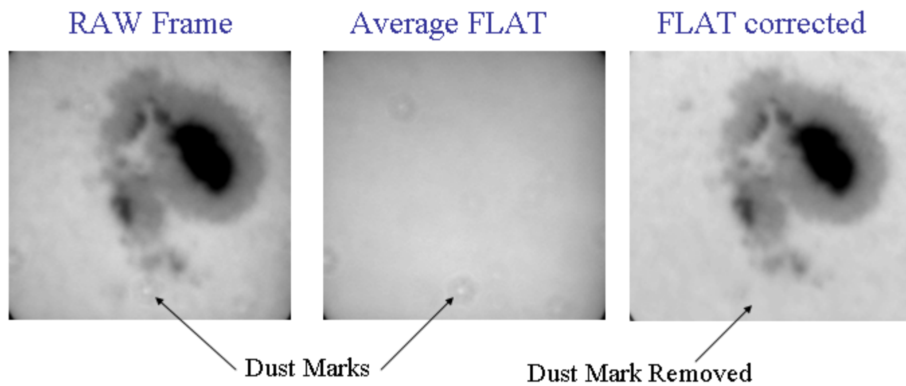

Figure 4.2: An example of flat-fielding procedure of the data frames using flat-field frame. The flat fielding removes the dust-marks, corrects for gain inhomogeneities of the detector and the overall system transmission.

4.3.3 Image Registration

The image motion due to atmospheric seeing and the telescope tracking errors are inevitable. These errors, while performing the wavelength scan, lead to spatio-spectral cross-talks. In order to correct these errors we need to register the images spatially. This registration needs to be performed within a single data-cube as well as between data-cubes. The three data-cubes (Stokes Q, U and V) are illustrated in figure 4.3. The first step is to register the images in each data-cube, taking the first image in that cube as the reference image. In second step the three data-cubes are aligned to each other. Thus all three datasets are spatially registered. The registration is done using the feature in the image like a sunspot or a pore. The registration is done with sub-pixel accuracy by interpolation in the Fourier domain

(Sridharan, 2001).

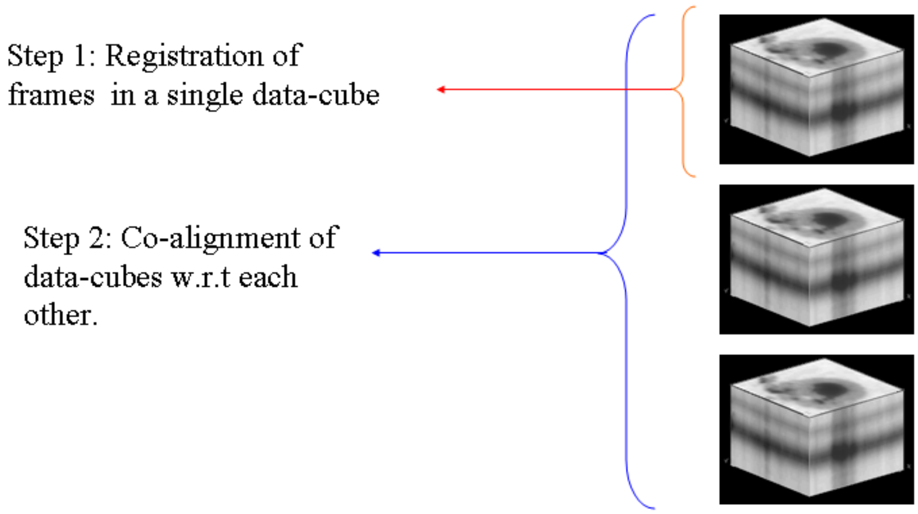

Figure 4.3: The three data-cubes (Stokes Q, U and V) are illustrated in this figure. The first step is to register the images in each data-cube, taking the first image in that cube as the reference image. In second step the three data-cubes are aligned to each other. Thus all three datasets are spatially registered.

4.3.4 Co-aligning the dual beams

The dual-beam optical setup was found to be the best solution to counter seeing-induced spurious signals in the polarization data (Lites et al. 1987, Semel 1987). The so called "beam exchange" technique, in which the two beams are swapped during observations, not only greatly reduces seeing-induced polarization signals but also makes best use of the photons available for the polarimetry (Semel 1993). The differential aberrations in the two optical paths are also greatly reduced by this technique. In order to merge the data from the two beams, it is required to co-align the images as accurately as possible. Again, this co-alignment is done using the feature in the image like a sunspot or a pore. The registration is done with sub-pixel accuracy by interpolation in the Fourier domain (Sridharan, 2001).

4.3.5 Removal of Fringes

The reflections between the surfaces of SVM optical components produces weak fringes in the data. These fringes are complicated because they are a function of wavelength and hence, a single flat field image is not sufficient to take care of fringes. Also, the removal of fringes by filtering in Fourier domain introduces artifacts as the spatial frequency of fringes is similar to that of solar features. However, these are repeatable (i.e., time independent) and do not occur randomly. In order to remove the fringes from the images in the data-cube we take a "clean" data-cube. The "clean" data-cube is taken with identical parameters as the "real" data-cube containing solar target region, but in a quiet region close to disk center. At each wavelength position in the data-cube

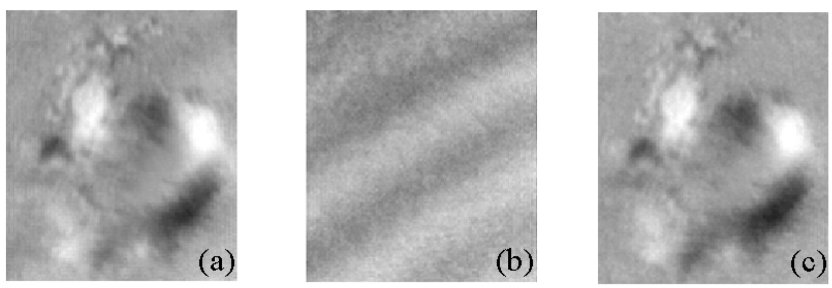

Figure 4.4: An example of fringe removal: (a) Stokes-U image of a sunspot obtained without fringe-removal, (b) a "clear" Stokes-U image at same wavelength as the sunspot, since there is no sunspot the contrast of fringes appears higher, and (c) the Stokes-U image after fringe removal as described in the text.

about six images are averaged by moving the telescope randomly to smooth out solar disk. The resulting "clear" data-cube, which contains the spectral line and the changing fringe pattern identical to the one in "real" data-cube. The next step is to remove the spectral line variation from the data-cube and leave alone the fringes.

This is not straightforward since the Fabry-Perot is in collimated beam there is a wavelength variation with field-of-view. In order to extract only the fringes in the data-cube, a parabolic surface is fitted to the frames and the frames are divided by the fit. This removes the spectral intensity variation across the field and leaves only the fringe pattern. This cube with only the fringe pattern is then used to remove fringes from the data like the usual flat-fielding procedure. The "clear" data cube used above is already corrected for dark, bias and continuum flat-field. As an example, fig 4.4 shows (a) a Stokes-U image of a sunspot obtained without correcting for fringes, (b) a "clear" Stokes U image at same wavelength as the sunspot, and (c) the Stokes-U image of the sunspot after fringe-removal.

4.3.6 Polarization calibration

The observed Stokes I,Q,U,V intensities at each wavelength position are corrected for polarimeter response. This is done by multiplying the observed Stokes vector by the inverse of experimentally determined Mueller matrix of the polarimeter (Chapter 2). The two beams from the calcite analyzer can be exchanged by changing the orientations of wave-plates of the polarimeter, i.e., $(I \pm S)$ positions are interchanged and they become $(I \mp S)$. The polarimeter response matrix is deduced separately for each scheme and applied to the corresponding observations. The two datasets are corrected and are merged to average the two signals to improve signal-to-noise ratio of the profiles. These profiles are then ready for Stokes inversion in order to deduce magnetic field parameters.

4.4 Stokes Inversion of the observed profiles

In order to infer the physical parameters from the observations, one assumes a model (i.e., set of assumptions and hypotheses) of the source atmosphere and tries to obtain the parameters of the model by reproducing the observations as closely as possible. These inferred parameters are therefore indirect observables. In practice the solar

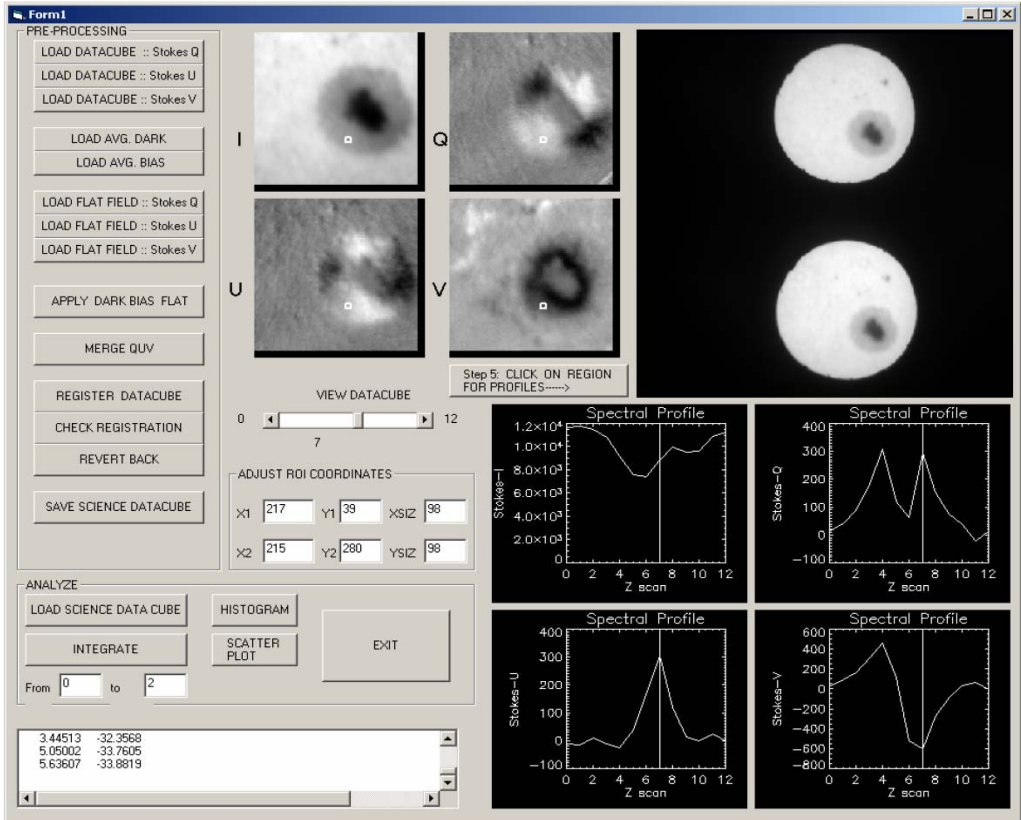

Figure 4.5: Snapshot of the data reduction tool, used to carry out the operations mentioned in the text. The IDL graphics display window is embedded for image display.

atmosphere may deviate from the idealized model assumptions and therefore the inversion results should be treated as an approximation to the actual physical conditions present in the real atmosphere. The results obtained by inversions may differ from model to model and therefore one considers which model is most plausible for a particular solar observation like sunspot, quiet sun, plage network etc.

4.4.1 Polarized Radiative Transfer Formulation

The quantitative interpretation of the observed stokes spectra is done by using a theoretical formulation of polarized radiative transfer equation. These equations determine how the profiles of Stokes vector are formed in the solar atmosphere permeated by magnetic field. These equations were first derived by Unno(1956), Stepanov(1960), and Rachkovsky(1972). The equation (from Stenflo 1994;2002) is represented as

$$\frac{d\vec{I_\nu}}{d\tau_c} = (\vec{\eta} + \vec{E})\ \vec{I_\nu} - \vec{S_\nu}$$

where $\vec{I_\nu}$ is the Stokes vector at frequency ν, τ_c is the continuum optical depth, defined by

$$d\tau_c \ = -\kappa_c\ ds$$

κ_c is the continuum opacity, $\vec{S_\nu}$ is the source function vector, which will be specified later, $\vec{E}$ is the 4 × 4 unity matrix, and $\vec{\eta}$ is the line absorption matrix, given by

$$\vec{\eta} = \begin{pmatrix} \eta_I & \eta_Q & \eta_U & \eta_V \\ \eta_Q & \eta_I & \rho_V & -\rho_U \\ \eta_U & -\rho_V & \eta_I & \rho_Q \\ \eta_V & \rho_U & -\rho_Q & \eta_I \end{pmatrix}$$

For normal Zeeman triplet

$$\eta_{I,Q,U,V} = \eta_0 H_{I,Q,U,V},$$

$$\rho_{Q,U,V} = 2\eta_0 F_{Q,U,V}$$

Here

$$\eta_0 = \kappa_0/\kappa_c,$$

where $\kappa_0 H(a,0)$ is the line absorption coefficient at the center of the line. The Voigt function $H(a,v)$ is defined below. First we define $H_{I,Q,U,V}$ by

$$H_I = H_\Delta sin^2\gamma + \frac{1}{2}(H_+ + H_-),$$

$$H_Q = H_\Delta sin^2\gamma\ cos2\chi,$$

$$H_U = H_\Delta sin^2\gamma\ sin2\chi,$$

$$H_V = \frac{1}{2}(H_+ - H_-)\ cos\gamma,$$

with

$$H_q = H(a, v - qv_H), \quad q = 0, \pm 1,$$

$$H_\Delta = \frac{1}{2}[H_0 - \frac{1}{2}(H_+ + H_-)].$$

The corresponding expressions for $F_{I,Q,U,V}$ are obtained by simply replacing H by F.

The Voigt function $H(a, v)$ is given by

$$H(a, v) = \frac{a}{\pi}\int_{-\infty}^{+\infty} \frac{e^{-y^2}dy}{(v-y)^2 + a^2},$$

which when integrated over v has an area $\sqrt{\pi}$ (so defined to make H(0,0)=1).

The line dispersion function $F(a, v)$ is given by

$$F(a, v) = \frac{1}{2\pi}\int_{-\infty}^{+\infty} \frac{(v-y)e^{-y^2}dy}{(v-y)^2 + a^2},$$

Further

$$v = (\nu_0 - \nu)/\Delta\nu_D,$$

$$q\ v_H = \Delta\nu_H/\Delta\nu_D,$$

while the damping parameter

$$a = \gamma/(4\pi\Delta\nu_D).$$

Here ν_0 is the central frequency and $\Delta\nu_D$ is the Doppler width.

The source function, under the assumption of Local Thermodynamic Equilibrium (LTE) is given as S_ν=B_ν (the Planck function). The analytic solutions of the polarized radiative transfer can be obtained under simplified model atmosphere. The first simplifying assumption that is made is that absorption matrix η is depth independent, which implies that the magnetic field is assumed to be homogeneous, and that the strength η_0 and shapes of the absorption-dispersion profiles are independent of depth. Another, assumption is that the source function vector S_ν, depends linearly on optical depth. This idealization is called Milne-Eddington approximation.

The solution for the emergent Stokes vector in units of the intensity of the local continuum was first derived by Unno (1956), without magneto-optical effects (anomalous dispersion), and later by Rachkovsky (1972) when magneto-optical effects were fully accounted for:

$$I/I_c = 1 + \beta + \beta(\eta_I + 1)[(\eta_I + 1)^2 + d]/\Delta$$

$$Q/I_c = -\beta[(\eta_I + 1)^2\eta_Q + (\eta_I + 1)(\rho_U\eta_V - \rho_V\eta_U) + s\rho_Q]\Delta$$

$$U/I_c = -\beta[(\eta_I + 1)^2\eta_U + (\eta_I + 1)(\rho_V\eta_Q - \rho_Q\eta_V) + s\rho_U]\Delta$$

$$V/I_c = -\beta[(\eta_I + 1)^2\eta_V + (\eta_I + 1)(\rho_Q\eta_U - \rho_U\eta_Q) + s\rho_V]\Delta$$

where

$$\Delta = (\eta_I + 1)^2[(\eta_I + 1)^2 - a + d]s^2$$

$$a = \eta_Q^2 + \eta_U^2 + \eta_V^2$$

$$s = \eta_Q\rho_Q + \eta_U\rho_U + \eta_V\rho_V$$

a represents absorption, d dispersion effects, while s is a kind of "scalar-product" between absorption and dispersion. Δ is common denominator of all the expressions .

4.4.2 Stokes Inversion

The forward calculation of emergent Stokes profiles from a given model atmosphere is simple, but the inverse problem of getting the model parameters from observed profiles is a difficult one. However, the inverse problem can be solved by linearization, like a least-squares fitting procedure. Let $y_i, i = 1, 2, 3, .., n$ be the observables with uncertainties σ_i, and let Y_i be the corresponding fits computed from the model. The goodness of the fit is judged by

$$\chi^2 = \frac{1}{n - m}\Sigma_{i=1}^{n}\frac{1}{\sigma^2}(y_i - Y_i)^2.$$

$n - m$ is the degrees of freedom of the problem. The problem is then to find the set of model parameters for which χ^2 reaches global minimum. Let the free parameters of the model be $a_k, k = 1, 2, ..., m$. Let us represent set of free parameters as components of vector $\vec{a}$). Then χ^2 as a function of $\vec{a}$ is represented by a surface in m-dimensional parameter space. We need to find the minimum value of χ^2on this surface. χ^2 hits local minimum when

$$\frac{\partial \chi^2}{\partial a_k} = 0$$

for all k. One can constrain the range of a_k by realistic values. The minimum of χ^2 is determined iteratively by starting with "guess" value $\vec{a_0}$. The $\vec{a_0}$ is perturbed by $\delta\vec{a}$ and a new improved minimum is searched. The new improved value for the location of the minimum $\vec{a_1} = \vec{a_0} + \delta\vec{a}$, serves as the starting point of new iteration. The iterations continue till no further minimum is reached.

4.4.3 Stokes inversion of SVM data

We have used MELANIE inversion code (Socas Navarro, 2001) for inverting the SVM observations. This code has been kindly provided by High Altitude Observatory (HAO), Boulder, Colorado under their Community Inversion Codes (CIC) project. This code fits Stokes profiles emergent from the solar atmosphere under the assumptions of Milne-Eddington atmosphere. The code tries to find the model atmosphere that provides the best least-squares fit to the profiles of an arbitrary number of simultaneously-observed spectral lines. The inversion code uses LORIEN engine (the LOvely Reusable Inversion ENgine), which combines the Singular Value Decomposition (SVD) technique with the Levenberg-Marquardt minimization method to solve inverse problems (Press et al. 1992). The underlying assumptions are:

- For all the lines considered, the opacity, Doppler width, velocity, and damping parameter are constant with height. The various line opacities may differ by a constant factor.

- The source function varies linearly with optical depth (at a reference wavelength) and is the same for all the lines.
- No sub-pixel magnetic structure is considered in the horizontal direction, although the magnetic atmosphere may coexist with a non-magnetic component.
- The observed Stokes profiles are induced by the Zeeman effect in transitions where L-S coupling is a valid approximation.

4.4.4 A toolkit for Milne-Eddington inversions

The MELANIE code has an input file which tells the mode of operation, i.e. synthesis mode or inversion mode. The synthesis mode generates synthetic line profiles for given input model parameters. The inversion mode inverts the observed profiles. The code needs wavelength parameters like start, end and step-size of wavelength profiles. Apart from this the code needs to know the spectral line parameters (Lande g-factor, upper and lower level quantum numbers). Also the model parameters for the model can be changed interactively. These parameters are namely : Magnetic field strength (in Gauss), inclination angle away from the line of sight (degrees), azimuth angle (degrees), line strength (a dimensionless parameter, also known as η in the literature), Doppler width (in mÅ), damping parameter (dimensionless), line-of-sight velocity (in km/s, positive values correspond to redshifts), source function at $\tau = 0$ (in units of intensity), source function gradient with τ (units of intensity), macroturbulence (km/s) and fraction of stray light (between 0 and 1, this parameter may be interpreted as the filling factor of the non-magnetic component).

With these inputs the code runs in either of the modes, i.e, synthesis or inversion. The description of the above mentioned parameters is given in separate files whose names are mentioned in the input files. Also, the profiles are needed to be fed in form of formatted text files containing columns for wavelength, Stokes I, Q, U, V normalized by continuum intensity. Normally, it is very time consuming for user to change the inversion parameters i.e., editing each of the files every time inversion is run for a dataset. Also, user often does not want to invert entire map but in few locations of interest over the active region or small region in the map. These features are not built into the code intrinsically. As a requirement to expedite the inversion process I have developed a graphical user interface around this code which allows interactive use of the code on the data. The design of the software is very general and can adapt to any data format and inversion code. For, example the data-cubes from either spectrograph based instruments or filter based instruments can be converted to desired format with little effort. Once the input data is in required format, the inversions can be performed straightaway. Another feature of the interface is the adaptability to any inversion code, for example the UNNOFIT code and the SIR code have been adapted to the interface successfully. The geometric operations on the data-cube, i.e., reversing dimensions of the data-cube like flipping vertical or horizontal axis can be performed from the interface. Further, the inversion of one point or a region-of-interest or entire map can be done from the interface. The output of inversion can be checked by plotting the fits over observed profiles. The outcome of the inversion of the entire maps can be displayed and saved into a file with all the inversion parameters used for the purpose. Also, the data-cube can be visualized inside the interface by a slider. The acronym given to the interface is Solar User-friendly Milne-Eddington Inversion Toolkit (SUMIT). A snapshot of the interface is shown in figure 4.6. The interface is however developed for Windows^{TM} operating systems and requires IDL installation.

4.5 Visualization package for SVM vector data

Further, in order to visualize and derive other physical parameters from the vector magnetograms I have developed a interactive display tool. The inverted magnetic field vector field data (saved into a file) can be loaded and be displayed in standard format followed by Hagyard (1984). In this format the line-of-sight (LOS) magnetic field is represented by contours, with different colors for positive and negative LOS field. The potential transverse field can be calculated using observed LOS field and used for resolving the 180° ambiguity. The observed and measured transverse field

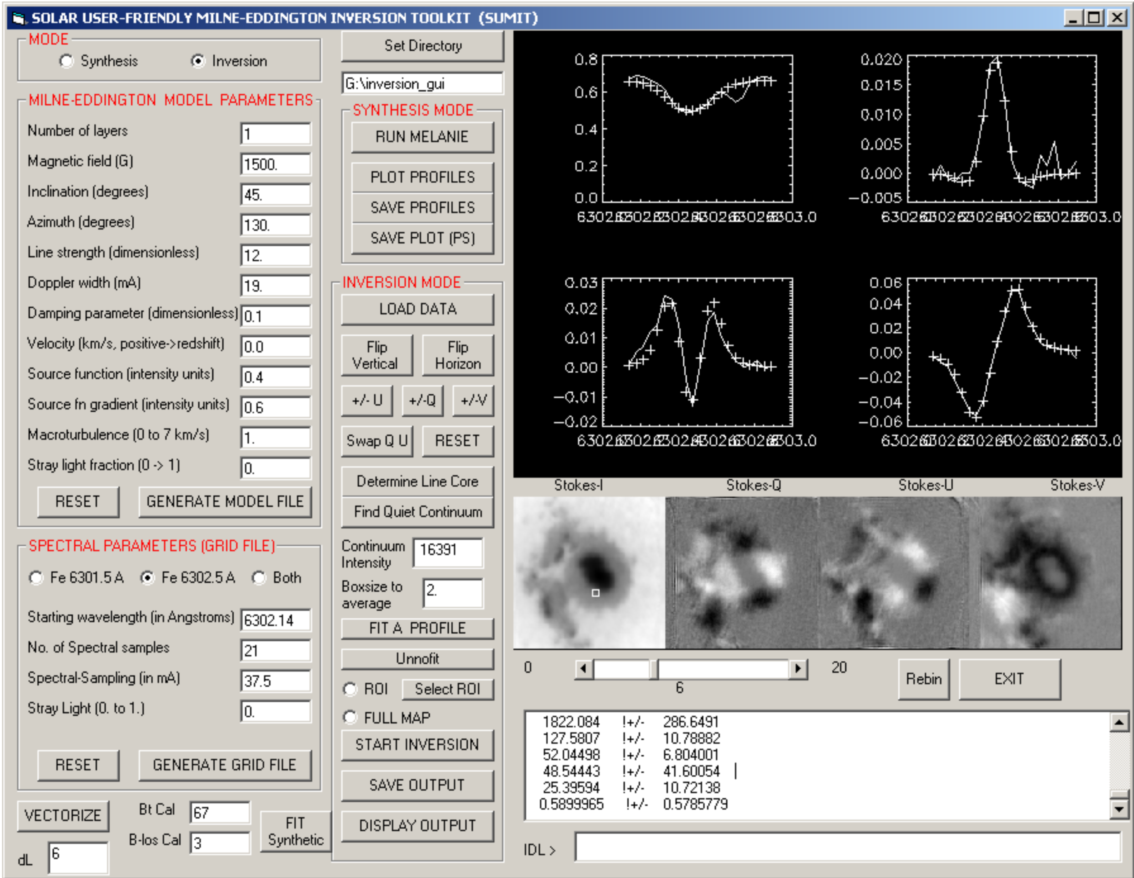

Figure 4.6: Snapshot of the GUI for performing inversion of Stokes profiles. The interface is developed around MELANIE code and can be used for line synthesis as well as inversion. The model parameters and wavelength scan parameters can be updated from the interface.

directions are compared and that direction of the observed field which makes acute angle with the potential field direction is taken as correct orientation of the field. This method is called "acute angle method" in literature and works for most part of the magnetic regions. In places where this angle is close to 90° there is problem in resolving the ambiguity, in such cases clue from orientation of observed H-α fibrils must be taken. Further, Venkatakrishnan et al. (1988) found that the shear angle (i.e., the difference between potential and observed azimuth angles) and the apparent length of neutral line in active regions located away from disk center suffers from projection effects. Thus, in order to transform vectors and field maps to heliographic coordinates algorithms developed by Hagyard (1987) and Venkatakrishnan et al (1988) are implemented. These algorithms require calculation of disk center L_0, B_0 and P angle for the date and time of observation, as well as the heliographic coordinates of the center of active region field-of-view i.e., $L_c \& B_c$. In order to calculate these values the programs are implemented in the interface itself. These programs are developed using formulae given in Duffet & Smith (1979). Further, for calculating $L_c \& B_c$ a full disk image can be loaded for the corresponding SVM observation and the coordinates can be determined by clicking at the appropriate active region. Since, the corresponding full-disk magnetogram is available from NSO/GONG ftp-site *ftp.nso.gong.edu/pub/dsds/fd/* (in Udaipur folder). These can be accessed by a button in the interface itself.

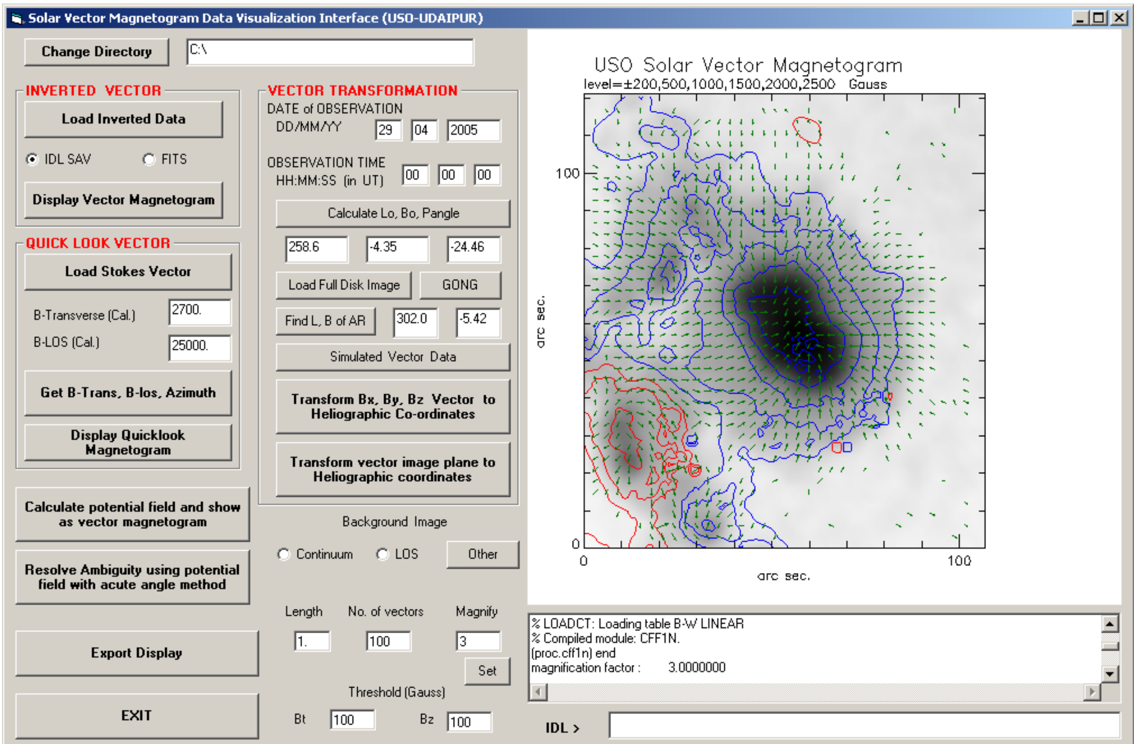

Figure 4.7: A snapshot of the interface for performing visualization, disambiguation and heliographic transformation of SVM vector magnetograms.

Chapter 5

Acoustic wave interaction with inclined magnetic fields

5.1 Introduction

The power spectrum of solar p-mode oscillations peaks around 5 minute period. The amplitude of these oscillations decreases in regions of strong magnetic fields. In fact, observations show that amplitude of oscillations decreases in low frequency (less than acoustic cut-off frequency) and increase in high frequency with increasing line-of-sight (LOS) magnetic field (Braun et al. 1987,1988; Venkatakrishnan et al 2002), with a transition at about 5 mHz (close to cut-off frequency). The high frequency power is also seen to be enhanced in sunspots. Also, the incoming acoustic power was seen to be greater than outgoing power (Braun et al. 1990), which implies absorption of acoustic energy by magnetic structures. The energy of acoustic p-modes is absorbed by about 50% in the regions of magnetic field concentrations like sunspots (Braun et al. 1992). The mechanism responsible for this absorption is, however, not clearly identified.

Two theories are proposed:

(i) Resonant Absorption (Dissipative Mechanism): Absorbed energy may be converted into heat within the sunspot by dissipative (irreversible) processes in a thin resonance layer. This process, known as resonant absorption has been studied well in coronal loops (Ionson 1982; Hollweg 1984; Davila 1987). Essentially MHD waves within a sunspot tube excite resistive modes at local Alfven resonance. At this point strong dissipation of internal MHD waves in a sunspot flux tube is possible, resulting in net loss of energy.

(ii) Mode Conversion (Non-Dissipative Mechanism): Incoming sound wave shakes the magnetic field of sunspot and energy (which was originally in sound waves) is transferred through mode conversion into magnetic wavemodes propagating more or less parallel to the magnetic field of sunspot flux tube. If these waves can leak from the system say upward through chromosphere (Bart De Pontieu, B. 2004), or downward through the base of the sunspot, one could explain the observed absorption by a completely non-dissipative process involving mode conversion in the field of the sunspot.

These process are not mutually exclusive, both may be present at the same time.

In this chapter an observational study of p-mode absorption by magnetic fields of a large sunspot is presented. The dependence of p-mode power absorption with magnetic field strength as well as inclination is carried out. It is found that in the strong field regions the amplitude of p-modes increases with increasing inclination angle. Further, the distribution of high and low frequency power over umbral, penumbral and umbral-penumbral boundary is studied. Our results agree with the finding that the power is reduced in middle penumbra as compared to inner and external penumbra (Marco et al. 1996).

5.2 Observational Data

The target region for the present study was NOAA AR No. 10756. This was a large sunspot covering about 690 millionth of entire solar surface. The region consisted of an unipolar sunspot and surrounding plage with no following sunspot. The sunspot appeared on 25th April 2005 and disappeared to the far-side of the sun on 6th

May 2005. The pixel scale of MDI (2arc-sec per pixel) offers only few (5-10) points for typical sunspots of size of 10-20 arc-sec for studying the spatial distribution of acoustic power in relation to sunspot structure. Large sunspots with diameter of 70-80 arc-sec have the advantage since they allow large sample points for statistics. There was no major flare event recorded for this region. The sunspot did not evolve much and remained simple and isolated. The right-half of the sunspot was symmetric as compared to left-half. Calibrated full disk MDI dopplergrams with one minute cadence and spanning from 17:59 UT to 01:58 UT, 29th April 2005 with intermittent missing frames were used as time series for further analysis. A region of 128x128 pixels containing the sunspot is extracted from full disk (1024x1024 pixels) image. The missing frames are replaced with the mean of temporally adjacent frames. The time varying component of the measured velocity signal is used for constructing the power spectrum at each pixel.

The vector magnetogram for this sunspot, derived from SVM observations, is shown in top panels of figure 5.1. The vector magnetogram has been transformed from image plane (left panel) to heliographic plane (right panel) using algorithm of Venkatakrishnan et al. (1988). The north is upwards and west is towards right hand side in the transformed vector magnetogram. The differences in the shape of the neutral line can be noticed as was found by Venkatakrishnan et al (1988) in studies of other active regions. The time averaged line-of-sight velocity field over the sunspot is also shown in figure 5.1 (lower panel). This mean LOS velocity field is constructed by averaging two hour time series of MDI dopplergrams. The well known Evershed flow can be noticed clearly in the penumbral regions. A weak outflow is seen even in the umbral region. At the lower side of the sunspot there are strong converging flows which coincide with the polarity inversion line between the main sunspot (of negative polarity) and a small island of opposite polarity close by. The existence of the converging flow region in the observations suggests that, near the polarity inversion line the Evershed flow of the main sunspot interacts with the opposing flow from the adjacent opposite polarity region. The mass involved in the converging flows, eventually, should disappear below the photosphere. The situation is similar to the downflow regions of the inter-granular lanes.

The figure 5.2 shows the general picture of the sunspot in intensity and LOS field in MDI observations (upper panel). The lower panel of figure 5.2 shows the map of the sunspot in low and high-frequency. The low-frequency power (LFP) maps of the sunspot are made by summing power over frequency range $0 < \omega < 5.2$ mHz. The enhanced power surrounding sunspot, called "acoustic halos", can be seen in high frequency map as found by Hindman & Brown (1998). Further, the low frequency maps shows the coincidence between regions of decreased power and magnetic field concentrations as was found earlier (Leighton, Noyes & Simon 1962; Lites et al. 1982).

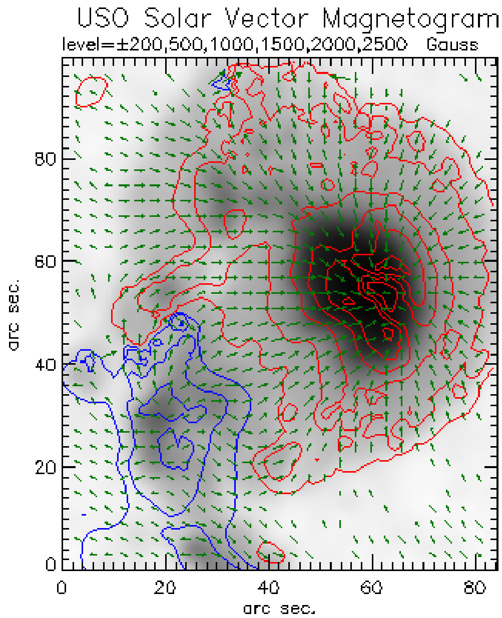

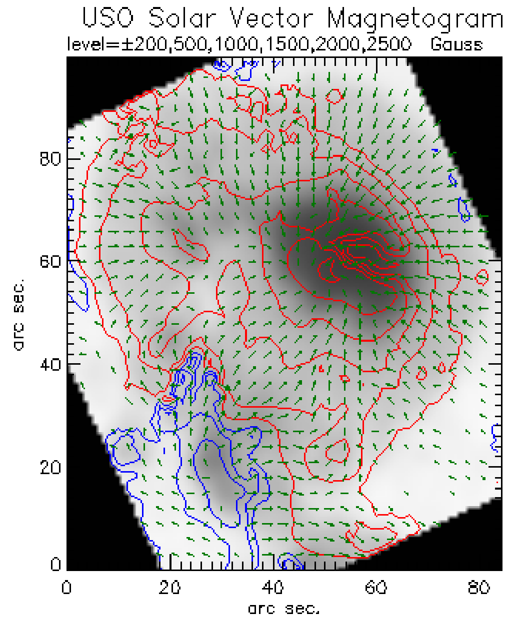

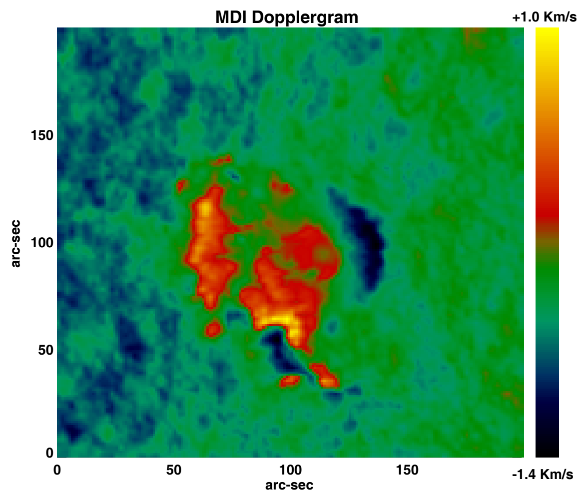

Figure 5.1: The top panel shows the USO vector magnetogram of NOAA AR No. 10756, as observed in image plane (left) and in transformed heliographic plane (right). The lower panel shows a two hour mean doppler image of the sunspot. The dopplergram shows strong upflows and downflows in the neutral line region.

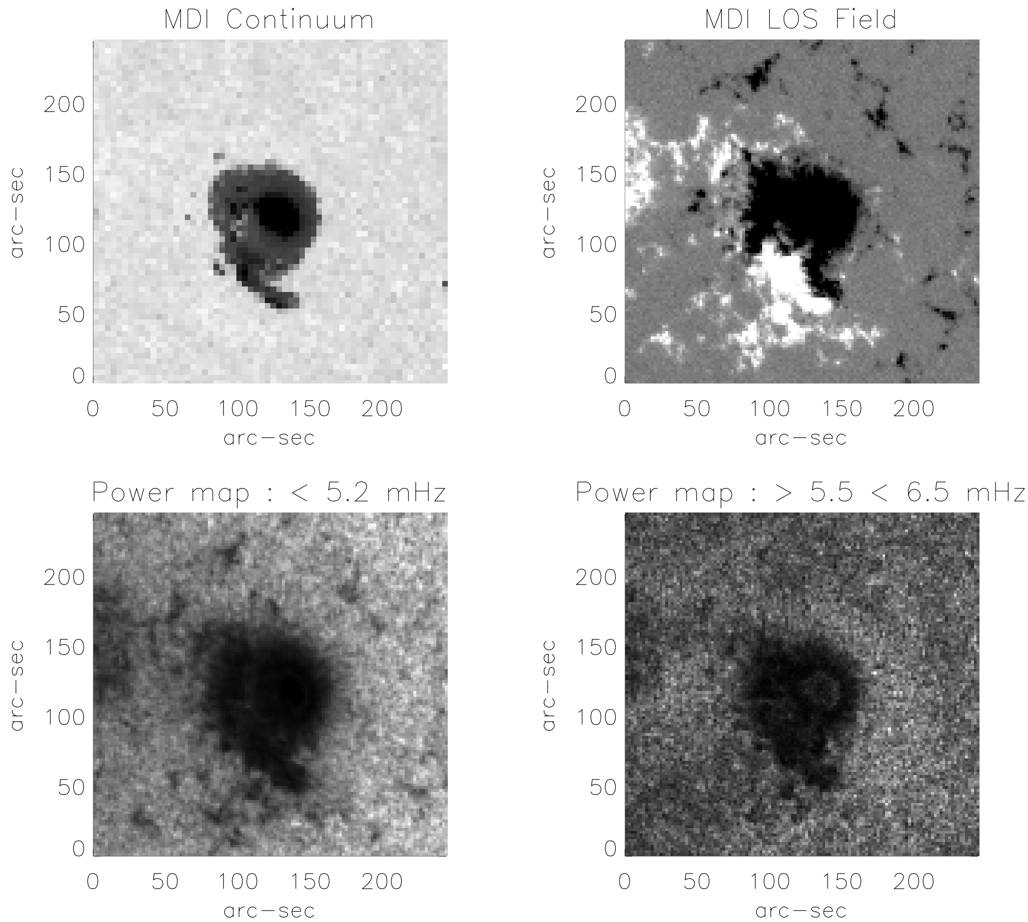

Figure 5.2: The top panel shows continuum intensity image (left) and LOS magnetogram (right) obtained from SoHO/MDI. The lower panel shows maps of low frequency and high frequency acoustic power. The low-frequency power (LFP) maps of the sunspot are made by summing power over frequency range $0 < \omega < 5.2$ mHz. Similarly, high-frequency power (HFP) maps are made by summing power over frequency range $5.5 < \omega < 6.5$ mHz.

5.3 Variation of acoustic power with vector field parameters

In order to study the dependence of acoustic spectra on magnetic field strength and inclination separately we have sorted out the regions into three inclination bins and two magnetic field strength bins. The field inclination bins are (i)$30° < \gamma < 50°$, (ii)$50° < \gamma < 70°$, and (iii) $70° < \gamma < 90°$. The magnetic field bins are (i) $B < 1000G$, and (ii) $B > 1500G$. The plots in figure 5.3 shows the mean power spectra in different bins (indicated above each plot). As may be noticed, for strong fields (left column), the power in 5 minute band is suppressed more in vertical field regions than the inclined field regions. However, the high frequency band of power spectra shows a weak opposite trend. Further the following observations can be made:

(i) For a given inclination the peak power is higher for weaker fields.

(ii) The shape of the power spectra is independent of inclination for weaker fields.

(iii) The power spectra changes are very sensitive to the inclination of strong fields.

(iv) Peak power and ratio of low to high frequency component increases with inclination for strong fields.

5.4 Inferences on excitation of 5 minute oscillations in magnetic regions

Globally, the power or amplitude of the solar oscillations is capped by the balance between the power delivered to the acoustic cavity, (chiefly by convective excitation) and the power lost from the cavity by radiation of various kinds of progressive MHD waves. It was found recently that the p-modes could leak enough power into the chromosphere through inclined surface fields, and possibly drive formation of spicules (Bart De Pontieu et al 2004). Recently, Schunker and Cally (2006)

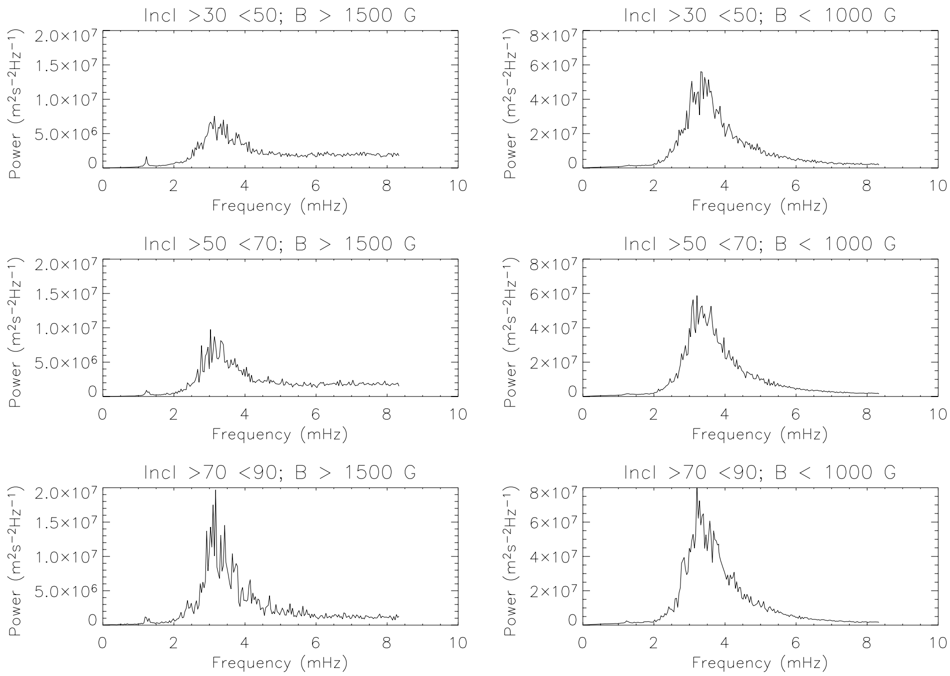

Figure 5.3: The plots show mean power spectrum in regions lying in inclination and field strength bins indicated on top of each plot.

performed wave mechanical and modified ray theory based numerical studies of fast-to-slow conversion in magnetically modified model-S (Christensen Dalsgaard 1996). They found that the mode conversion near the equipartition depth, where Alfven speed matches local sound speed, could enhance acoustic signals at heights observed by SOHO/MDI. They calculated acoustic wave energy density at a height (z=200km) roughly matching with SoHO/MDI as a function of magnetic field inclination to the vertical (see fig 5, 6, Schunker & Cally, 2006). Our observations that acoustic power increases with magnetic field inclination for strong fields show similar trend as predicted by Schunker & Cally (2006).

Alternatively, another simple minded explanation for our observations might be given as follows. The suppression of convection by magnetic fields in a highly conducting plasma is well known (Chandrasekhar, 1961; Parker, 1979). It is also known that convection in rolls is possible wherever the magnetic field has large inclination to the gravity vector. Thus, the increase in power of 5 minute oscillations with inclination could be due to convective motions, which presumably excite the oscillations, and are more vigorous in regions of large field inclination. In addition, the plasma beneath these regions is likely to be field free, thus enhancing the power at deeper layers where the 5 minute oscillations would be excited.

The behaviour of the higher frequency oscillations in strong and inclined field does not fit the above simple explanation. Since the absolute value of the power is large only for the strong less inclined fields, and since these are also regions of lower signal to noise ratio for the measurements, we would hesitate to discuss a physical interpretation for this behaviour. On the other hand, it certainly calls for deeper study of high frequency oscillations in magnetized regions, especially in view of the potential for high frequency waves to heat the solar chromosphere. In the near future HMI/SDO observations is expected to carry out detailed observational studies, which together with numerical modeling should make our understanding of acoustic wave interaction with magnetic fields much better.

5.5 Acoustic power distribution

The distribution of acoustic power in sunspot is shown in figure 5.4. The map on left shows the low frequency map and the map on right shows the map of high frequency power. It may be noticed that there are three regions marked as R1, R2 and R3 in which the power in region R2 is stronger than the regions R1 and R3 in both maps. This region of enhanced power corresponds to the umbra-penumbra boundary, while R1 and R3 correspond to umbral and mid-outer penumral region. Our results agree with the finding that the power is reduced in middle penumbra as compared to inner and external penumbra (Marco, E et al 1996).

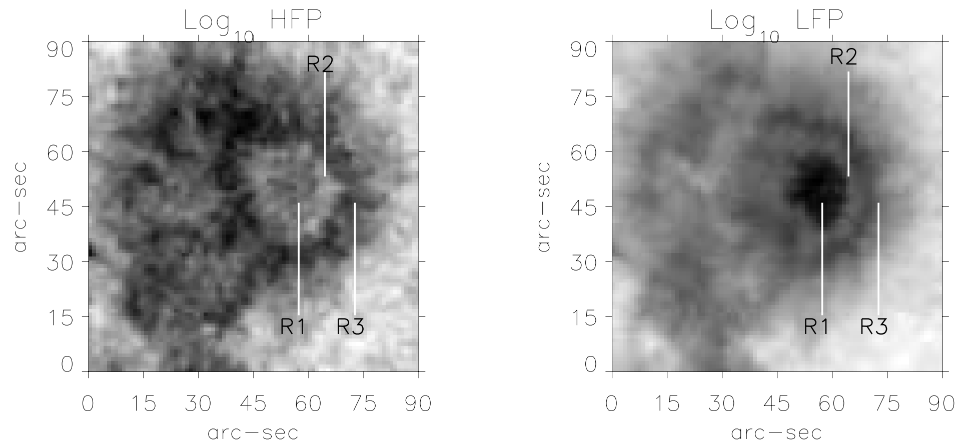

Figure 5.4: The left panel shows the high frequency power map and the right panel shows low frequency power map to a logarithmic scale. The low-frequency power (LFP) maps of the sunspot are made by summing power over frequency range $0 < \omega < 5.2$ mHz. Similarly, high-frequency power (HFP) maps are made by summing power over frequency range $5.5 < \omega < 6.5$ mHz. The regions marked by R1, R2 and R3 are discussed in the text.

5.6 Results and Discussion

In the recent years, helioseismic observations of the sun, meant to study the solar interior, have been used extensively to study the p-mode interaction with surface magnetic fields. It was known long back that in sunspots or regions of strong magnetic field the p-mode amplitudes are suppressed (Leighton, Noyes & Simon 1962; Lites et al. 1982). This reduction in p-mode amplitude is attributed to absorption of acoustic waves by magnetic structures (Cally 1995). On the other hand, the high frequency acoustic power around active regions as measured with the Fe I 5576 line and Ca II K line show enhanced amplitudes of high frequency oscillations (Braun et al, 1992; Brown et al 1992). Using observations from MDI (Michelson Doppler Imager, Scherrer et al. 1995), Hindman & Brown (1998) showed that the high-frequency oscillation power is a strong function of magnetic field in the 50-250 Gauss range.

These regions of enhanced high-frequency acoustic power are termed as "halos", due to their appearance as a bright halo surrounding active regions or sunspots in maps made by integrating acoustic power in high frequency band. Their study of MDI continuum intensity fluctuations however did not show any enhancement of high frequency power, suggesting that the oscillations may be incompressible in nature. Similarly, Jain & Haber (2002) found lack of "halos" in continuum intensity power maps, while their spectral line depth observations showed presence of power "halos". Few plausible explanations for the acoustic "halos" have been suggested (Hindman & Brown 1998) like, acoustic emission or scattering is modified in presence of magnetic field or the acoustic motions align themselves to field direction thereby enhancing line-of-sight velocity component.

On the contrary, in the UV continuum data (with TRACE instrument), Muglach et al. (2005) found reduced high-frequency power around active region at chromospheric height. They inferred that the enhancement of photospheric high frequency power and reduction in chromospheric high frequency power may be due to interaction of acoustic waves with the magnetic canopy. In order to understand p-mode interaction with magnetic field, which has important implications for understanding the role of acoustic wave energy in coronal heating, it is important to gather detailed observational properties of active region acoustics.

In this paper we have studied, using vector magnetic field observations, the absorption of acoustic power in strong fields of different field inclinations. Also, we compared the distribution of acoustic power in three basic regions of sunspot i.e., in umbra, penumbra and umbra-penumbra boundary. The combined analysis of vector field observations and time series of MDI dopplergrams is very useful to understand the physical nature of coupling between acoustic waves and magnetic field which could be important source of coronal-heating.

5.7 Summary

A large sunspot was observed at Udaipur Solar Observatory on 29 April 2005 in NOAA 10756. Using combined observations of vector magnetic field from SVM of USO, Udaipur and dopplergrams from MDI/SoHO, we study the distribution of acoustic power in and around this large sunspot as a function of field geometry. The high ($5.5 < \omega < 7.5$ mHz) and low frequency ($0 < \omega < 5.2$ mHz) domains of the acoustic power spectrum are analyzed in relation to magnetic field strength and field inclination. Following observations were made: (i) For a given inclination the peak power is higher for weaker fields, (ii) the shape of the power spectra is independent of inclination for weaker fields,(iii) the power spectra changes are very sensitive to the inclination of strong fields, and (iv) Peak power and ratio of low to high frequency component increases with inclination for strong fields.

Also, the distribution of acoustic power in high and low frequency bins is studied by LFP anf HFP maps. It is found that the acoustic power in both frequency bands shows a small enhancement at the umbra-penumbra boundary. Our results agree with the finding that the power is reduced in middle penumbra as compared to inner and external penumbra (Marco et al 1996).

Chapter 6

Summary, Conclusion and Future Improvements

6.1 Summary and Conclusions

In this thesis the main emphasis is on the development of a magnetograph capable of measuring both longitudinal as well as the transverse components of magnetic field on the Sun. The observations of the Zeeman effect induced polarization across the spectral line is used for deriving magnetic fields. The derivation of magnetic field parameters is done by non-linear least squares fitting of observed profiles with theoretical profiles generated under the assumptions of Milne-Eddington model atmosphere and LTE. This method of measuring fields is superior to the conventional magnetographs which suffer from problems of (i) Zeeman saturation, i.e., saturation of polarization signals in presence of very strong fields, and (ii) Magneto-optical effects which effect the measurement of field azimuth in strong field regions.

The design and strategies used for integration of various opto-mechanical, electrical and electronic sub-systems were developed by me. The development of the instrument control system is based on an innovative technique which nicely interfaces the hardware data acquisition layer with data analysis layer. This control software equipped with a graphical user interface (GUI) allows users to operate the instrument with very little training. A complete data reduction and analysis toolkit has been developed with a GUI for the user to easily deal with vast amounts of data. The Milne-Eddington inversion of observed Stokes profiles is carried out by using a well documented MELANIE code of HAO, Boulder USA. A user friendly interface has been developed to carry out the inversion of observations interactively using this MELANIE code. This interface is general in nature and can be used to deal with the spectro-polarimetric data of any other instrument or adapt to any other inversion code. Further, a tool to visualize the magnetograms in standard manner, overlaying with H-α images, potential field calculation, resolution of 180° ambiguity in transverse field direction using acute angle method and transformation of observed vectors to heliographic coordinates is developed to facilitate quick-look analysis of vector magnetograms.

With these developments, the total time taken to arrive at a vector magnetogram is greatly reduced. This will eventually benefit SVM in terms of keeping up-to-date archive of magnetograms with minimal or no backlogs resulting in better usage of the instrument. The completion of the SVM instrument saw a period of extremely low solar activity due to overlap with solar cycle minimum. This circumstance prevented us from carrying out solar flare related studies from the vector magnetograph. However, a few sunspots appeared which were utilized for carrying out correlation studies of p-mode power amplitude and magnetic field parameters. It was found that the acoustic power amplitude depends on field inclination in strong field regime. The results are found to be in line with recent theoretical works showing similar relationship between inclination and acoustic power amplitude (Bart De Pontieu et al 2004; Schunker & Cally 2006).

Further, a preliminary study of comparison between field azimuth in penumbral regions of simple sunspots and the direction of super-penumbral fibrils as seen in H-α filtergrams was carried out. This study shows similarities in the sign of "twistedness" of the sunspot fields in photosphere as well as chromosphere (Tiwari, S. et al 2007). The figure 6.2 illustrates these observational results. The top panel shows the overlay of photospheric transverse field vectors on the chromospheric H-α filtergram. The filtergrams have been obtained from USO, Udaipur and transverse field vectors are derived from SVM observations. The NOAA number and date of observed sunspots is mentioned on the top of each figure. The dextral chirality of super-penumbral "whorls" can be noticed clearly in these filtergrams. The lower panel shows superimposed observed photospheric transverse field (red arrows) and (current-free) potential transverse field (blue arrows) overlaid on the continuum image of the sunspot. The departure from potential field directions also shows dextral chirality of the observed transverse field. This shows that the sense of chirality of superpenumbral "whorls" is maintained even in the photosphere of sunspot penumbra. These results give us confidence in using chromospheric fibrils for resolving 180° ambiguity of transverse field direction.

Further, it may be noted that opposite hemispheres predominantly show opposite signs of various indicators of chirality like filaments (dextral or sinistral), superpenumbral "whorls" etc. This hemispheric dependence is seen in the sign of magnetic field helicity also (Zhang et al 2003; Pevtsov et al 2003), although the rule is statistically quite weak as compared to statistics of chirality indicators. The statistical work on magnetic helicity distribution across hemispheres is mainly carried out using magnetographs which are prone to magneto-optical effects. Thus, instruments like SVM, which derive field azimuths taking magneto-optical effects into account, shall provide better estimates of hemispheric helicity distribution by observing throughout the solar cycle 24 and beyond.

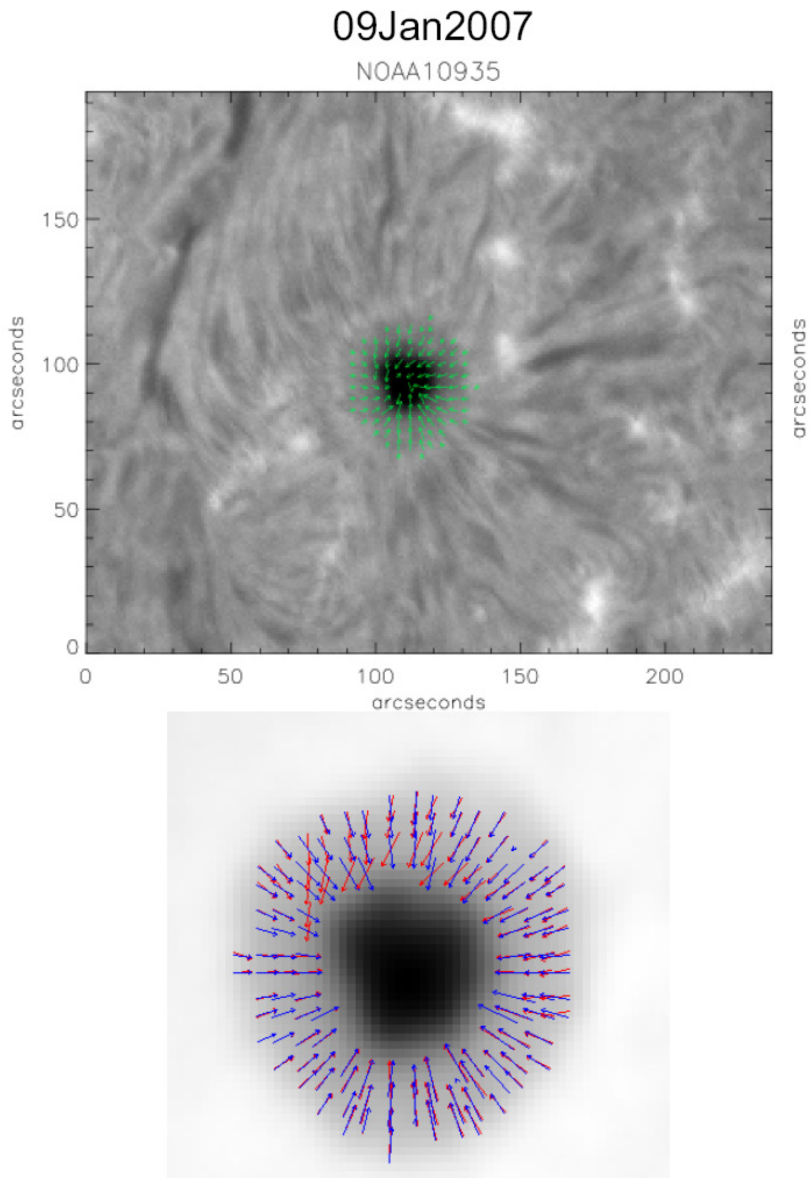

Figure 6.1: Chirality of NOAA 10935 on 9 January, 2007

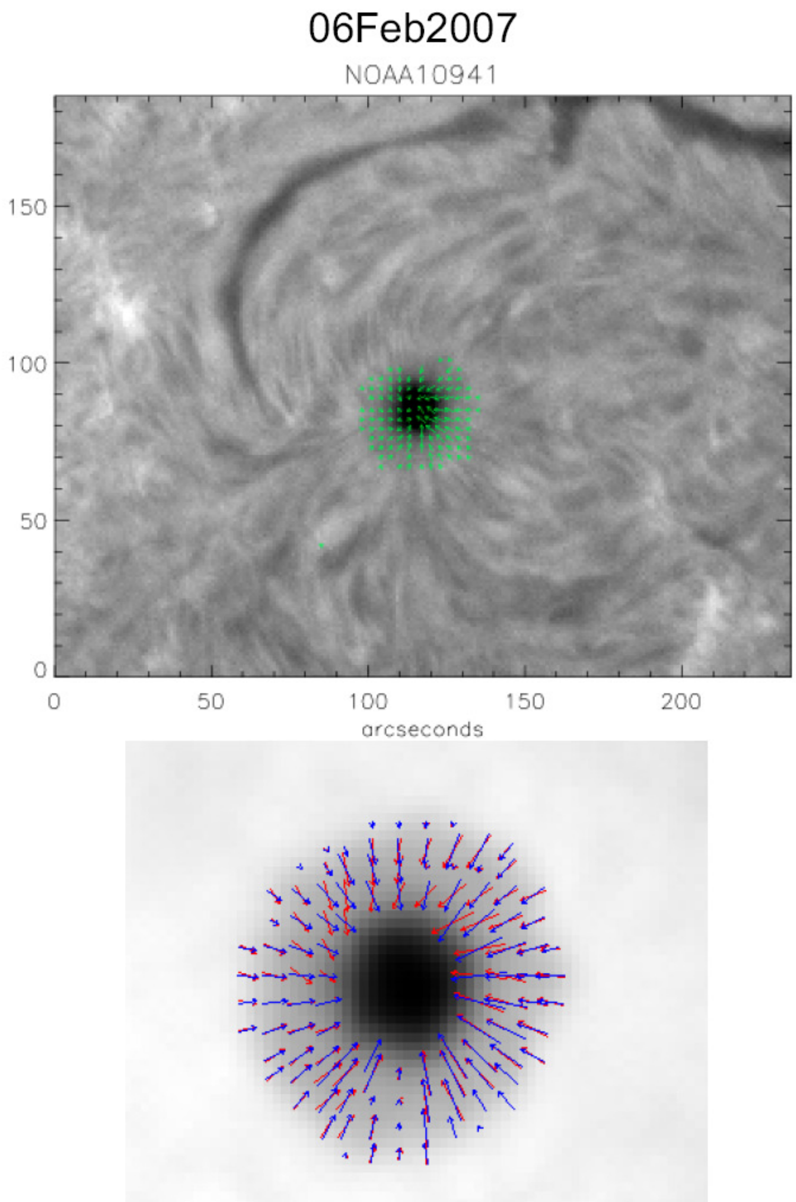

Figure 6.2: Chirality of NOAA 10941 on 6 February, 2007

6.2 Future Improvements

Every instrument makes some trade-offs in its design parameters. These may be imposed either due to the limitations of the technology itself or the accessibility of technology in the industry. However, with technological developments in most of the fields related to instrumentation namely, optics, computers, CCD cameras, electronics etc. there is always scope for improving the design and performance of an instrument. This argument is valid for Solar Vector Magnetograph also. The following paragraphs discuss the areas in which SVM can be improved in future versions.

6.2.1 A fast CCD camera and Modulator

Ideally one would like to have a fast modulator such that all modulations are accomplished before the seeing changes (typically tens of milliseconds). Such fast modulations can be achieved with Ferro-electric Liquid Crystal (FLC) modulators and Piezo-Elastic-Modulators (PEMs) however, the limited readout speed of area-scan detectors is the main bottle-neck. The typical readout time of commercially available fast area-scan cameras is of the order of 50 to 100 milliseconds for single readout. Thus, for one complete Stokes measurement, which requires at least four readouts, it takes about 300 to 400 milliseconds which is not adequate for beating the seeing. Specially designed and custom made cameras which match the required readout speeds prove to be very costly. Even if one is able to match the required readout speed, the photons collected by moderate sized telescope will not be enough for very short exposure times. In such case a very fast camera and modulators require telescope with large aperture to have sufficient photons in a few millisecond exposure time. Since one does not have unlimited resources, the best approach is to develop the instrument in phased manner. That is, upgrade the instrument to latest technology when the budget is available. For the present scheme of SVM the main improvements that can be made are as follows:

(i) A new CCD camera with faster speed and higher quantum efficiency: This is required due to the fact that present speed is only 2 frames per second, with an exposure time of 100 milliseconds. This speed is very slow considering the fact that the a wavelength scan for a single Stokes parameter needs at least 21 point scan and so the time taken for performing a wavelength scan can be reduced greatly by a faster camera. Also, it is desired that the new camera have electronic shutter, as the present mechanical shutter has a limitation that below 10 milliseconds exposures can not be taken. Also the faster cameras (i.e., 30 to 50 frames per seconds) with electronic shutter allow exposures of up-to microseconds. These very short exposure times require that the quantum efficiency of the detectors are high to exploit all the photons available.

(ii) A fast Modulation system based on LCVRs: The dual beam system of SVM polarimeter avoids the seeing induced spurious polarization signals. However, the fast modulation is required because the rotation of waveplates consumes lot of time in acquiring whole observing sequence (about 40 seconds in entire six data-cube sequence). Also, the problem of beam wobbling requires that the flats must be taken at all orientations and hence requires additional time. If a non-rotating modulator like nematic liquid crystals variable retarder (LCVRs) is used, then a single flat-field is enough. Also, at present a wavelength scan is performed for each Stokes parameter setting (i.e., for each orientation of polarimeter waveplates). The wavelength scan is repeated for another setting of polarimeter. This scheme can be optimized in the case of LCVRs such that at each wavelength position all Stokes parameters can be obtained in quick succession. In this mode the wavelength scan is required to be done only once per cycle of observation. In a LCVR based modulation system the advantage is that its retardance is variable and the operation can be adjusted for any wavelength range, unlike FLCs. With the proposed faster CCD camera and faster modulator system based on LCVRs we can tackle spurious seeing induced polarization and utilize all the available photons by retaining the dual beam analyzer system. The dual beam is advantageous since in a single beam system only 50% of the photons are utilized. Also, by performing “beam-exchange” and merging the two frames, one improves signal-to-noise ratio and minimizes noise due to camera readout and differential optical aberrations encountered by the dual beams.

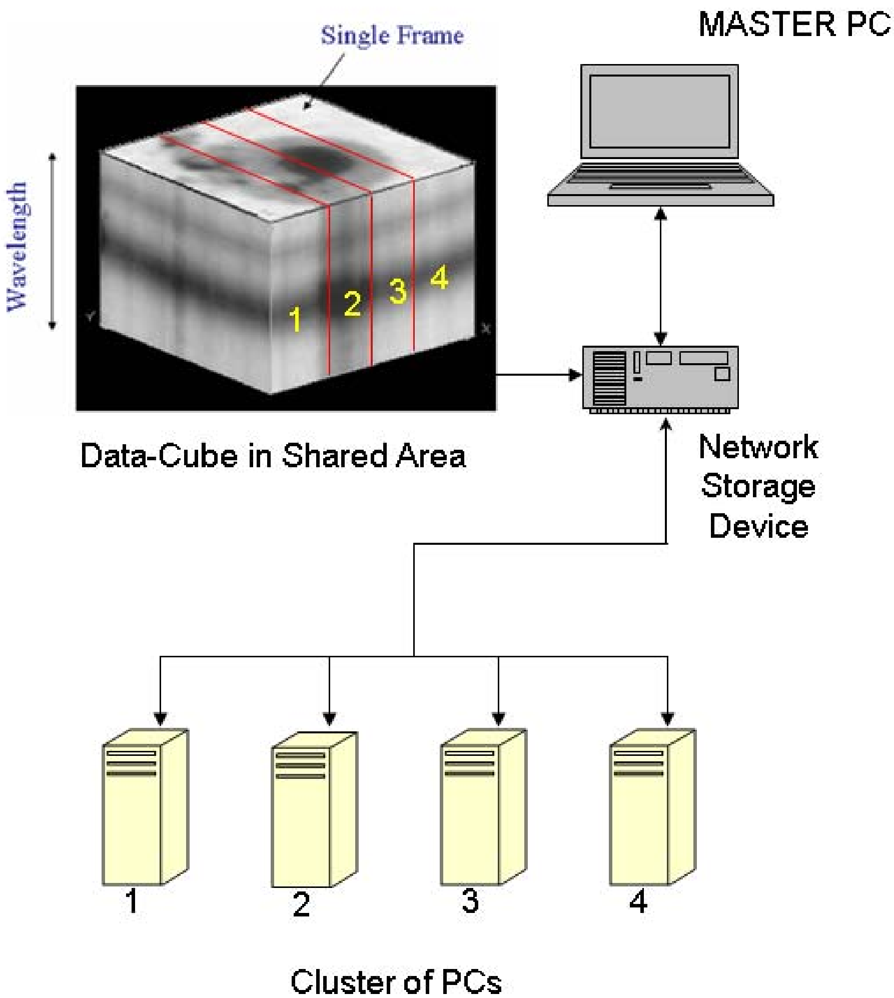

Figure 6.3: The schematic of performing parallel inversion of large number of profiles. The data-cube is split nto 1,2,3 and 4 files and each kept in common area on network. The files are inverted by respective PCs and results are gathered back by MASTER PC.

6.2.2 Parallelization of Stokes Inversion

The inversion of observed Stokes profiles to derive the magnetic field parameters requires lot of computer time. Specially when the number of profiles are too large.

This is typical of large observed field-of-view in imaging polarimeters. For instance in case of SVM, the typical map consists of 10,000 profiles corresponding to a circular field of 100 arc-sec diameter. Therefore, time taken for inverting the profiles over the entire map is very large in a single computer. Typically, for a Pentium IV processor with 3.2 GHz, and 512 MB RAM, the time taken for 10,000 profiles is about one and half hour. This has two disadvantages (i) the time taken is too large for real-time space weather forecasting, and (ii) the backlog of data to be inverted keeps on increasing with time. This is a great problem and several approaches are being tested these days for expediting the inversion process. One approach is to use Artificial Neural Networks (ANNs), where a large number of Stokes profiles are simulated and a database is created. Then the observed profiles are matched with the closest profile in least squares sense. The accuracy of this approach is however, being scrutinized. Another, approach is to use distributed computing. With the availability of cheap and fast PCs (computers with dual and quad core processors), network based disk storage, and fast network communication devices it is possible to use a network of PCs for parallel inversion on a single data set. A schematic of this method is shown in the figure 6.3. The data file is kept on a common disk storage on the server. The MASTER PC splits this file into smaller files, one for each PC in the network (i.e., each node), together with input parameters like the wavelength parameters, atomic parameters etc. After the file is split, a message is broadcast on the network, on listening to this message each nodes starts inverting the respective file. At the end of inversion by each node the results are kept on the same common place, which the MASTER PC combines in the end. The total time taken for inversion is thus inversely proportional to the number of PCs. For example with five PCs the typical time for inverting SVM maps will be only 18 minutes. As, the number of PCs in the research institute is typically large, i.e., greater than five, which we assumed above. If we request all the PC owners to allow the spare time of their PC for the parallel inversion, then the total inversion time will be reduced drastically. This needs to be implemented in SVM in near future.

6.2.3 Simultaneous Stokes observations in chromospheric lines

The magnetic field in chromosphere is more force-free in comparison to the photosphere where most of the field measurements are done routinely. The extrapolation of measured photospheric magnetic fields to coronal heights requires the fields at lower boundary (of the volume where field is extrapolated) to be force-free. This is also true for the computation of "free" energy in an active region, which is the difference between the energy derived from measured vector field (using Virial theorem) and the computed (current-free) potential field. These arguments emphasize that simultaneous observations in a chromospheric line is very important for solar activity studies and should be added to SVM in near future. The chromospheric lines that have been used in recent times are He 10830 (Solanki et al 2003; Lagg et al 2004; Wiegelmann et al 2005), Mg b lines(Lites et al 1988 ; Gosain et al 2003), H-β line (Zhang et al 1993), Na D1 line (Metcalf et al 2005) and H-α (Balasubramanian et al 2004).

The He 10830 lines are very suitable due to the fact that they include photospheric lines very closeby and these are optically thin chromospheric lines so scattering effects are minimal which simplifies their inversions (Solanki et al 2003; Lagg et al 2004). However, this line is in infra-red (IR) region and therefore needs a dedicated system optimized for IR and also the observing site must be suitable for these observations. In SVM, the Fabry-Perot filter has a operating wavelength range of 550-700 nm. Choosing a chromospheric line in this spectral region for spectro-polarimetry shall be very useful in future studies. Chromospheric vector field measurements have inherent difficulties regarding weak magnetic field strengths and complexity of NLTE line formation theory. The developments in instrumentation and NLTE based line inversion techniques together with advancements in Hanle diagnostics will lead to better understanding of chromospheric vector field properties in future.

6.2.4 Higher spatial resolution

It is important to obtain structure of vector magnetic fields at higher spatial resolutions in order to study small localized regions having sheared fields. The blurring and defocusing effects of the seeing are the main limiting factors in present version of SVM. One way of removing such effects, to some extent, is to have a simultaneous image in continuum near the spectral line used for polarimetry and use post processing techniques like de-stretching or polynomial warping to restore the structure of the images. So, a simultaneous continuum channel can be included in the optical scheme by using a beam splitter after the polarization analysis. This requires an additional CCD camera synchronized to the data camera. However, such techniques are of limited use and require lot of post-processing time. Instead, the deployment of a low-order adaptive optics together with tip-tilt image stabilization system developed at USO, Udaipur shall be a great leap for the SVM observations (Sridharan et al. 2005). For high resolution studies of sub-arcsecond scale solar magnetic structures a large telescope with high order adaptive optics is required. This shall be the focus of the upcoming facility at USO , Udaipur called MAST, i.e., Multi Application Solar Telescope (Venkatakrishnan 2005, 2006). The joint observations of SVM and MAST in different spatial and spectral scales will be of great value to solar physics. Also, the instrument shall contribute to the co-ordinated observations with space based observatories like HINODE (formerly called Solar-B), STEREO mission, and future missions like Solar Dynamics Observatory (SDO).

Appendix - A

Webcam based solar autoguider : An autoguider for correcting the drifts in telescope tracking during observations has been developed. Before describing the guider system a brief description of telescope control system is given below. The MKS-4000 (TM) telescope control system of the mount supplied by M/s Optical Guidance Systems consists of a microprocessor which has an on-board flash memory which contains the embedded program for controlling the telescope. The MKS 4000 system is interfaced to the telescope DC servo motors and optical encoders on RA and Dec axes. The interface to the user computer can be done either by a RS232 serial or USB port. The software supplied by the telescope manufacturer for controlling the telescope is called "TheSky(TM)" from M/s Software Bisque. The parameters of telescope control can be updated from this software, either temporarily for a particular session or stored in flash memory till further update. Further, a port for moving the telescope via a joystick is provided for manual control.

A guider port is given at the MKS 4000 board, which is essentially a RJ11 jack with six pins. Four pins are used for RA $\pm$ and DEC $\pm$ control. One is for power supply and one is grounded. The guide port follows the traditional standard of SBIG (M/s Santa Barbara Instrumentation Group, USA) autoguiders used in stellar astronomy. The guider signals for RA and DEC control are accepted as standard 5 volt TTL signals. The guider is developed using the commercially available webcam. We used e-CAM series webcam (model JIL 2240) from M/s Frontech, India. This particular model has an advantage that the imaging lens is collar mounted and can be easily removed and is small in size. The webcam has 480,000 imaging pixels and digitization in 24 bit color (8 bit per R,G,B). The camera can be programmed to read only in monochrome mode. The webcam is retro-fitted on a small finder-scope and is interfaced to the PC via standard USB cable. The full disk image of the sun is formed on the camera chip. The camera is readout at about 5 frames per second and the centroid of the image is calculated, which coincides with the center of the solar image. This centroid is then tracked and any drifts are corrected by applying TTL signals to the guider port via the parallel port of the PC. The TTL signals from PC parallel port are transmitted via an opto-isolator which prevents possible damage to the PC parallel port.

The software used for the webcam image capture is VidCap ActiveX (TM) from M/s Viscom Soft. The snapshot of the GUI of the guider software is shown in figure 1 below. The images are acquired and continuously overwritten on the hard-disk as bitmap (BMP) image. The image is continuously displayed in the live preview panel of the GUI. Also, embedded in the program is the IDL ActiveX component called "IDLDrawWidget". This is very useful for performing higher level programming and image processing of the guider images. The acquired bitmap images are continuously read from the disk via IDL ActiveX component in synchronization with acquisition rate. The centroid of the image is calculated and compared with the centroid of reference image and is used for guiding the telescope. The errors in the guiding are displayed as a plot in the lower panel of the interface. By choosing an arbitrary reference coordinate the telescope can be offset guided at any location on the sun. The field-of-view of the guider-scope is about 3×2 degrees which allows tracking the sun at extreme limb positions also. A better camera with more pixel resolution and dynamic range and addition of PID control to the software is planned for improving the guider accuracy in near future.

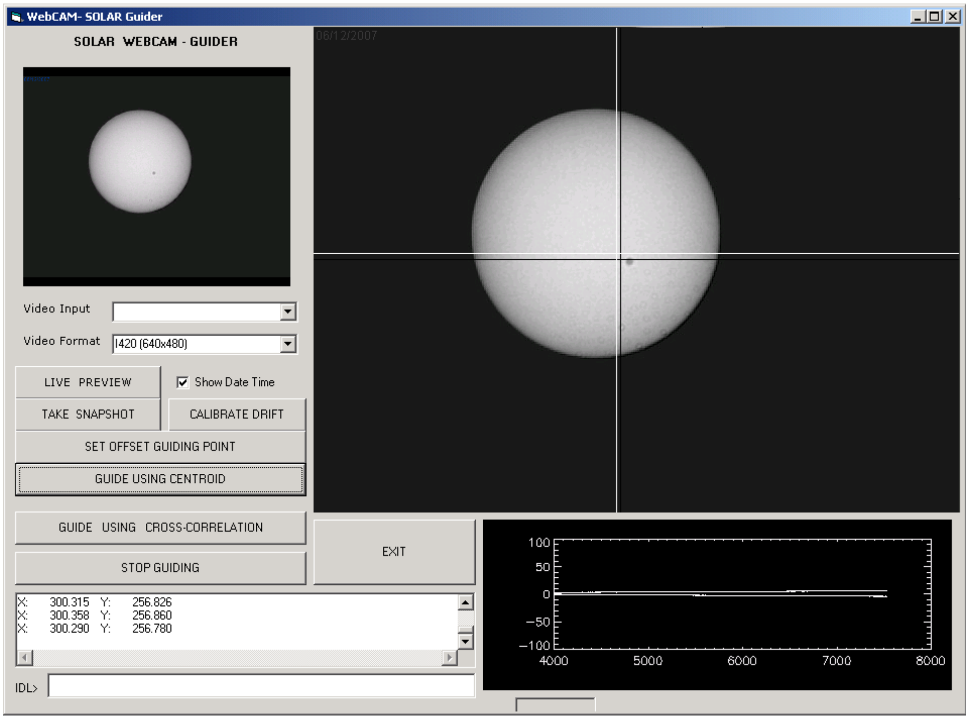

Figure 6.4: A snapshot of the guider control software. The live preview of the webcam output is seen on the upper left corner of the window. The format of the acquired image can be set between 800x600 and 160x120 pixels. The frequency of the loop cycle increases with decreasing image size. Snapshot pictures in monochrome format are acquired and displayed in upper right corner of the window. The buttons on the window allow to calibrate the drift, set guiding center for offset guiding and start-stop the guider loop.

Bibliography

[1] Aulanier, G., Demoulin, P., van Driel-Gesztelyi, L. et al.:1990, "3 D magnetic configurations supporting prominences - II The lateral feet as a perturbation of twisted flux tube", *Astron. Astrophys.* **335**, 309.

[2] Azzam, R. M. A. and Bashara, N. M.: 1987, "Ellipsometry and Polarized light",*North Holland*.

[3] Babcock, H.:1953, "The solar magnetograph", *Astrophys. J.* **118**, 387.

[4] Babcock, H.:1961, "The topology of the Sun's magnetic field and the 22-year cycle", *Astrophys. J.* **133**, 572.

[5] Balasubramaniam, K. S., Venkatakrishnan, P., and Bhattacharya, A.:1985, "Measurement of vector magnetic fields: I - Theoretical approach to the instrumental polarization of Kodaikanal Tower telescope", *Solar Phys.* **99**, 333.

[6] Balasubramaniam, K. S.:2002, "Imaging spectroscopy of a sunspot: Thermal and velocity structure", *Astrophys. J.* **575**, 553.

[7] Balasubramaniam, K. S., Christopoulou, E. B., and Uitenbroek, H.:2004, "Promises and pitfalls of solar H α Zeeman spectro-polarimetry", *Astrophys. J.* **606**, 1233.

[8] Bart De-Pontieu, Robert Erdelyi, and Stewart P. James.:2004, "Solar chromospheric spicules from the leakage to photospheric oscillations and flows", *Nature* **430**, 536.

[9] Beck, C., Schmidt, W., Kentischer, T., and Elmore, D.:2005, "Polarimetric Littrow Spectrograph - Instrument calibration and first measurements", *Astron. Astrophys.* **437**, 1159.

[10] Beckers, J. M.:1969, "A table of Zeeman triplets", *Sacpeak Obs. Cont. No. 141.*

[11] Beckers, J. M.:1971, "The measurement of solar magnetic fields", *IAU Symp. No. 43*, Dordrecht, Riedel, p 3.

[12] Bendlin, C., Volkmer, R., and Kneer, F.:1992, "A new instrument for high resolution two dimensional solar spectroscopy", *Astron. Astrophys.* **257**, 817.

[13] Bianda, M., Solanki, S. K., and Stenflo, J. O.:1998, "Hanle depolarization in the solar chromosphere", *Astron. Astrophys.* **331**, 760.

[14] Bianda, M.:2003, "Enigmatic magnetic field effects in the scattering polarization of the Ca I 4227 Åline", *ASP Conf. Ser.* **286**, 61.

[15] Biskamp, D.:1993, Book "Non-linear MHD", *Cambridge Univ. press*, Cambridge.

[16] Bommier, V., and Rayrole, J.:2002, "Search for polarimetric sensitivity in the first observations with the THEMIS spectro-polarimetric mode (August 1998 Campaign)", *Astron. Astrophys.* **381**, 227.

[17] Borrero, J. M., Tomczyk, S., Norton, A. et al:2007, "Magnetic field vector retrieval with Helioseismic and Magnetic Imager", *Solar Phys.* **240**, 177.

[18] Brajesh, K., Venkatakrishnan, P., and Venugopalan, K.:2007, "Site characterization using solar H-alpha images", *Solar Phys.*, in press.

[19] Braun, D. C., Duvall, T. L. Jr., and La-Bonte, B. J.:1987, "Acoustic absorption by sunspots", *Astrophys. J.* **319**, 27.

[20] Braun, D. C., Duvall, T. L. Jr., and La-Bonte, B. J.:1988, "The absorption of

high degree p-mode oscillations in and around sunspots", *Astrophys. J.* **335**, 1015.

[21] Braun, D. C., La-Bonte, B. J., and Duvall, T. L. Jr.:1990, "The spatial distribution of p-mode absorption in active region", *Astrophys. J.* **354**, 372.

[22] Braun, D. C., Lindsey, C., Fan, Y., et al.:1992, "Local acoustic diagnostics of the solar interior", *Astrophys. J* **392**, 739.

[23] Brickhouse, N. S., and La-Bonte, B. J.:1988, "Mass and energy flow near sunspots I: Observations and moat properties", *Solar Phys.* **115** 43.

[24] Brown, T. M., Bodgan, T. J., Lites, B. W. et al.:1992, "Localized sources of propagating acoustic waves in the solar photosphere", *Astrophys. J. Lett.* **394**, L65.

[25] Brueckner, G. E.:1963, "Photoelecktriche polarizationsmessungen an resonanzlimen in sonnenspecktrum", *Zietschrift fur Astrophysik, 1963.*

[26] Cally, P. S.:1995, "Effects of weak to moderate vertical magnetic fields on solar f and p modes", *Astrophys. J.* **451**, 372.

[27] Cavallini, F.:2006, "IBIS: A new post focus for solar imaging spectroscopy", *Solar Phys.* **236**, 415.

[28] Chandrasekhar, S.:1961, "Hydromagnetic and hydrodynamic instability", *Oxford Univ. press.*

[29] Chen, J.:1996, "Theory of prominence eruption and propagation: Interplanetary consequences", *J. Geophys. Res.* **101**, 27499.

[30] Chitre, S. M., and Davila, J. M.:1991, "The resonant absorption of p-modes by sunspots with twisted magnetic fields", *Astrophys. J.* bf 381, 31.

[31] Choudhary, D. P., Venkatakrishnan, P., and Gosain, S.:2002, "On the magnetic flux imbalance in solar active regions", *Astrophys. J.* **573**, 251.

[32] Christensen-Dalsgaard, J., Dappen, W., Demarque, P. et al.:1996, "", *Bull. Am. Astron. Soc.* **28**, 903.

[33] Collett, E.:1993, "Polarized Light: fundamentals and applications", *Marcel Decker.*

[34] Davila, J. M.:1987, "Heating of solar corona by the resonant absorption of Alfven waves", *Astrophys. J.* **317**, 514.

[35] Debi Prasad, C., Mathew, S. K., Bhatnagar, A., Ambastha, A.:1998, "Solar photospheric and chromospheric observations using Lithium Niobate Fabry-Perot etalon", *Ex. Astron.* **8**, 125.

[36] Do-Young, B., Young-Zoo, Y.:2002, "Development of Control Softwares for the SRAO 6-Meter Telescope Based on PCs Running Linux", *Experimental Astronomy.***14**, 183.

[37] Donati, J. F., Semel, M.:1990, " Zeeman -Doppler imaging: a new option for magnetic field study of Ap and solar type stars", *Solar Phys.* **128**, 227.

[38] Donati, J. F.,et al:1999, "Magnetic topology and prominence patterns on AB Doradus", *Mon. Not. Roy. Astron. Soc.* **1302**, 437.

[39] Duffet-Smith, P.:1979, "Practical astronomy with your calculator", *Cambridge Univ. Press.*

[40] Durney, B. R., De Yound David, S. and Roxburg, I. W.:1993, "On the generation of large scale and turbulent magnetic fields in solar type stars", *Solar Phys.* **145**, 207.

[41] Elmore, D. F., Lites, B. W.Tomczyk, S. et al.:1992, "The Advanced Stokes Polarimeter - A new instrument for solar magnetic field research", *Proc. of SPIE* **1746**, 22.

[42] Faurobert-Scholl, M.:1992, "Hanle effect with partial frequency redistribution II: Linear polarization of the solar Ca I 4227 Åline", *Astron Astrophys.* **258**, 521.

[43] Faurobert-Scholl, M.:1993, "Investigation of microturbulent magnetic fields in the solar photosphere by their Hanle effect in the Sr I 4607 Åline", *Astron Astrophys.* **268**, 765.

[44] Faurobert-Scholl, M.:1995, "Turbulent magnetic fields in the solar photosphere: diagnostics and interpretation", *Astron Astrophys.* **298**, 289.

[45] Forbes, T. G. and Acton, L. W.:1996, "Reconnection and field-line shrinkage in solar flares", *Astrophys. J.* **459**, 330.

[46] Gandorfer, A., and Povel, H.:1997, "First observations with a new imaging polarimeter", *Astron. Astrophys.* **328**, 381.

[47] Gosain, S., and Choudhary, D. P.:2003, " Simultaneous Stokes-V diagnostics of a sunspot using Mg b and Fe I lines", *Solar Phys.* **217**, 119.

[48] Gosain,S., Venkatakrishnan, P., and Venugopalan, K.:2005, "Design of instrument control software for Solar Vector Magnetograph at Udaipur Solar Observatory", *Experimental Astronomy* **18**, 31.

[49] Gosain,S., Venkatakrishnan, P., and Venugopalan, K.:2006, "Design and status of Solar Vector Magnetograph (SVM-I) at Udaipur Solar Observatory", *J. Astron. Astrophys.* **233**, 171.

[50] Graham, J. P. et al:2002, "Inference of solar magnetic field parameters from data with limited wavelength sampling", *Solar Phys.* **208**, 211.

[51] Hagyard, M. J.:1984, "Measurements of Solar Vector Magnetic Fields", *NASA Conf. Publ.* **2374**, Eds. M. J. hagyard.

[52] Hagyard, M. J.:1987, "Changes in measured vector magnetic fields when transformed into heliographic coordinates", em Solar. Phys. **107**, 239.

[53] Hale, G. E.:1908, "The Zeeman effect in the sun", em Pub. Astron. Soc. of Pacific. **20**, 287.

[54] Hale, G. E. and Nicholson, S. B.:1925, "The law of sunspot polarity", *Astrophys. J.* **62**, 270.

[55] Harvey, K. L., and Harvey, J. W.:1973, "Observations of moving magnetic features near sunspots", *Solar Phys.* **28**, 61.

[56] Harvey, K. L. (Ed.):1992 "The Solar Cycle" *PASP Conf. Ser.* **Vol. 27**

[57] Hernandez, G., and Mills, O. A.:1973, "Feedback stabilized Fabry-Perot interferometer", *Appl. Optics*, **12**, 126.

[58] Hicks, T. R., Reay, N. K., and Stephens, C. L.:1976, "A servo-controlled Fabry-Perot interferometer with online computer control.", *Astron. Astrophys.* **51**, 367.

[59] Hindman, B. W., and Brown, T. M.:1998, "Acoustic power maps of solar active region", *Astrophys. J* **504**, 1029.

[60] Hollweg, J. V., and Sterling, A. C.:1984, "Alfvenic resonant cavities in the solar atmosphere", *Astrophys. J.* **282**, 31.

[61] Hough, J. H., Lucas, P. W., Bailey, J. A. et al:2006, "Planetpol: A very high sensitivity polarimeter", em Pub. of Astron. Soc. Pacific **118**, 1305.

[62] Hundhausen, A. J.: 1988, in *Proceedings of Solar Wind 6* **NCAR TN-306**, 181.

[63] Ionson, J. A.:1982, "Resonant electrodynamic heating of stellar coronal loop: A LRC circuit analog", *Astrophys. J.* **271**, 778.

[64] Ivanov, V. V.:1991, "Stellar Atmospheres: Beyond Classical Models (eds. L. Crivellari, I. Hubney and D. G. Hummer)", *Proc. NATO* **81**, Kluwer.

[65] Jain, R., and Haber, D.:2002, "Solar p-modes and surface magnetic fields: Is there an acoustic emission ? MDI/ SOHO observations", *Astron. Astrophys.* **387**, 1092.

[66] Jones, H. P., Duvall, T. L., Harvey, J. W. et al:1992, "The NASA/NSO spectro-magnetograph", *Solar Phys.* **139**, 211.

[67] Keller, C. U.:2000, "Anomalous polarization effects due to coherent scattering on the sun", *Astron. Astrophys.* **355**, 789.

[68] Kentischer, T. J., Schmidt, W., Sigwarth, M., and Uexkuell, M. V.:1998, "TESOS: A double Fabry-Perot instrument for solar spectroscopy", *Astron. Astrophys.* **340**, 569.

[69] Kiepenheuer, K. O.:1953, "Photoelectric measurements of solar magnetic fields", *Astrophys. J.* **117**, 447.

[70] Lagg, A., Woch, J., and Krupp, N.:2004, "Retrieval of the full magnetic field vector with the He I multiplet at 10830 Å, Maps of emerging flux region", *Astron. Astrophys.* **414**, 1109.

[71] Leighton, R. B., Noyes, R. W., and Simon, G. W.:1962, "Velocity fields in the solar atmosphere: I - Preliminary report", *Astrophys. J.* **135**, 474.

[72] Lites, B. W., White, O. R., and Packman, D.:1982, "Photoelectric observations of propagating sunspot oscillations", *Astrophys. J.* **253**, 386.

[73] Lites, B. W., and Skumanich, A.:1984, " The inference of vector magnetic fields from polarization measurements with limited spectral resolution", *NASA Conf. Publ.* **2374**, Eds. M. J. Hagyard.

[74] Lites, B. W.:1987, "Rotating waveplates as polarization modulator for stokes polarimetry of the sun: Evaluation of seeing induced cross-talks", *Appl. Optics* **26**, 3838.

[75] Lites, B. W., Skumanich, A, Rees, D. E. et al :1988, "Stokes profile analysis and vector magnetic fields IV : Synthesis and inversion of the chromospheric Mg I B lines", *Astrophys. J.* **330**, 493.

[76] Lites, B. W., Pillet, V. Martinez, and Skumanich, A.:1994, "A quantitative comparison of vector magnetic field measurement and analysis techniques", *Solar Phys.* **159**, 203.

[77] Lites, B. W.:1996, "Performance characteristics of Advanced Stokes Polarimeter", *Solar Phys.* **163**, 223.

[78] Livingston, W. C., Harvey, J. W., Slaughter, C., Trumbo, D.:1976a, "Solar magnetograph employing integrated diode arrays", *Applied Optics* **15**, 40.

[79] Livingston, W. C., Harvey, J. W., Pierce, A. K., Scharge, D., Gillespe, B.:1976b, "The Kitt Peak 60 cm vacuum telescope", *Applied Optics* **15**, 33.

[80] Lockwood, M., Stamper, R., and Wild, M. N. :1999, "A doubling of the sun's coronal magnetic field during the past 100 years", *Nature* **399**, 437.

[81] Low, B. C.:1996, "Solar activity and the corona", *Solar Phys.* **167**, 217.

[82] Luhe, von der., and Kentischer, T. J.:2000, "High resolution performance of a triple Fabry-Perot filtergraph", *Astron. Astrophys. Suppl.* **146**, 499.

[83] Luhe von der, O. et al.:2002, "Adaptive optics system for a 1.5 m solar telescope", *Proc. SPIE* **4538**, 197.

[84] Malherbe, J. M., tarbell, T., Wiik, J. E. et al.:1997, "The post flare loops and the nearby active chromosphere of 1992 June 26", *Astrophys. J.* **482**, 535.

[85] Marco, E., Aballe Miller, M. A., and Vazquez, M. et al.:1996, "Spatial changes of oscillatory pattern in sunspot penumbrae at the photosphere", *Astron. Astrophys.* **309**, 284.

[86] Martin, S. F. and Feynman, J.:1995, "The initiation of coronal mass ejections by newly emerging magnetic flux", *J. Geophys. Res.* **100**, 3355.

[87] Martinez Pillet, V., Collados, M., Sanchez Almeida, J. et al.:1999, "LPSP, TIP - Full stokes polarimeters for the Canary islands observatories", *ASP Conf. Ser. No. 183*, Eds. T. R. Rimelli, K. S. Balasubramaniam, R. R. Radick, p264.

[88] Mathew, S. K., Bhatnagar, A., C. Debi Prasad, and Ambastha, A.:1998a, “Fabry-Perot based solar videomagnetograph”, *Astron. Astrophys. Supp.* **133**, 285.

[89] Mathew, S. K.:1998b, “A study of solar magnetic and velocity fields”, *Ph. D. thesis, M. S. University, Baroda*

[90] Metcalf, T. R., Leka, K. D., and Mickey, D. L.:2005, “Magnetic free energy in NOAA, Active Region 10486 on 2003, Oct. 29”, *Astrophys. J. Lett.* **623**, L53.

[91] Mickey, D. L., Canfield, R. C., La Bonte, B. J. et al:1996, “ The Imaging Vector Magnetograph at Haleakala”, *Solar Phys.* **168**, 229.

[92] Mughlach, K., Hofmann, A., and Staude, J.:2005, “Dynamics of solar active regions: II Oscillations observed with MDI and their relation to magnetic field topology”, *Astron. Astrophys.* **437**, 1055.

[93] Orozco Suarez, D., Bellot Rubio, L. R., Vargas Dominguez, S. et al:2006, “Simulation and analysis of VIM measurements: feedback on design parameters”, *Proceed. of ”The Second Solar Orbiter Workshop”, 2006, Athens*, **astro-ph/0611443**

[94] Parker, E. N.:1979, “Cosmical magnetic Fields”, *Clarendon Press, Oxford.*

[95] Parker, E. N.:1984, “Vector structure of active magnetic fields”, in *NASA. Conf. Pub. 2374, Ed. M. J. Hagyard.*

[96] Pevtsov, A. A., Canfield, R. C., and Zirin, H.:1996, “Reconnection and helicity in a solar flare”, *Astrophys. J.* **473**, 533.

[97] Pevtsov, A. A.:2003, “Helicity patterns on the sun”, *Adv. Space. Res.* **32**, 1867.

[98] Povel, H. P.:1998, “The Zurich imaging Polarimeter (ZIMPOL)”, *Meeting of the AG at Heidelberg, Sept 14-19*, Talk No. 107.

[99] Press, W. H. et al:1992, “Numerical Recipes in FORTRAN: The art of scientific computing”, *Cambridge Univ. Press.*

[100] Raadu, M. A., Schmieder, B., Mein, N., and Gesztelyi, L.:1988, "Photospheric induced destabilization and ejection of prominence material", *Astron. Astrophys.* **197**, 289.

[101] Rachkovsky, D. N.:1972, "On the theory of radiative transfer in a magnetic field", *Izv. Kryskoj Astrofiz.* **43**, 190.

[102] Rimelle, T. R. et al.:2006, "Progress with solar multi-conjugate adaptive optics at NSO", *Proc. SPIE* **6272**, 5.

[103] Rompolt, B.:1990, "Small scale structure and dynamics of prominences", *Hvar Obs. Bull.* **141**, 37.

[104] Rust, D. M., Burton, C., Abell, R.:1985, "A Fabry-Perot etalon for differential spectral imaging", *Bull. Am. Astron. Soc.* **17**, 642.

[105] Rust, D. M., and Kumar, A.: 1996, " Evidence for helically kinked magnetic flux ropes in solar eruptions", *Astrophys. J.* **464**, L199.

[106] Sankarasubramanian, K., and Venkatakrishnan, P.:1998, "A CCD based polarization interferometric technique for testing waveplates", *Optics and Laser Tech.* **30**, 15.

[107] Sankarasubramanian, K., and Venkatakrishnan, P.:2000, "Stokes polarimetry at Kodaikanal Tower Tunnel Telescope", *J. Astron. Astrophys.* **21**, 241.

[108] Sankarasubramanian, K., Elmore, D. F., Lites, B. W. et al:2003, "Diffraction Limited Spectro-Polarimeter: Phase I", *Proceed. of SPIE* **4843**, 414.

[109] Sankarasubramanian, K., Rimelli, T. R., Lites, B. W.:2006, " Diffraction Limited Spectro-polarimetry at the Dunn Solar Telescope", *Bull. Am. Astron. Soc.* **36**, 686.

[110] Scharmer, G. B. et al.:2000, "Workstation based solar stellar adaptive optics system", *Proc. SPIE* **4007**, 239.

[111] Scherrer, P. H. et al.:1996, “New views of the sun’s interior from the SOHO/MDI space experiment”, *Bull. Am. Astron. Soc.* **28**, 1298.

[112] Schmidt, W., Beck, C., Kentischer, T. et al.:2003 “POLIS: A spectro-polarimeter for the VTT and for GREGOR”, *Astron. Nachr.* **324**, 300.

[113] Schmieder, B.:1992, “Post Flare Loops”, in *Lecture Notes in physics*,**399**, 124.

[114] Schunker, H, Cally, P. S.:2006, “Magnetic field inclination and atmospheric oscillation above solar active regions”, *Mon. Not. Roy. Astron. Soc.* **372**, 551.

[115] Semel, M.:1987, “Polarimetry and imagery through uniaxial crystals: Application to solar observations with high resolution”, *Astron. Astrophys.* **178**, 257.

[116] Semel, M.:1993, “Zeeman-Doppler imaging of active stars: III- Instrumental and technical considerations”, *Astron. Astrophys* **278**, 231.

[117] Sheeley, N. R. Jr.: 1969, “The evolution of photospheric network”, *Solar Phys.* **9**, 347.

[118] Shurcliff, W. A.:1962 “Polarized Light: production and use”, *Harvard Univ. press.*

[119] Skumanich, A., Lites, B. W., Martinez Pillet, V., and Seagraves, P.:1996, “The Calibration of Advanced Stokes Polarimeter”, *Astrophys. J. Suppl.* **110**, 357.

[120] Socas Navarro, H.:2001, “Stokes inversion techniques: Recent achievements and future horizons”, *236*, 487.

[121] Socker, D. G. et al.:1996, “LASCO, spectrometric Lyot coronograph tunable passband filter”, *Proc. SPIE* **2804**, 126.

[122] Solanki, S. K., Lagg, A., Woch, J. et al.:2003, “Three dimensional magnetic field topology in a region of coronal heating”, *Nature.* **425**, 692.

[123] Solanki, S. K., Usoskin, I. G., Kromer, B. et al.:2004, “An unusual solar activity in the last century”, *Nature.* **431**, 1084.

[124] Sridharan, R., Bayanna, A. R., Kumar, B., and Venkatakrishnan, P.:2005, "An image stabilization system for solar observatory", *Bull. Astron. Soc. india.* **33** , 414.

[125] Sridharan, R.:2001, "Techniques for achieving higher spatial resolution", *Ph. D. Thesis*, Bangalore University.

[126] Stenflo, J. O.:1974, "Observations of resonance polarization in Ca I 4227 Å", *Solar Phys.* **37**, 31.

[127] Stenflo, J. O.:1980, "Resonance line polarization: V - Quantum mechanical interference between states of different angular momentum", *Astron Astrophys.* **84**, 68.

[128] Stenflo, J. O. :1983, " Coherent scattering in solar spectrum - survey of linear polarization in the range 4200 - 9950 Å", *Astron. Astrophys. Suppl.* **54**, 505.

[129] Stenflo, J. O.:1992, " On the validity of Babcock-Leighton approach to modeling the solar cycle", in *Proceedings of NSO/SP, 12th Summer Workshop, ASPC* **Vol. 27**, 83.

[130] Stenflo, J.O.:1994, "Solar magnetic fields: Polarized radiation diagnostics", *Kluwer.*

[131] Stenflo, J. O., Keller, C. U., and Gandorfer, A.: 1998, "Differential Hanle effect and spatial variation of turbulent magnetic fields on the sun" , *Astron. Astrophys.* **329**, 319.

[132] Stenflo, J. O.:2002, "Polarized radiation diagnostics of solar magnetic fields", *in Astrophysical Polarimetry*, Cambridge Univ. Press.

[133] Stenflo, J. O.:2006, "Spectropolarimetry with ZIMPOL, Plans for the future", *Memorie della Societa Astronomica Italiana* **78**, 181.

[134] Stepanov, V. E.:1960, "The absorption coefficient in the inverse Zeeman effect for arbitrary multiplet splitting and the transfer equation for light with mutually orthogonal polarization", *Astronomichski Zhurnal* **37**, 631.

[135] Tinbergen, J.: 1996 "Astronomical Polarimetry", *Cambridge Univ. press.*

[136] Tiwari, S., Joshi, J., Gosain, S., and Venkatakrishnan, P.:2007, "Evolution of magnetic helicity of NOAA over three consecutive rotations", *Proceed. of IHY workshop, Nainital, 5-10 May 2007.*

[137] Tritschler, A., Schmidt, W., Langhans, K. et al.:2002, "High resolution solar spectroscopy with TESOS: Upgrade from double to triple system", *Solar Phys.* **211**, 17.

[138] Tritschler, A., Bellot Rubio, L. R., and Kentischer, T. J.:2004 "Towards 2D-Spectro-polarimetry with TESOS and Adaptive Optics", *Bull. Am. Astron. Soc.* **36**, 794.

[139] Unno, W.:1956, "Line formation of a normal Zeeman triplet", *PASJ*, **8**, 108.

[140] van Driel-Gesztelyi, L., Wiik, J. E. et al:1997, "Post flare loops of 26 June 1992: IV - Formation and expansion of hot and cool loops", *Solar Phys.* **174**, 151.

[141] Venkatakrishnan, P., Hagyard, M. J., and Hathaway, D. H.:1988, "Elimination of projection effects from vector magnetograms - The pre-flare configuration of active region AR 4474", *Solar Phys.* **115**, 125.

[142] Venkatakrishnan, P., Brajesh Kumar, C., and Tripathy, S. C.:2002, "Variations of acoustic power with magnetic field as seen in GONG+ data", *Solar phys.* **211**, 77.

[143] Venkatakrishnan, P.:2003, " Solar magnetic fields", *Lec. Notes. Phys.* **619**, 202.

[144] Venkatakrishnan, P.:,2005 "Experiments and Design Activities for the Multi Application Solar Telescope", *Bull. Astron. Soc. india.* **33** , 353.

[145] Venkatakrishnan, P.:,2006 "Multi Application Solar Telescope (MAST): A Versatile Tool for Studying the Physics of Solar Eruptions", *Proceed. of US/NASA IHY Workshop in Bangalore, 2006*, Abstract Book p.33.

[146] Vrsnak, B., Ruzdjak, V., and Rompolt, B.:1991 "Stability of prominences exposing helical like patterns", *Solar. Phys.* **136**, 151.

[147] Wang, H. and Zirin, H.:(1992), "Flows around sunspots and pores", *Solar Phys.* **140**, 41.

[148] Wang, J., Zirin, H. and Shi, Z:1985, "The smallest observable elements of magnetic flux", *Solar Phys.* **98**, 241.

[149] Wang, Z., Brystanson-cross, P. J., and Whitehouse, D. J.:1996, " Phase shift determination by fringe pattern matching", *Optics and Laser Tech.* **28**, 417.

[150] Weigelmann, T., Lagg, A., Solanki, S. K. et al:2005, "Magnetic Loops: A comparison of extrapolation from photospheric and chromospheric measurements", *ESASP Pub.* **596**, 7.

[151] Wiehr, E.: 1975, "Measurement of solar disc polarization in a number of Fraunhofer lines and their adjacent continuum", *Astron. Astrophys.* **38**, 303.

[152] Wiehr, E.:1978, "Measurement of solar disc polarization in a number of Fraunhofer lines and their adjacent continuum: II Improved data and new line measurements", *Astron. Astrophys* **67**, 257.

[153] Yurchyshyn, V. B. and Wang, H.:2001, "Photospheric plasma flows around a solar moat", *Solar Phys.* **203**, 233.

[154] Zhang, H.:1993, "Solar chromospheric magnetic fields in active regions inferred by monochromatic images of Stokes parameter V of the H β line", *Solar Phys.* **146**, 75.

[155] Zhang, M., and Low, B. C.:2003, "Magnetic Flux emergence into the solar corona III The role of magnetic helicity conservation", *Astrophys. J.* **584**, 479.

[156] Zhang, M. and Low, B. C.:2005, "The hydromagnetic nature of solar coronal mass ejections", *Ann. Rev. Astron. Astrophys.*, **43**, 103.

[157] Zirin, H. and Martin, S. F.:1987,"The appearance and disappearance of magnetic flux on the quite sun", *Final Report, Oct 1981., Calif. Inst. of tech., Pasadena, Solar Astron. Group*

[158] Zirin, H.:1995, "On the comparison of filter magnetograph and the Advanced Stokes Polarimeter", *Solar Phys.* **155**, 1L.

List of Publications

I. Papers in Journals:

1. *Comparative study of LiNbO3 and servo-controlled air-gap Fabry-Perot etalons for solar applications*, Debi Prasad Choudhary and Sanjay Gosain *Experimental Astronomy.* **13**, 153 (2002).

2. *Design of Instrument Control Software for Solar Vector Magnetograph at Udaipur Solar Observatory*, S. Gosain, P. Venkatakrishnan, and K. Venugopalan. *Experimental Astronomy* **18**, 31 (2004).

3. *Design and Status of Solar Vector Magnetograph (SVM-I) at Udaipur Solar Observatory*, S. Gosain, P. Venkatakrishnan, and K. Venugopalan. *Journal of Astrophysics & Astronomy* **27**, 285 (2006).

II. In Proceedings:

1. *Acoustic power and magnetic field orientation in a large sunspot*, S. Gosain, P. Venkatakrishnan, and Venugopalan, K. *ESA SP-624: Proceedings of SOHO 18/GONG 2006/HELAS I, Beyond the spherical Sun, 18.* (2006).